



University
of Glasgow

Craig, Beverley R. (2006) *Magnetic and physical characterisation of soft thin films for use in perpendicular recording heads.*

PhD thesis

<http://theses.gla.ac.uk/4011/>

Copyright and moral rights for this thesis are retained by the author

A copy can be downloaded for personal non-commercial research or study, without prior permission or charge

This thesis cannot be reproduced or quoted extensively from without first obtaining permission in writing from the Author

The content must not be changed in any way or sold commercially in any format or medium without the formal permission of the Author

When referring to this work, full bibliographic details including the author, title, awarding institution and date of the thesis must be given

Magnetic and Physical Characterisation of Soft Thin Films for Use in Perpendicular Recording Heads

Beverley R. Craig M.Sci



UNIVERSITY
of
GLASGOW

Presented as a thesis for the degree of Ph.D. at the
Department of Physics and Astronomy, University of Glasgow
December 2006

©Beverley R. Craig 2006

Abstract

The increasing demand for greater storage densities poses constant challenges for the magnetic recording industry. The move to perpendicular recording occurred recently as this provides one way of increasing the storage density. For further advance in the technology it is important to gain an understanding of the micromagnetic and microstructural properties of the materials used in the hard drive. The material used in the write head is extremely important as the storage density is increased. CoFe alloys are currently of interest as they have a high magnetic moment and therefore have the potential to write to the high anisotropy materials required for writing at the high densities. Transmission electron microscopy is an ideal tool to gain such information as it provides a way of extracting magnetic information of the nanometre scale and structural information on the atomic scale.

Chapter 1 of this thesis provides an introduction to ferromagnetic materials and the magnetic energy contributions which are present. The principles of magnetic recording are then discussed along with the advantages of switching to perpendicular recording. The requirements for the write head material are discussed at the end of chapter 1 and a review of previous work on CoFe materials is given.

The main experimental techniques used for the work in this thesis are described in chapter 2. Firstly the sputter deposition of samples is discussed along with the characterisation of the bulk films with a B-H loop. A detailed description of transmission electron microscopy (TEM) and the various imaging modes which have been used is given. The Fresnel mode and the differential phase contrast (DPC) mode of Lorentz microscopy have been used to study the magnetisation reversal behaviour of the films and these are described. Electron energy loss spectroscopy (EELS), which was used to investigate the elemental distribution in the films, is also discussed. A dual beam SEM/FIB was used

to investigate the surface topology of the films and a brief description of the instrument is given. The final part of chapter 2 deals with the preparation of cross-sectional specimens with the encapsulation method and the patterning of thin films with electron beam lithography for use in the TEM.

By way of an introduction to the various reversal behaviour which is observed within magnetic films two soft films, NiFeCuMo and CoFeB, have been investigated. The results from these films are discussed in chapter 3.

In chapter 4 results from four CoFe thin films are presented. While all films were of similar total thickness, 50 nm, the differences were the inclusion or otherwise of a seedlayer and the introduction of nonmagnetic spacer layers to form laminate films. The detailed mechanisms for easy and hard axis reversals of the films were investigated. As expected cross-tie walls were observed in the films with thicker CoFe layers and wall displacements were seen with the introduction of the spacer layers. Magnetisation dispersion was reduced as multilayering was introduced and a significant reduction in the grain size from 12.5 ± 2.8 nm to 7.9 ± 1.5 nm was observed. In the laminated films with three spacer layers defect areas where the magnetisation distribution differed markedly from that in the surrounding film were observed and the formation of 360° domain walls was noted. Cross-sectional TEM showed that the layer roughness increased throughout the film thickness and this was thought to be the probable cause of the localised anomalies.

Chapter 5 follows on from chapter 4 with an investigation into the origin of the defect areas and 360° domain walls. The easy and hard axis magnetisation reversals for four CoFe laminate films were investigated. The main differences between these films and those investigated in chapter 4 was the reduction in spacer layer thickness and variation of CoFe layer thickness. In this case the presence of physical defects which significantly influenced the reversal behaviour were noted. A high density

of 360° domain walls which persisted up to fields of a few hundred oersteds were observed. The walls remained throughout reversal and the likely processes which occur during the reversal are presented. A quantitative investigation with DPC revealed that although some of the 360° domain walls exist in only one or two layers of the laminate films there are occasions where the walls exist throughout the whole thickness of the film. However, the end points of the 360° domain walls are still not understood.

In an attempt to gain an understanding of the physical structure of the defects and some insight into what happened where the 360° domain walls ended, SEM, cross-sectional TEM and EELS have been carried out and the results are presented at the end of chapter 5 and in chapter 6. The defects were found to originate from particles present on the substrate before the deposition of the CoFe films. The identity of the particles is still unknown, however, due to the regularity of the particles they are thought to be caused from some process after the etching of the substrate and not from handling. Cross-sectional TEM revealed the spacer layers are effective at separating the magnetic layers although there are some instances where the growth in one layer may be affected by that in an underlying layer.

In chapter 7 the final experimental work which explores the reversal mechanisms occurring in patterned films is presented. Rather than doing the investigation on the complex CoFe multilayers, six permalloy shapes with similar dimensions to a write head were studied. It was found that pole tips with widths of 500 nm and $1\ \mu\text{m}$ were influenced significantly by the reversal occurring within the whole shape. This study revealed the obstacles which the CoFe films with well defined anisotropy have to overcome when patterned down to write head dimensions.

Finally, the conclusions from the experimental studies are discussed in chapter 8 along with future work which could be carried out.

Acknowledgements

First and foremost I would like to thank my supervisors Dr Stephen McVitie and Professor John Chapman for their advice and guidance throughout my PhD, I couldn't have done it without them.

I would also like to express my gratitude to Dr Maureen MacKenzie for all her help with the Tecnai F20 and EELS analysis not to mention letting me use her office sink - sorry for the disturbance!

For all his efforts to keep the microscopes running and fix the numerous problems asap I would like to thank Dr Sam McFadzean. Thankyou to Brian Miller for helping to prepare some of the more tricky cross-sectional samples. Thanks to Dr Damien McGrouther for the help with the collection of the SEM/FIB data and Dr Nils Weiss for his help with the electron beam lithography I would also like to thank Billy and Colin for their technical assistance when needed and for being around for the occasional gossip. . A big thankyou to the people at Seagate technology in Northern Ireland, specifically Alan Johnston, Denis O'Donnell and PJ Doherty, for providing samples and some good hospitality when I visited Derry.

For the occasional night out and the annual outings I would like to thank everyone in the SSP group. To name a few past and present Susan, Paula, James, Gary, Craig, Paul, Damien, Nils and Clair for the office/coffee chat.

Finally I would like to say a huge thankyou to all my friends and family who have supported me over the last three years. Although, despite numerous explanations, none of them are 100% sure what I've been doing!

Declaration

This thesis is a record of the work carried out by myself in the Department of Physics and Astronomy at the University of Glasgow during the period October 2003 - September 2006. The work described herein is my own, apart from the sputter deposition of samples and the B-H loop measurements which were carried out by Denis O'Donnell and Patrick Doherty at Seagate Technology, Northern Ireland and the deposition of the soft films in chapter 3 which was performed by Bill Egelhoff at the National Institute of Standards and Technology (NIST), USA.

Some of the work reported in this thesis can be found in the following paper:

1. Transmission Electron Microscopy study of CoFe films with high saturation magnetization, **B. R. Craig, S. McVitie, J. N. Chapman, D. O. O'Donnell and A. B. Johnston**
J. Appl. Phys. 100, 053915 (2006)

This thesis has not previously been submitted for a higher degree.

Contents

Abstract	i
Acknowledgements	iv
Declaration	v
Contents	vi
List of Tables	xi
List of Figures	xii
1 Ferromagnetic thin films and their use in magnetic recording	1
1.1 Introduction	1
1.2 Ferromagnetism in Thin Films	2
1.2.1 Energy Terms in a Ferromagnet	3
1.2.2 Zeeman Energy	3
1.2.3 Exchange Energy	4
1.2.4 Anisotropy Energy	4

1.2.5	Magnetoelastic energy and magnetostriction	6
1.2.6	Magnetostatic Energy	7
1.2.7	Domain Wall Energy	8
1.2.8	Total Energy	10
1.2.9	Hysteresis Loop	11
1.3	Principles of Magnetic Recording	12
1.4	High Density Magnetic Recording	13
1.4.1	Longitudinal Magnetic Recording	13
1.4.2	Perpendicular Magnetic Recording	15
1.5	Write Head Materials for Perpendicular Magnetic Recording	16
1.5.1	CoFe as a Write Head Material	17
1.6	Summary	19
2	Instrumentation and Experimental Techniques	24
2.1	Introduction	24
2.2	Sample Preparation and Characterisation of Films	25
2.2.1	Deposition of Thin Magnetic Films	25
2.2.2	Bulk Characterisation with the B-H loopers	26
2.3	Transmission Electron Microscopy (TEM)	27
2.3.1	The Electron Gun	28
2.3.2	The Microscope Column	29
2.3.3	Diffraction	32
2.3.4	Bright Field and Dark Field Imaging	32

2.3.5	Magnetic Imaging	33
2.4	The Philips CM20	34
2.4.1	Fresnel Imaging	35
2.4.2	Differential Phase Contrast (DPC)	36
2.5	The FEI Tecnai 20	38
2.6	The FEI Tecnai F20	38
2.6.1	STEM Bright and dark field Imaging	39
2.6.2	Electron Energy Loss Spectroscopy (EELS)	40
2.6.3	The EELS spectrometer	42
2.6.4	Spectrum Imaging	43
2.7	The Scanning Electron Microscope and Focused Ion Beam System	44
2.8	Preparation of Cross-sectional Specimens	45
2.9	Electron Beam Lithography and the Lift-off Process	46
3	Characterisation of extremely soft ferromagnetic thin films	50
3.1	Introduction	50
3.2	Physical microstructure of NiFeCuMo and CoFeB thin films	51
3.3	Reversal mechanisms of NiFeCuMo and CoFeB thin films	52
3.3.1	Fresnel studies of NiFeCuMo	53
3.3.2	Fresnel studies of CoFeB	58
3.4	Discussion	63

4	Magnetic characterisation of CoFe single and multilayer films	66
4.1	Introduction	66
4.2	B-H loop measurements	68
4.3	Easy and hard axis reversal mechanisms of CoFe single layer films	69
4.4	Easy and hard axis reversal mechanism of the CoFe bilayer system	75
4.5	Easy and hard axis reversal mechanism of the CoFe quadrilayer system	80
4.6	Cross-sectional TEM of the CoFe films	86
4.7	Discussion	87
5	Investigation of 360° domain walls in CoFe multilayer films	93
5.1	Introduction	93
5.2	B-H loop measurements	95
5.3	Observation of stable 360° domain walls	95
5.4	DPC investigation of the 360° domain walls	113
5.5	Physical microstructure and elemental composition of planar samples	119
5.6	Discussion	124
6	Structural properties of the CoFe thin Films	128
6.1	Introduction	128

6.2	SEM of film M5	129
6.3	Cross-sectional TEM of CoFe thin films	131
6.4	EELS investigation of CoFe laminate films	133
6.5	Discussion	140
7	Patterned soft magnetic films	144
7.1	Introduction	144
7.2	Fresnel Studies of Patterned Permalloy films	145
7.3	Discussion	157
8	Conclusions and Future Work	161
8.1	Introduction	161
8.2	Conclusions	162
8.3	Future Work	165

List of Tables

4.1	Reference table for film structures M1, M2, M3 and M4 .	67
5.1	Description of samples M5, M6, M7 and M8. All four films have a 1 nm NiFe seed layer and 1.25 nm Al ₂ O ₃ spacer layer.	94

List of Figures

1.1	Illustration of the stray fields generated in (a) single domain state, (b) and (c) multidomain states and (d) a flux-closure state.	8
1.2	Planar view schematic illustrations of (a) Bloch-type wall, (b) Néel-type wall, (c) Cross-tie wall, (d) linear 360° domain wall and (e) 360° domain wall loop.	10
1.3	A typical ferromagnet hysteresis loop.	12
1.4	Schematic diagram of the magnetic recording process . . .	13
1.5	Illustration of a longitudinal ring head	14
1.6	Illustration of a perpendicular single pole head showing (a) the SUL and (b) the image head.	16
2.1	Schematic illustration of sputter deposition.	26
2.2	Simplified ray diagram for image formation in conventional TEM.	30
2.3	Schematic of (a) diffraction, (b) bright field and (c) dark field imaging modes.	33
2.4	Modified objective lens region in the Philips CM20 microscope.	35

2.5	(a) Schematic ray diagram for image formation in the Fresnel imaging mode and (b) Example Fresnel image. The yellow arrow indicates the magnetisation direction.	36
2.6	(a) Schematic of image formation in DPC and (b) Example DPC images. The yellow arrows indicate the direction of induction which the corresponding image is sensitive to.	37
2.7	Schematic illustration of the Tecnai double tilt rod.	38
2.8	Schematic illustration of STEM detectors on the Tecnai F20 where the collection angles follow the following relationship $\theta_3 > \theta_2 > \theta_1$. The BF detector collects the direct electron beam and low angle scattered electrons whereas the ADF and HAADF detectors collect those electron scattered to higher angles.	40
2.9	Example of an EELS spectra from the CoFe multilayer samples showing (a) the low loss region and (b) the core loss region.	41
2.10	Schematic illustration of the main parts of the Gatan Enfina spectrometer.	43
2.11	Schematic illustration of spectrum image acquisition.	44
2.12	Schematic illustration of a cross-sectional specimen.	45
2.13	Schematic of the steps involved in the lift-off process. (a) the two layers of resist on top of the sample, (b) the overhang profile created after e-beam exposure and developing, (c) metallisation and (d) after lift-off.	47
3.1	(a) and (b) Bright field TEM images of NiFeCuMo and CoFeB respectively and (c) and (d) corresponding diffraction patterns of NiFeCuMo and CoFeB.	52

3.2	Reversal along the hard axis of NiFeCuMo with red arrows indicating the direction of applied field and the white arrows the magnetisation direction	54
3.3	Hysteresis loop calculated from the Fresnel images for the hard axis of NiFeCuMo	55
3.4	Reversal along the easy axis of SF1, NiFeCuMo, with red arrows indicating the direction of applied field and the white arrows the magnetisation direction	56
3.5	Easy axis hysteresis loop calculated from the Fresnel images for NiFeCuMo	57
3.6	Easy axis symmetrised hysteresis loop for SF1, NiFeCuMo.	57
3.7	Reversal along axis 1 of SF2, CoFeB, with red arrows indicating the direction of applied field and the white arrows the magnetisation direction	59
3.8	Hysteresis loop calculated from the Fresnel images for SF2, CoFeB, axis 1	60
3.9	Symmetrised hysteresis loop for SF2, CoFeB, axis 1	60
3.10	Reversal along axis 2 of SF2 with red arrows indicating the direction of applied field and the white arrows the magnetisation direction	61
3.11	Hysteresis loop calculated from the Fresnel images for SF2 axis 2	62
3.12	Symmetrised hysteresis loop for SF2 axis 2	62
4.1	Schematic showing the structures of (a) CoFe (M1), (b) NiFe/CoFe (M2), (c) NiFe/CoFe/Al ₂ O ₃ /NiFe/CoFe (M3) and (d) NiFe/CoFe/(Al ₂ O ₃ /CoFe/NiFe) _{x3} (M4).	67

4.2	Easy and Hard axis B-H loops for (a) M1, (b) M2, (c) M3 and (d) M4	68
4.3	Easy axis magnetisation reversal of M1, CoFe50 nm, with red arrows indicating the direction of applied field and the white arrows the mean magnetisation direction.	70
4.4	Easy axis magnetisation reversal of M2, NiFe1nm/CoFe50nm, with red arrows indicating the direction of applied field and the white arrows the magnetisation direction. The green circles indicated vortex/crosstie pair along the crosstie domain wall.	73
4.5	Hard axis magnetisation reversal of M2, NiFe1nm/CoFe50nm, with red arrows indicating the direction of applied field and the white arrows the magnetisation direction.	74
4.6	Easy axis magnetisation reversal of M3, NiFe1nm/CoFe22.5nm/Al ₂ O ₃ 1.5nm/NiFe1nm/CoFe22.5nm, with red arrows indicating the direction of applied field and the white arrows the magnetisation direction.	77
4.7	Hard axis magnetisation reversal of M3, NiFe1nm/CoFe22.5nm/Al ₂ O ₃ 1.5nm/NiFe1nm/CoFe22.5nm, with red arrows indicating the direction of applied field and the white arrows the magnetisation direction.	78
4.8	Magnetisation reversal of M3, NiFe1nm/CoFe22.5nm/Al ₂ O ₃ 1.5nm/NiFe1nm/CoFe22.5nm, 1° from the hard axis with red arrows indicating the direction of applied field and the white arrows the magnetisation direction.	79

4.9	Schematic diagram showing (a) displaced and (b) superposed Néel walls.	80
4.10	Easy axis magnetisation reversal of film M4, NiFe1nm/CoFe10nm/(Al ₂ O ₃ 1.5nm/NiFe1nm/CoFe10nm)x3, with red arrows indicating the direction of applied field and the white arrows the magnetisation direction.	81
4.11	Hard axis magnetisation reversal of M4, NiFe1nm/CoFe10nm/(Al ₂ O ₃ 1.5nm/NiFe1nm/CoFe10nm)x3, with red arrows indicating the direction of applied field and the white arrows the magnetisation direction.	82
4.12	TEM images of M4 (a) at a region without a defect (b) at defect region	83
4.13	Easy axis magnetisation reversal of M4, NiFe1nm/CoFe10nm/(Al ₂ O ₃ 1.5nm/NiFe1nm/CoFe10nm)x3, at a defect region with red arrows indicating the direction of applied field and the white arrows the magnetisation direction. The green circle indicates a 360° domain wall.	84
4.14	Hard axis magnetisation reversal of M4, NiFe1nm/CoFe10nm/(Al ₂ O ₃ 1.5nm/NiFe1nm/CoFe10nm)x3, at a defect region with red arrows indicating the direction of applied field and the white arrows the magnetisation direction.	85
4.15	Bright field TEM image of (a) NiFe10nm/CoFe500nm and (b) NiFe10nm/CoFe100nm/(Al ₂ O ₃ 15nm/NiFe10nm/CoFe100nm)x3	87

5.1	Schematic illustration of (a) M5, (b) M6, (c) M7 and (d) M8	94
5.2	Easy and Hard axis B-H loops for (a) M5, (b) M6, (c) M7 and (d) M8	95
5.3	Easy axis magnetisation reversal of M7, NiFe1nm/CoFe10nm/ Al ₂ O ₃ 1.5nm/NiFe1nm/CoFe10nm, showing repeated end points of a magnetisation cycle. Red arrows indicate the direction of applied field and the white arrows the magnetisation direction. The coloured ovals highlight 360° domain walls which remain throughout at least one cycle of reversal.	97
5.4	Easy axis magnetisation reversal of M5, NiFe1nm/CoFe10nm/ (Al ₂ O ₃ 1.5nm/NiFe1nm/CoFe10nm)x3 with red arrows indicating the direction of applied field and the white arrows the magnetisation direction. The green circles highlight a 360° domain wall which remains throughout reversal.	99
5.5	Bright field TEM images showing typical defect areas in films (a) M5 and (b) M7.	100
5.6	Hard axis magnetisation reversal of M5, NiFe1nm/CoFe10nm/ (Al ₂ O ₃ 1.5/NiFe1nm/CoFe10nm)x3 with red arrows indicating the direction of applied field and the white arrows the magnetisation direction. The green circles highlight a 360° domain wall which remains throughout reversal.	101

5.7	Easy axis magnetisation reversal of M6, NiFe1nm/CoFe22.5nm/(Al ₂ O ₃ 1.5nm/NiFe1nm/CoFe22.5nm)x3 with red arrows indicating the direction of applied field and the white arrows the magnetisation direction.	103
5.8	Hard axis magnetisation reversal of M6, NiFe1nm/CoFe22.5nm/(Al ₂ O ₃ 1.5nm/NiFe1nm/CoFe22.5nm)x3 with red arrows indicating the direction of applied field and the white arrows the magnetisation direction.	104
5.9	Easy axis magnetisation reversal of M7, NiFe1nm/CoFe10nm/ Al ₂ O ₃ 1.5nm/NiFe1nm/CoFe10nm, with red arrows indicating the direction of applied field and the white arrows the magnetisation direction. The green circles highlight a 360° domain wall which remains throughout reversal.	106
5.10	Hard axis magnetisation reversal of M7, NiFe1nm/CoFe10nm/ Al ₂ O ₃ 1.5nm/NiFe1nm/CoFe10nm with red arrows indicating the direction of applied field and the white arrows the magnetisation direction.	107
5.11	Easy axis magnetisation reversal of M8, NiFe1nm/CoFe5nm/(Al ₂ O ₃ 1.5nm/NiFe1nm/CoFe5nm)x3 with red arrows indicating the direction of applied field and the white arrows the magnetisation direction.	109
5.12	Hard axis magnetisation reversal of M8, NiFe1nm/CoFe5nm/(Al ₂ O ₃ 1.5nm/NiFe1nm/CoFe5nm)x3 with red arrows indicating the direction of applied field and the white arrows the magnetisation direction.	110

5.13	Schematic diagram showing hard axis reversal behaviour of 360° domain walls. The black and white colouring is used to illustrate the contrast observed in the Fresnel images.	112
5.14	Schematic diagram showing easy axis reversal behaviour of 360° domain walls	112
5.15	DPC image sequence during an easy axis reversal of M7, NiFe1nm/CoFe10nm/ Al ₂ O ₃ 1.5nm/NiFe1nm/CoFe10nm	114
5.16	Signal profile across a 180° domain wall. The blue rectangle indicates the area which the profile was taken over.	115
5.17	Signal profile across a 360° domain wall. The blue rectangle indicates the area which the profile was taken over.	115
5.18	Schematic diagram of the signal generated from (a) 180° domain wall, (b) 360° domain wall present in 2 layers and (c) 360° domain wall present in 1 layer of a bilayer film. Domains are indicated in red and blue and the domain wall regions in green.	115
5.19	(a)-(d) DPC images of film M5. Red arrows indicate the direction of induction which the image is sensitive to. (e) corresponding bright field image. The coloured ovals highlight examples of 360° domain walls.	117
5.20	Signal profile across 180° and 360° domain walls in film M5. The blue rectangle indicates the area which the profile was taken over. The red arrow indicates the direction of induction which the image is sensitive to.	117
5.21	Signal profile across a 360° domain wall in film M5. The blue rectangle indicates the area which the profile was taken over. The red arrow indicates the direction of induction which the image is sensitive to.	118

5.22	Signal profile across a 360° domain wall in film M5. The blue rectangle indicates the area which the profile was taken over. The red arrow indicates the direction of induction which the image is sensitive to.	118
5.23	Schematic diagram of a 360° domain wall present in (a) one layer and (b) two layers of a quadrilayer film. Domains are indicated in red and domain walls in green. . .	118
5.24	Bright field TEM image of a defect showing the visible crystallites within the annular defect.	119
5.25	HAADF images of (a) defect site 1 and (b) defect site 2 showing the corresponding spectrum image line traces. Spectra, normalised with respect to the O K-edge, taken from points a,b and c on the line traces are shown in (c) and (d) for spectrum image 1 and 2 respectively.	122
5.26	Graph showing the element profiles of O, Fe and Co across spectrum image 1. The t/λ profile is also shown.	123
5.27	Graph showing the element profiles of O and Fe across spectrum image 2. The t/λ profile is also shown.	123
5.28	Schematic illustration of (a) 360° domain wall, (b) 360° compensating wall and (c) 0° compensating wall. The red areas indicate the domains and the green areas indicate the domain wall region.	125
6.1	(a) and (b) SEM image of the surface of M5 showing the defects, (c) and (d) cross-sectional SEM images of the defects showing the multilayer film on top of the defect. .	130

6.2	(a) BFTEM and (b) DFTEM of M5, NiFe1nm/CoFe10nm/(Al ₂ O ₃ 1.25nm/NiFe1nm/CoFe10nm)x3. (c) BFTEM and (d) DFTEM images of M9, NiFe1nm/CoFe22.5nm/(Al ₂ O ₃ 1.5nm/NiFe1nm/CoFe22.5nm)x7.	132
6.3	(a) Survey image showing spectrum image region, (b) spectrum image and (c) elemental profiles across the spectrum image of NiFe1nm/CoFe10nm/(Al ₂ O ₃ 1.25nm/NiFe1nm/CoFe10nm)x3.	134
6.4	Typical EELS spectra taken from (a) a CoFe layer, (b) a NiFe seed layer and (c) a Al ₂ O ₃ spacer layer in film M9, NiFe1nm/CoFe10nm/(Al ₂ O ₃ 1.25nm/NiFe1nm/CoFe10nm)x3.	136
6.5	(a) Survey image showing spectrum image region, (b) spectrum image and (c) elemental profiles across the spectrum image of NiFe1nm/CoFe10nm/(Al ₂ O ₃ 1.25nm/NiFe1nm/CoFe10nm)x3.	137
6.6	(a) Survey image showing spectrum image region, (b) elemental maps of O, Fe, Co and Ni. (c) elemental profiles across the spectrum image of NiFe1nm/CoFe22.5nm/(Al ₂ O ₃ 1.5nm/NiFe1nm/CoFe22.5nm)x7.	139
7.1	Schematic diagram of head shapes (a) H1, (b) H2, (c) H3, (d) H4, (e) H5 and (f) H6.	145
7.2	Fresnel reversal of H1. Red and white arrows indicate the direction of applied field and magnetisation direction respectively. The Black arrows indicate the magnetisation direction within the tip.	147
7.3	Schematic illustration of the Fresnel intensity in the tip of H1.	147

7.4	Fresnel reversal of H2. Red and white arrows indicate the direction of applied field and magnetisation direction respectively.	149
7.5	Schematic illustration of the Fresnel intensity in the tip of H2 at 0 Oe applied field.	149
7.6	Fresnel reversal of H3. Red and white arrows indicate the direction of applied field and magnetisation direction respectively. The Black arrows indicate the magnetisation direction within the tip.	151
7.7	Schematic illustration of the Fresnel intensity in the tip of H3.	151
7.8	Fresnel reversal of H4. Red and white arrows indicate the direction of applied field and magnetisation direction respectively.	153
7.9	Fresnel reversal of H5. Red and white arrows indicate the direction of applied field and magnetisation direction respectively.	154
7.10	Fresnel reversal of H6. Red and white arrows indicate the direction of applied field and magnetisation direction respectively.	156

Chapter 1

Ferromagnetic thin films and their use in magnetic recording

1.1 Introduction

Since IBM introduced the first disc drive in 1957 the storage density has grown by a factor of more than two million [1]. The data storage industry is constantly striving to maximise the storage in the smallest area possible. At present lab demonstrations have shown densities of ~ 200 Gbit/inch² and densities of 1 Tbit/inch² envisaged [2]. With this increase in density there is a dramatic scaling down of critical dimensions for recording heads and this leads to many design challenges.

For many years commercial disc drives have used the longitudinal mode of recording. Whilst this mode of recording can still be used for storage at high densities, it is approaching the superparamagnetic limit [3] where spontaneous demagnetisation can occur. The magnetic recording industry is now moving towards perpendicular recording which eliminates head to head or tail to tail transitions between 'bits'. In this mode the superparamagnetic limit is extended and higher storage densities can be achieved as discussed in section 1.4.2. Toshiba recently released the first commercial drive utilising perpendicular technology [4] with other companies such as Seagate following them [5, 6].

There are many challenges facing the industry with the move to perpendicular technology. A critical challenge is developing the material used in the write head. $\text{Co}_x\text{Fe}_{1-x}$ alloys have attracted a lot of interest as they possess a high known magnetic moment at room temperature and therefore are suitable candidates for writing to high coercivity materials. The advantages of using CoFe are discussed further in section 1.5.1.

To introduce the research carried out this chapter deals with the basics of ferromagnetism, magnetic recording and the use of CoFe as a write pole material.

1.2 Ferromagnetism in Thin Films

Ferromagnets are materials which possess a non-vanishing magnetic moment in the absence of an applied field. Ferromagnetism originates from the spin and orbital motion of the electrons within an atom inducing a magnetic moment. Weiss [7] described the interaction between neighbouring moments in terms of an internal molecular field, H_m , which is directly proportional to the magnetisation, M . Heisenberg [8] then showed the molecular field could be understood from quantum mechanical exchange interactions between unpaired electrons on adjacent atoms which promote the parallel alignment of the atomic moments. The energy associated with the exchange interactions is discussed further in section 1.2.3. The exchange interaction is overcome at temperatures above the Curie temperature, T_c , where the material becomes paramagnetic with randomly oriented atomic moments in the absence of an applied field.

The maximum moment of a ferromagnetic material is known as the saturation magnetisation, M_s , and occurs when all the atomic moments are aligned in the same direction by a high enough applied field. When the field is removed the material may retain a net moment in the direction of applied field. This moment is known as the remanent magnetisation,

M_r , and is usually considerably lower than M_s . The reduced moment can be explained through energy considerations, as discussed in section 1.2.1, which cause the magnetisation to break up into uniformly magnetised regions known as domains. The total moment of the material is the vector sum of the magnetic moments of the domains. In the presence of an applied field the net magnetisation increases in the direction of the applied field through either domain wall motion or coherent magnetisation rotation. It is possible to image and study the behaviour of domains in response to an applied field through techniques such as magnetic force microscopy (MFM) [9], the Bitter technique [10], the Kerr effect [11] and Lorentz microscopy [12].

1.2.1 Energy Terms in a Ferromagnet

There are many contributing energy terms which determine the total potential energy of a ferromagnet. These include the Zeeman energy, the exchange energy, the anisotropy energy, the magnetoelastic energy, the magnetostatic energy and the domain wall energy; they are discussed in sections 1.2.2 - 1.2.7. These terms dictate the micromagnetic behaviour of the ferromagnet such as domain formation, magnetisation reversal and hysteresis.

1.2.2 Zeeman Energy

The Zeeman energy is the energy within the specimen due to an external magnetic field and is given by

$$E_z = -\mu_0 \int_V \mathbf{M} \cdot \mathbf{H} dV \quad (1.1)$$

where μ_0 is the permeability of free space, H is the applied field and V is the sample volume. The applied field acts to align the magnetic

moments along its direction and is the Zeeman energy is a minimum for all moments aligned parallel along this direction.

1.2.3 Exchange Energy

The quantum mechanical exchange interaction between unpaired electrons on adjacent atoms causes minimisation of the electrostatic energy in the system and is responsible for the alignment of spin moments in a magnetic material. If two interacting electrons are considered from the Heisenberg approach [8], the exchange energy, e_{ex} , can be described by:

$$e_{ex} = -2J_{i,j}\mathbf{s}_i \cdot \mathbf{s}_j \quad (1.2)$$

where $J_{i,j}$ is the exchange coupling constant and s_i and s_j are the atomic electron spin moments. The overall exchange energy, E_{ex} , is found from summing the local exchange energies over the whole system. In most cases a nearest neighbour calculation is sufficient and the total exchange energy can be found from:

$$E_{ex} = -2J_{i,j}S^2 \sum_{i,j} \cos\phi_{i,j} \quad (1.3)$$

where S is the magnitude of the spin vector and $\cos\phi_{i,j}$ is the angle between the spins i and j . Thus for ferromagnetic materials where the exchange constant J is positive, the exchange energy is minimised when $\phi_{i,j} = 0$, i.e. for parallel spins. Hence, the magnetic moments of the sample align to give a non-zero magnetisation.

1.2.4 Anisotropy Energy

Another term which contributes to the total magnetic energy of a ferromagnetic system is the anisotropy energy. Spin-orbit interactions are

one source of anisotropy in single crystals and direct the magnetisation along preferred crystallographic directions referred to as easy axes. The directions which require the largest amount of work to align the magnetisation along are known as hard axes. The anisotropy is dependent on the crystallographic symmetry of the material.

The anisotropy energy, E_k , of a hexagonal or uniaxial crystal such as Co can be expressed as a series expansion:

$$E_k = \int (K_1(1 - \alpha_3^2) + K_2(1 - \alpha_3^2)^2) dV \quad (1.4)$$

where K_1 and K_2 are anisotropy constants and α_3 is the direction cosine with respect to the unique axis. There are three anisotropy possibilities in hexagonal crystals. The first is when the easy axis prefers to lie parallel to the anisotropy axis and occurs if K_1 is large and positive. However, if K_1 is large and negative, the easy axis prefers to lie perpendicular to the anisotropy axis. The final case occurs when $-2 < K_1/K_2 < 0$ and the magnetisation prefers to lie on a cone of angle θ to the anisotropy axis.

For a cubic crystal such as Fe the situation is more complicated due to the higher degree of symmetry. The anisotropy energy in this case can also be expressed as a series expansion:

$$E_k = \int [K_1 (\alpha_1^2 \alpha_2^2 + \alpha_2^2 \alpha_3^2 + \alpha_3^2 \alpha_1^2) + K_2 \alpha_1^2 \alpha_2^2 \alpha_3^2] dV \quad (1.5)$$

where α_1 , α_2 and α_3 are direction cosines along the crystallographic axes. The integration is performed over the volume of the solid, although due to thermal fluctuations the higher order terms average out and only the first two terms generally need be considered. The anisotropy constant K_1 has the largest effect on determining the preferred crystallographic direction. Common easy directions in cubic crystals are $\langle 111 \rangle$, $\langle 110 \rangle$ and $\langle 100 \rangle$.

For the polycrystalline CoFe films investigated in this thesis an easy direction has been induced by deposition in an applied field of ~ 60 Oe (around the same order of magnitude to that used in previous studies on high moment materials [13]). Variation in the easy direction due to the orientation of individual crystallites causes fluctuations of the magnetisation about the easy direction and this is seen as magnetisation ripple [14, 15] and is discussed further in section 1.5.1.

1.2.5 Magnetoelastic energy and magnetostriction

Ferromagnetic materials can be subject to mechanical deformations under an applied magnetic field or on ordering into domains when cooled below their Curie temperature. The deformation arises from interactions between neighbouring atomic moments and is known as the magnetostriction. The separation between the atomic moments due to magnetostriction changes with the magnetic field. The magnetostriction, λ , is defined as the fractional length change, $\delta l/l$, and the saturation value, λ_s , occurs when the magnetisation in the direction of the applied field is equal to M_s .

The magnetoelastic energy is associated with the stress and the direction of spontaneous magnetisation and can be expressed as

$$E_\lambda = \int \left(\frac{3}{2} \lambda_s \sigma \sin^2 \alpha \right) dV \quad (1.6)$$

where σ is the tension in the system due to the applied field and α is the angle between the saturation magnetisation and σ . A fuller description of magnetostriction can be found in reference [16].

1.2.6 Magnetostatic Energy

The magnetostatic energy, E_m , is partly responsible for the formation of domains within a ferromagnet. It arises from the Coulomb interactions between magnetic dipoles present in the specimen. Both an external stray field and an internal demagnetising field are generated by the magnetic charges. The potential of the stray field for a volume, V , and surface area, S , can be expressed as

$$\Phi_m = \frac{1}{4\pi} \left(\int_V \frac{-\nabla \cdot \mathbf{M}}{R} dV + \int_S \frac{\mathbf{M} \cdot \mathbf{n}}{R} dS \right) \quad (1.7)$$

where R is the position vector for the point in space where the field from the charge is evaluated and \mathbf{n} is the outward pointing unit vector, normal to the surface. $\nabla \cdot \mathbf{M}$ is the magnetic volume charge and $\mathbf{M} \cdot \mathbf{n}$ is the magnetic surface charge. The Stray field, H_m can then be derived from

$$\mathbf{H}_m = -\nabla \Phi_m \quad (1.8)$$

The magnetostatic energy contributions can then be written as

$$E_m = \frac{\mu_0}{2} \int \mathbf{H}_m^2 dV \quad (1.9)$$

where μ_0 is the permeability of free space integrated over all space. The extent of the demagnetising effect is strongly dependent on the sample geometry, i.e. E_m decreases when the volume occupied by the stray field decreases. Hence, by formation of domains, E_m is reduced and a multidomain state, as illustrated in figure 1.1b-d, is preferred. However, increasing the number of domains increases the exchange energy due to the large angle between spins within the domain walls, thus the magnetostatic energy and exchange energy are in direct competition. The flux

closure state, figure 1.1d, has minimal stray field and is the preferred state when there is little or no Zeeman energy and anisotropy.

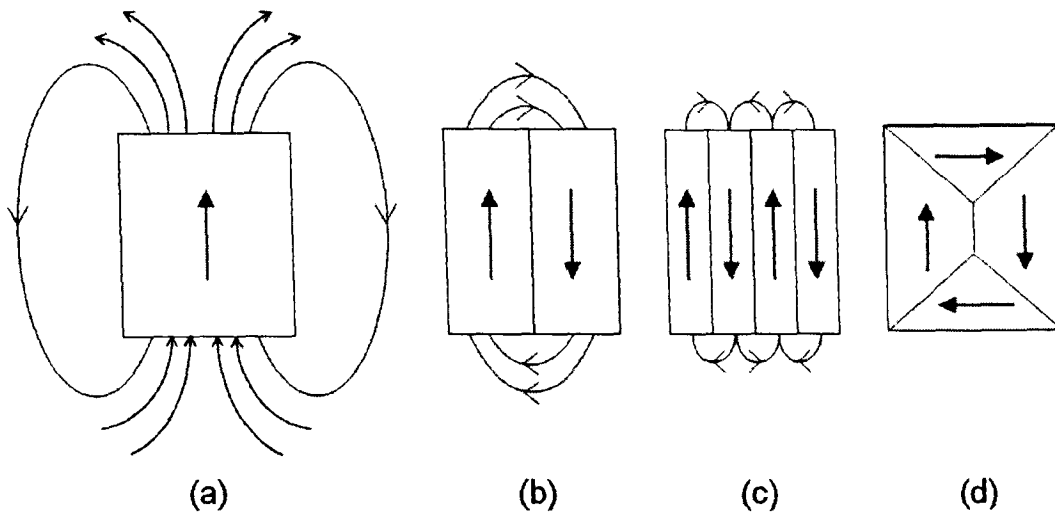


Figure 1.1: Illustration of the stray fields generated in (a) single domain state, (b) and (c) multidomain states and (d) a flux-closure state.

1.2.7 Domain Wall Energy

The transition regions which separate domains are called domain walls. The magnetisation rotates coherently between the directions of magnetisation in neighbouring domains. There are various types of domain walls as illustrated in figure 1.2. The occurrence of these walls is dependent on sample thickness. In a Bloch wall (figure 1.2a) the magnetisation rotates perpendicular to the plane of the surface and only occurs in thicker films and bulk material [17] due to the surface magnetostatic energy. As the film thickness is reduced and the magnetostatic energy becomes significant Néel walls form (figure 1.2b). In this case the magnetisation vector rotates within the plane of the film. The Néel wall has magnetostatic charges on each of the wall surfaces within the film. As a consequence of this, for a constant wall width, the magnetostatic energy is reduced as the thickness decreases. In multilayer films Néel walls tend to be attracted to each other and can form double walls as seen in chapter 4.

In bulk materials with uniaxial anisotropy in which Bloch walls occur, the energy associated with a domain wall, E_w , and the domain

wall width, δ , are determined by competing exchange interactions and anisotropy. The anisotropy energy acts to decrease the wall thickness as it is minimised by the moments aligning along the anisotropy axis whereas the exchange energy prefers a wider wall since it is minimal when neighbouring moments are parallel. In this case the domain wall width is given by $\delta = \pi\sqrt{\frac{A}{K_u}}$ where A is the exchange stiffness and K_u is the uniaxial anisotropy constant. For thin films where $t \leq \sqrt{\frac{A}{K_u}}$ Néel walls occur. The domain wall width scales with $\sqrt{\frac{A}{K_d}}$ where K_d is the stray field exchange constant and is given by $K_d = \mu_0 M_s^2 / 2$. As $K_d \gg K_u$, δ for Néel walls is narrower than in a Bloch wall.

Another type of domain wall which is observed in ferromagnetic materials is the cross-tie wall (figure 1.2c) [17]. This wall can form in films where the thickness is in the transition region between the Bloch and Néel walls. The magnetisation in a cross-tie wall rotates both in and out of the plane of the film, i.e. a combination of Bloch and Néel type walls.

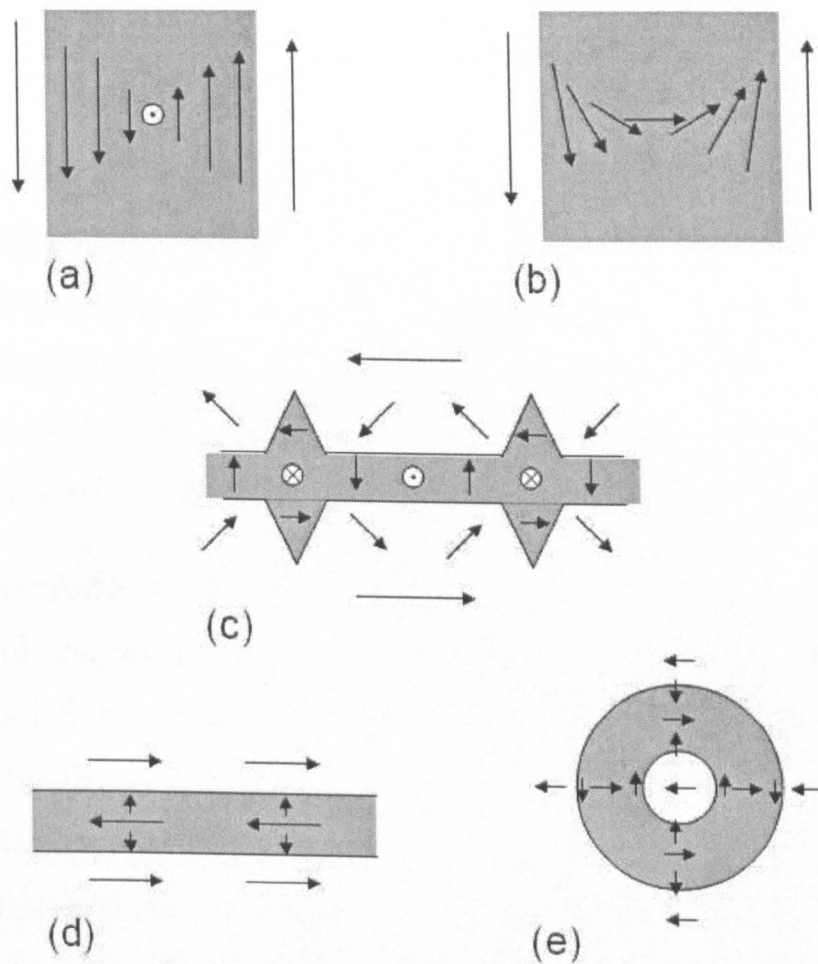


Figure 1.2: Planar view schematic illustrations of (a) Bloch-type wall, (b) Néel-type wall, (c) Cross-tie wall, (d) linear 360° domain wall and (e) 360° domain wall loop.

The last type of wall considered here is the 360° domain wall. The magnetisation on either side of this type of wall lies in the same direction. Linear 360° domain walls (figure 1.2d) often form during reversal sequences in thin films and there are several examples of this in chapters 4 and 5. The linear walls can join up to form 360° domain wall loops (figure 1.2e) which have been observed previously by TEM and are particularly stable [18, 19].

1.2.8 Total Energy

The total magnetic energy of a ferromagnet can be found from summation of all the energy contributions,

$$E_{tot} = E_z + E_{ex} + E_a + E_\lambda + E_m \quad (1.10)$$

A magnetic system at any time tries to minimise E_{tot} . However, the magnetic configuration is dependent on the history of the particular sample as the magnetic moments can get trapped at local energy minima and it is common for domains to be present in minimum energy configurations. The direction of the magnetic moments can be changed under an applied field and hysteretic behaviour such as domain processes can occur.

Through calculation and minimisation of the total energy it is possible to model magnetic systems and predict the behaviour in response to an applied field. There are many widely used micromagnetic packages based on finite difference [20] or finite element methods [21] which enable modelling on the nanometre scale and can be useful in understanding experimental observation. For example Schrefl et al simulated the formation and elimination of 360° domain walls in thin Co films [22] which is relevant to the experimental observations in chapter 5.

1.2.9 Hysteresis Loop

The hysteresis loop for a magnetic material is a plot of the magnetisation, M , against the applied field, H . A schematic of a typical hysteresis loop for a ferromagnet is shown in figure 1.3. When initially deposited, the net magnetic moment for thin magnetic films is usually zero. On application of a field the magnetisation then increases until saturation, M_s , is reached. This initial part of the hysteresis loop can only be reproduced if the ferromagnet is demagnetised. On reducing the applied field to zero the magnetisation then reduces to a value M_r , the remanence. As the field is increased in the opposite direction the magnetisation goes to zero when $H = H_c$, the coercivity. Hysteresis loops for ferromagnets are typically symmetric and centred about zero, as is the case for the thin films investigated in this thesis.

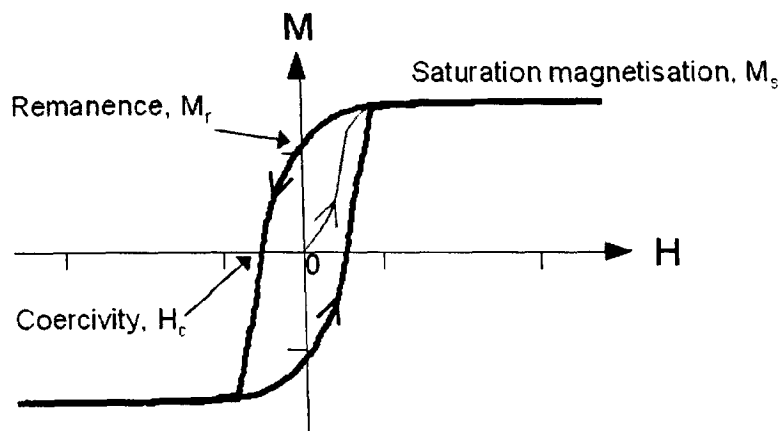


Figure 1.3: A typical ferromagnet hysteresis loop.

1.3 Principles of Magnetic Recording

Magnetic recording first began with Poulsen's experiments in 1898 [23] and over the past few decades there has been rapid advancement of the technology. A schematic of the recording process is shown in figure 1.4. In the recording system a current is generated in the write head by an input signal which in turn generates a field from the head. This field is then used to write the information to the magnetic recording media and information is stored in binary form as a series of magnetic domains known as 'bits'. The information can then be read back through sensing the stray field from the transition regions between the bits. This is done by the read head and the signal is then converted electronically to give an output signal.

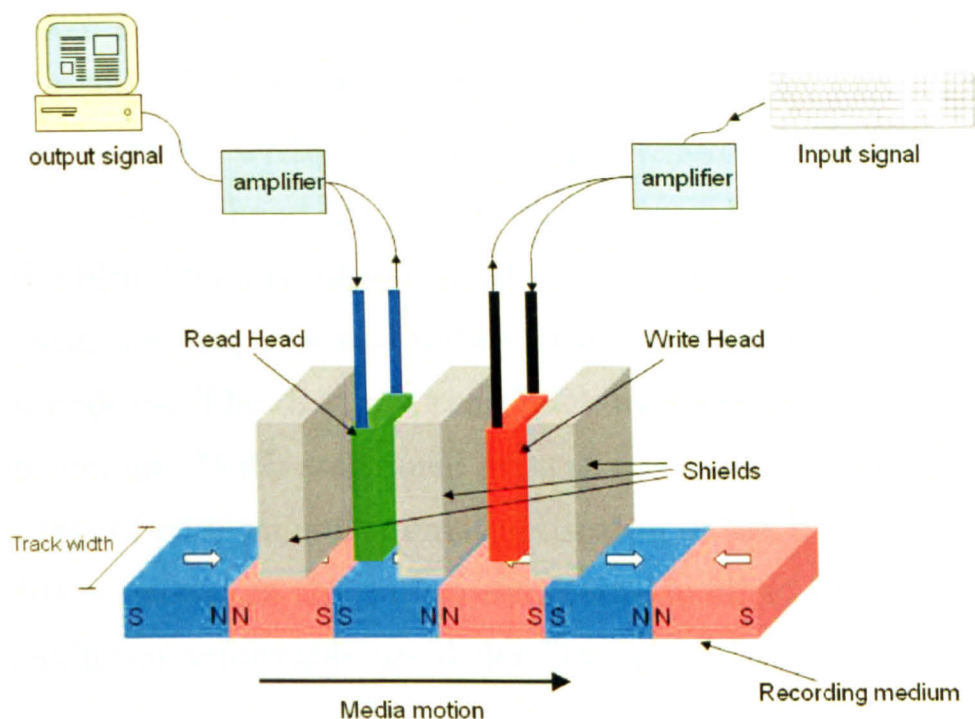


Figure 1.4: Schematic diagram of the magnetic recording process

1.4 High Density Magnetic Recording

The growing demand for storage on servers and personal computers means the industry is constantly striving to maximise the storage density. Storage densities are usually quoted in terms of areal densities, i.e. bits per unit area, however, the areal density can also be considered in terms of a track density (the number of tracks per unit width of the film) and a linear density (the number of bits per unit length of track). In essence, to increase the areal storage density the bit size should be reduced.

In this section various formats which have shown potential for high density magnetic recording are discussed.

1.4.1 Longitudinal Magnetic Recording

The longitudinal mode of magnetic recording is used in the majority of current commercial hard disc drives. A schematic of a longitudinal write

head is shown in figure 1.5. The head is a ring head and the magnetisation is written by the fringing fields from the head gap. This gives a maximum possible write field of $\sim M_s/2$ where M_s is the saturation magnetisation of the head [24]. The magnetisation of the bits lies in the plane of the film which results in head to head and tail to tail transitions between neighbouring bits and unfavourable demagnetising fields at the transition regions. The data are read back by sensing the fields from the transition regions. With continued growth in the areal recording density there is a risk of spontaneous demagnetisation of the bits due to thermal effects, this is known as the superparamagnetic effect and places a limit on the maximum achievable areal density [3].

Other factors which can limit the storage density are media parameters and write head characteristics. The demagnetising length is given by $M_r t / H_c$ [25] where M_r is the remanent magnetisation, t is the thickness of the media and H_c is the coercivity of the media. From the relationship it can be seen that the demagnetising length is smaller for smaller t . For greater areal densities smaller bit sizes are required which requires a smaller demagnetising length, hence, constraints are put on the film thickness.

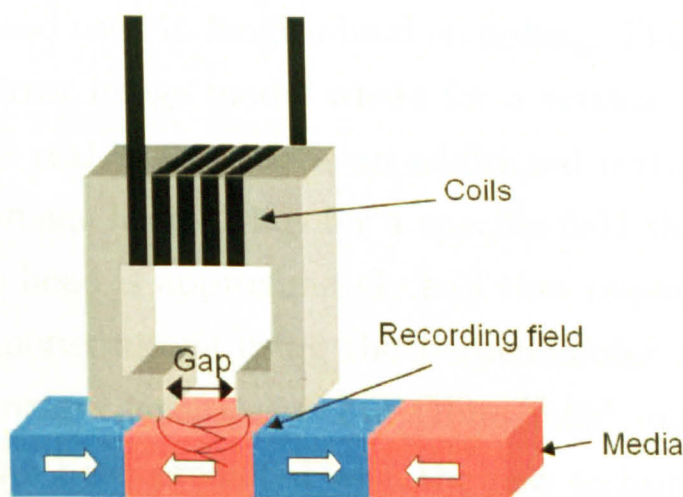


Figure 1.5: Illustration of a longitudinal ring head

1.4.2 Perpendicular Magnetic Recording

Iwasaki and Nakemura [26] renewed interest in perpendicular recording nearly 3 decades ago when they showed its potential for high density recording. Figure 1.6 shows a schematic of the writing process in the perpendicular mode of recording. In this mode the magnetisation of the bits is written perpendicular to the plane of the media by the direct field from the single pole head. The demagnetising effects which limit the areal density in the longitudinal mode are eliminated. In fact the demagnetising fields present in this mode support the opposite magnetisation of neighbouring bits [27] and therefore improve the thermal stability. Hence the superparamagnetic limit is extended.

The soft underlayer (SUL), as illustrated in figure 1.6a, provides an efficient return path for the magnetic flux emitted from the pole tip. In simple models the SUL can be considered as a mirror image of the head, figure 1.6b and thus in a perfect situation could effectively double the write field to $\sim M_s$ [28]. This enables writing to a higher coercivity medium and therefore higher areal densities can be achieved thereby further deferring the density at which the superparamagnetic limit comes into effect. It is also worth noting the single pole head is more efficient than the ring head used in longitudinal recording. This can be explained through the mirror image model where for a vertical field generated by a current in the real head there is an additional vertical field generated by the mirror image head. Thus for a specific field the current required in a single pole head is approximately half that required in a ring head. Recent lab demonstrations using the perpendicular mode of recording have shown storage densities of 245 Gbits/inch² and densities of 500 Gbits/inch² have been predicted with the new technology [29].

There are many other aspects which need to be considered for optimisation of the recording system. For example the shape of the write pole, head flying height, signal to noise ratio and recording medium thickness

[30, 31, 32].

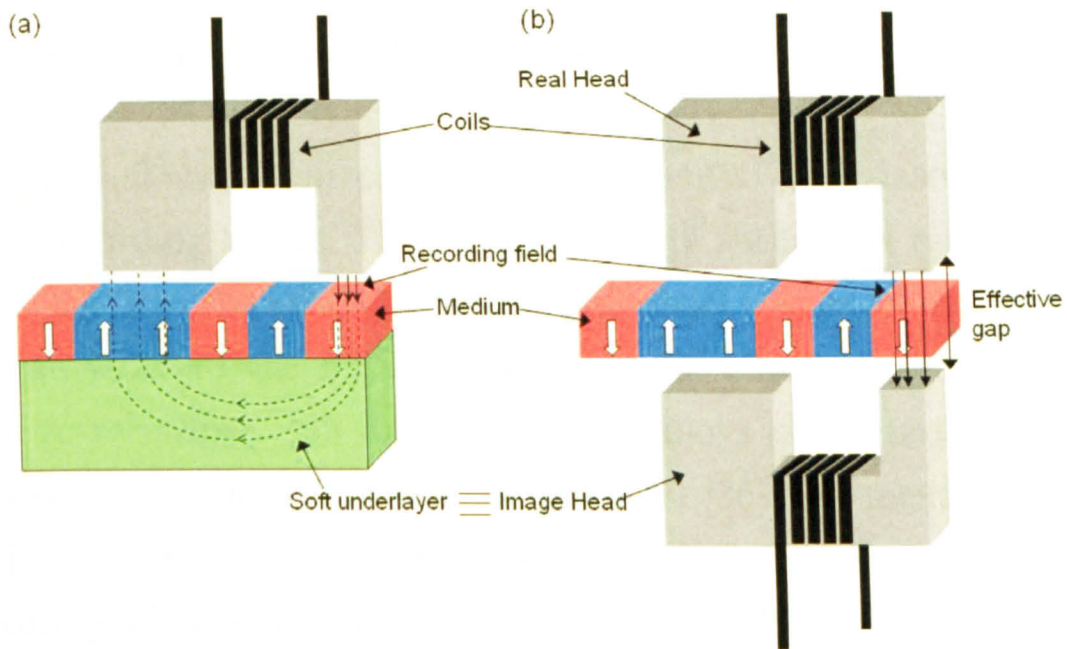


Figure 1.6: Illustration of a perpendicular single pole head showing (a) the SUL and (b) the image head.

1.5 Write Head Materials for Perpendicular Magnetic Recording

One of the main requirements for an effective single pole head is the capability to provide a large enough write field to record onto the high coercivity media required for high density magnetic recording. Also, to avoid the head retaining a remanent magnetisation which could disturb previously written data, it is important for the material to have a low coercivity and low remanence. FeN films have been pursued as possible candidates as they have saturation flux densities of ≥ 2 T and are capable of writing to media with coercivities up to ~ 5100 Oe [33]. Komuro et al. [34] reported a saturation flux density of 2.8 T for a Fe_{16}N_2 film. However this value of saturation flux density has only been found in samples which were grown by molecular beam epitaxy which is not practical for large scale manufacture. CoFe alloys have also attracted significant interest due to their large saturation flux densities. Some of the challenges with the use of CoFe alloys for single pole heads are discussed in the following

section 1.5.1.

1.5.1 CoFe as a Write Head Material

$\text{Co}_x\text{Fe}_{100-x}$ alloys are currently the best potential candidates for perpendicular recording heads. They possess a high saturation magnetisation, $\mu_0 M_s \geq 2.4$ T in the range $30 \leq x \leq 50$ [35] where x is atomic percent, and thus can write to the high coercivity media required for high density magnetic recording. As deposited CoFe alloys characteristically show isotropic behaviour with relatively large H_c [36]. As mentioned in section 1.5, a large H_c is undesirable for a single pole write head and poses a challenge if CoFe alloys are to be of any use. Previous studies of such films have looked at the effect of various underlayers on the coercive field [36, 37, 38, 39, 40, 41].

Sun and Wang found a reduction in H_c for a FeCoN film with a NiFe underlayer and proposed an exchange induced ripple reduction mechanism in which the incoming FeCoN atoms are exchange coupled to the NiFe during the deposition, thus benefiting from its intrinsic softness and low anisotropy dispersion [37, 38]. Other authors also point out the desirable effect of an underlayer though many with suitable attributes are non-ferromagnetic, emphasising that exchange coupling is not the only means by which H_c can be reduced. For example, Platt et al [36] described a reduction in coercivity from 150 Oe to 12 Oe when CoFe was grown on a thin CoO layer, Jung et al [41] reported significant reductions in H_c for CoFe grown on a range of underlayers including Cu, NiFe and Ru, and Katada et al [40] showed that underlayers of both NiFe and NiFeCr could be effective. All three groups of researchers attributed the lower H_c to a change in film microstructure induced by the underlayer. In particular the importance of reducing the grain size was noted. Moreover, Jung et al [41] pointed out that the reduction in H_c was quantitatively consistent with Hoffman's theory of magnetisation ripple [15, 42].

Magnetisation ripple is the name given to the small wave-like fluctuations of the magnetisation direction that occur in thin ferromagnetic films [15]. Its source is randomly oriented local anisotropies and, in the case of CoFe films, the origin is the anisotropy of the crystallites themselves. The axes of the crystallites are randomly oriented, in either 2- or 3-dimensions, depending on whether the film is textured or not. According to Hoffman's ripple theory, the wall coercivity in a polycrystalline thin film is given by [41]:

$$H_c \propto \frac{S}{M_s} \left(\frac{D}{W} \right)^{1/2} \frac{1}{L} \quad (1.11)$$

Here S is a structure parameter given by $K_{local}D/n^{1/2}$, K_{local} is the local anisotropy, n is the number of grains through the film thickness, D is the mean grain diameter, M_s is the saturation magnetisation, W is the wall width, L is the coupling length parallel to the wall approximated by $(A/K_1)^{1/2}$ where A is the exchange constant and K_1 is the magnetocrystalline anisotropy constant. From the relationship it is evident that a reduction in the mean grain size would indeed cause a reduction in the coercivity. S is also important for determining the dispersion angle of the ripple; a smaller S gives a smaller dispersion and the dependence on n is particularly relevant here as laminated films are under investigation.

Vopsaroiu et al [43] recently investigated the effect of controlling the grain size in CoFe films without seedlayers by a plasma sputtering process. They reported a reduction in H_c from 120 Oe to 12 Oe, a similar result to those described above, and again related the improvement in softness to a decrease in crystallite size. However, rather than using the ripple theory, they argued that the variation of H_c was well described by the random anisotropy model [43]. In this model, for a mean grain size D and exchange length L_{ex} , the coercivity increases as $\sim D^6$ for $D < L_{ex}$, is independent of D for $D \approx L_{ex}$ and decreases with $1/D$ for grain sizes larger than the domain wall width. For the case where

$D < L_{ex}$ the intergranular exchange is significant and sudden changes in the magnetisation at grain boundaries are prevented giving a more uniform magnetisation whereas for $D > L_{ex}$ local changes in anisotropy from grain to grain can affect the magnetisation orientation and more complex magnetisation distributions can occur. The results from Vopsariu et al [43] showed that for grain sizes less than 15 nm the coercivity was less than 25 Oe and for grain sizes in the range 15 nm to 26 nm the coercivity remained almost constant at 120 Oe. Thus whilst discussion continues on the precise mechanism by which H_c is controlled in high moment films of the kind used in write heads, it is generally agreed that grain size is important and that a small mean value is desirable.

Another of the main concerns for films used in a single-pole writer is the requirement for a remanent state which will not cause unwanted erasure of recorded data. Previously it was shown through modelling that laminating the pole tip gives near zero remanent field and therefore reduces this so called erase-after-write (EAW) [44]. Subsequently Nakamoto et al. demonstrated a significant reduction in head induced erasure by laminating high moment CoFe with non-magnetic NiCr [45]. The dynamics of laminated writers is also under investigation as it is desirable to reach the non-erasing state quickly [46].

1.6 Summary

In this chapter the basics of ferromagnetism have been discussed along with the use of ferromagnetic materials in magnetic recording. In section 1.4 various types of recording have been discussed and the promise of the perpendicular mode for high density recording has been shown. Section 1.5.1 focused on the write pole material and discussed the benefits and various challenges of the use of CoFe alloys.

The work in this thesis focuses on the magnetic and physical characterisation of various CoFe thin films through the use of transmission electron

microscopy. To gain a greater understanding of the properties of possible write pole materials the effect on the magnetic microstructure of both seedlayers and spacer layers has been investigated thereby allowing not only single layer but laminated CoFe films to be studied. The instrumentation and experimental techniques are discussed in chapter 2. Chapter 3 introduces the magnetic characterisation of very soft thin films through the Fresnel mode of Lorentz microscopy. The magnetic and physical characterisation of various CoFe multilayers are presented in chapters 4-6 and chapter 7 characterises patterned permalloy films.

Bibliography

- [1] http://www-1.ibm.com/ibm/history/history/decade_1950.html .
- [2] <http://www.eetimes.com/sys/news/OEG20030718S0038> .
- [3] S. H. Charap, P. L. Lu, and Y. He, IEEE Trans. Magn. **33** (1), 978 (1997).
- [4] http://www.theregister.co.uk/2005/08/17/toshiba_perpendicular_hdd .
- [5] <http://www.seagate.com/cda/newsinfo/newsroom/releases/article/0,1121,2934%5E,00.html> .
- [6] <http://www.seagate.com/cda/newsinfo/newsroom/releases/article/0,1121,3160%5E,00.html> .
- [7] P. Weiss, J. Phys. **6**, 661 (1907).
- [8] W. Heisenberg, Z Physik **49**, 619 (1928).
- [9] Y. Martin and H. K. Wickramasinghe, Appl. Phys. Lett. **50** (20), 1455 (1987).
- [10] F. Bitter, Phys. Rev. **41**, 507 (1932).
- [11] H. J. Williams, F. G. Foster, and E. A. Wood, Phys. Rev. **82**, 119 (1951).
- [12] J. N. Chapman, J. Phys. D **17**, 623 (1984).
- [13] V. A. Vas'ko *et al.*, J. Appl. Phys. **91**, 6818 (2002).

-
- [14] H. Hoffman, *IEEE Trans. Magn.* **4** (1), 32 (1968).
- [15] H. Hoffman, *J. Appl. Phys.* **35** (6), 32 (1964).
- [16] A. Hubert and R. Schafer, *Magnetic domains: the analysis of magnetic microstructures* (Springer, 1998).
- [17] J. E. E. Huber, D. O. Smith, and J. R. Goodenough, *J. Appl. Phys.* **29**, 294 (1958).
- [18] J. P. King, J. N. Chapman, M. F. Gilles, and J. C. S. Kools, *J. Phys. D* **34**, 528 (2001).
- [19] P. Gogol, J. N. Chapman, M. F. Gilles, and F. W. M. Vanhelmont, *J. Appl. Phys.* **92**, 1458 (2002).
- [20] J. G. Zhu, *MRS Bull.* **20**, 49 (1995).
- [21] J. Fidler and T. Schrefl, *J. Phys. D: Appl. Phys.* **33**, R135 (2000).
- [22] T. Schrefl, J. Fidler, and M. Zehetmayer, *J. Appl. Phys.* **87** (9), 5517 (2000).
- [23] V. Poulsen, *Method of recording and reproducing sounds or signals* (U. S. Patent: 661-619-1900, 1898).
- [24] M. H. Kryder and W. Y. Lai, *IEEE Trans. Magn.* **30**, 3873 (1994).
- [25] T. Susuki, *IEEE Trans. Magn.* **MAG-20** (5), 675 (1984).
- [26] S. Iwasaki and K. Nakamura, *IEEE Trans. Magn.* **MAG-13** (5), 1272 (1977).
- [27] D. Weller and A. Moser, *IEEE Trans. Magn.* **35**, 4423 (1999).
- [28] D. Litvinov *et al.*, *IEEE Trans. Magn.* **36** (5), 2483 (2000).
- [29] http://www.seagate.com/docs/pdf/whitepaper/TP-549_PerpRecording_Feb-06.pdf .
- [30] S. Khizroev and D. Litvinov, *J. Appl. Phys.* **95**, 4521 (2004).

-
- [31] D. Z. Bai and J. G. Zhu, *IEEE Trans. Magn.* **38** (5), 2240 (2002).
- [32] M. Mochizuki *et al.*, *J. Magn. Magn. Mater.* **235**, 191 (2001).
- [33] M. H. Kryder, S. Wang, and K. Rook, *J. Appl. Phys.* **30**, 6212 (1993).
- [34] M. Komuro, Y. Kozono, M. Hanazono, and Y. Sugita, *J. Appl. Phys.* **67** (9), 5126 (1990).
- [35] R. M. Bozorth, *Ferromagnetism* (IEEE, New York, 1993).
- [36] C. L. Platt, A. E. Berkowitz, D. J. Smith, and M. R. McCartney, *J. Appl. Phys.* **88**, 2058 (2000).
- [37] N. X. Sun and S. X. Wang, *J. Appl. Phys.* **92**, 1477 (2002).
- [38] S. X. Wang, N. X. Sun, M. Yamaguchi, and S. Yabukami, *Nature (London)* **407**, 150 (2000).
- [39] V. A. Vas'ko, J. O. Rantschler, and M. T. Kief, *IEEE Trans. Magn.* **40**, 2335 (2004).
- [40] H. Katada, T. Shimatsu, I. Watanabe, H. Muraoka, and Y. Nakamura, *IEEE Trans. Magn.* **38**, 2225 (2002).
- [41] H. S. Jung, W. D. Doyle, and S. Matsunama, *J. Appl. Phys.* **93**, 6462 (2003).
- [42] H. Hoffman, *IEEE Trans. Magn.* **9**, 17 (1973).
- [43] M. Vopsaroiu *et al.*, *J. Appl. Phys.* **97**, 10N303 (2005).
- [44] D. Z. Bai and J. G. Zhu, *J. Appl. Phys.* **93**, 6540 (2003).
- [45] K. Nakamoto *et al.*, *IEEE Trans. Magn.* **40**, 290 (2004).
- [46] O. Heinonen, A. Nazarov, and M. L. Plumer, *J. Appl. Phys.* **99**, 08S302 (2006).

Chapter 2

Instrumentation and Experimental Techniques

2.1 Introduction

This chapter outlines the various experimental techniques used. The sputter deposition of the magnetic films investigated is detailed in section 2.2. An overview of the electron microscope and the basic imaging modes are presented in section 2.3 followed by a discussion of Lorentz microscopy and the implementation of the techniques in the Philips CM20 microscope in section 2.4. Sections 2.5 and 2.6 detail the analytical techniques used to determine the physical microstructure of the films. A brief description of a scanning electron microscope and focused ion beam is given in section 2.7. The preparation of cross-sectional specimens for the analytical investigations and the fabrication of elements by electron beam lithography are then detailed in sections 2.8 and 2.9 respectively.

2.2 Sample Preparation and Characterisation of Films

2.2.1 Deposition of Thin Magnetic Films

One of the most commonly used methods for deposition of thin polycrystalline films is magnetron sputtering. Figure 2.1 shows a schematic of the sputtering process. The deposition chamber is a diode plasma system which is maintained under vacuum. The cathode is formed by the material to be deposited, i.e. the target, and the substrate is placed onto the anode. The plasma is generated by electrons from the cathode ionising an inert gas, usually argon. The gas ions are then accelerated towards the surface of the cathode and atoms from the target are ejected. These atoms are then deposited on the substrate and other surfaces within the chamber forming thin films. Gas pressure and power are important factors in determining the quality of the sputtered film as they control the substrate temperature and sputter rate. For increased sputter rates a magnetron is placed at the target trapping electrons above the target thus increasing the collision rate with the gas atoms. The deposition rate is also influenced by the distance of the substrate from the target. Most systems used today have multiple targets which can be selected without breaking the vacuum, therefore, multilayer films with high interfacial quality can be produced. The thin magnetic films investigated in this thesis were deposited in a multitarget magnetron system by Seagate Technology, Ireland. The composition of the magnetic layers in all films was $\text{Co}_{35}\text{Fe}_{65}$ (written hereafter as CoFe). Only in one case was the film a single magnetic layer; in the other films one or more seed and/or spacer layers were also present. Seed layers were 1nm thick $\text{Ni}_{82.5}\text{Fe}_{17.5}$ (written hereafter as NiFe) and spacer layers were 1.5nm thick Al_2O_3 . The CoFe and NiFe were deposited by DC magnetron sputtering whereas the Al_2O_3 layers were deposited by RF sputtering. The RF mode prevents charge build up on insulating targets by varying the bias applied

across the anode to cathode at a high rate, thus this mode is used for the deposition of oxide films. For the Lorentz microscopy studies the films were deposited on Si_3N_4 membranes supported by Si with a $100\ \mu\text{m} \times 100\ \mu\text{m}$ electron transparent window [1]. Such membranes are suitable for direct use in the transmission electron microscope (TEM), avoiding as they do the need to remove the film from a bulk substrate. The films were also deposited onto Si substrates for the preparation of cross-sectional specimens as detailed in section 2.8.

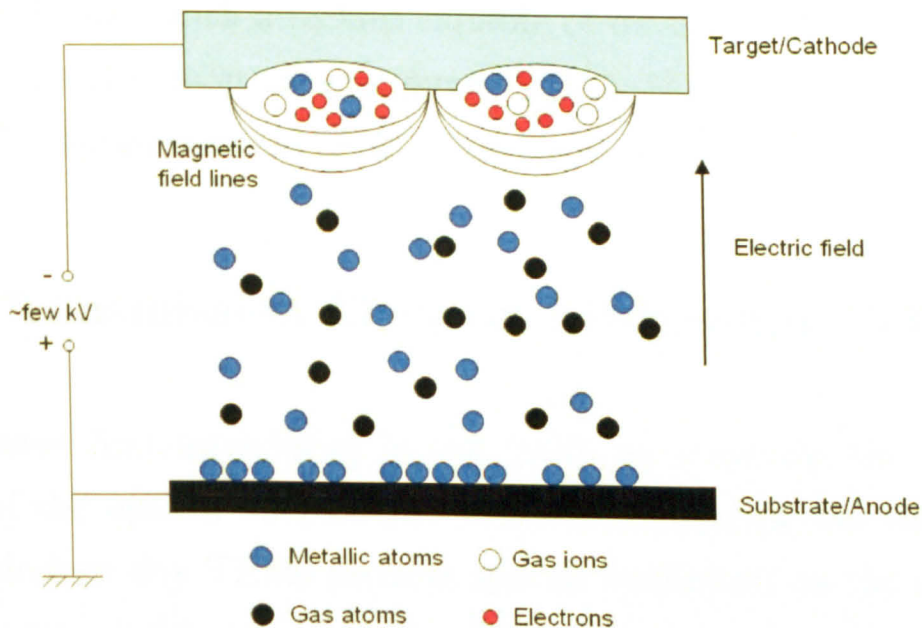


Figure 2.1: Schematic illustration of sputter deposition.

2.2.2 Bulk Characterisation with the B-H looper

The B-H looper provides a non-destructive way to characterise the magnetic properties of whole 6" wafers. The looper described here is the SHB109 model which was used to characterise the films deposited by Seagate Technology, Ireland. There are two main parts which make up the looper: one applies the magnetic field to the wafer and the other monitors the magnetisation of the wafer in the magnetic field.

In the first part orthogonal fields are generated in the plane of the specimen with two pairs of Helmholtz coils. Combination of these orthogonal fields can generate a magnetic field along any in-plane direction.

The second part comprises of two highly sensitive pickup coils: a normal pickup coil and a transverse pickup coil. The normal pickup coil is more sensitive, thus measurements are usually taken with this coil and the wafer is rotated through 90° between measurements of easy and hard axis hysteresis loops.

The SHB109 looper has two coil assemblies: a large coil assembly which has a maximum output field of 75 Oe and a small coil assembly which can output fields up to 200 Oe plus a DC offset of 20 Oe. The large assembly is used with a pickup capable of measuring 6" wafers and was used for the B-H loop measurements in this thesis. The small assembly is used for measurements on 3" silicon samples.

2.3 Transmission Electron Microscopy (TEM)

TEMs were first introduced in the 1930s to overcome the image resolution of the optical microscope, which is limited by the wavelength of light. Modern day TEMs provide spatial resolution on the atomic level and are extremely versatile instruments for characterising a wide range of materials. Along with structural information the TEM provides information on the magnetic microstructure of materials through a technique known as Lorentz microscopy which is discussed in section 2.3.5.

Three microscopes have been used for the work presented in this thesis. For the magnetic work a modified Philips CM20 microscope was used and for the conventional TEM imaging a FEI Tecnai 20 was used. The analytical work was carried out on a FEI Tecnai F20 (S)TEM equipped with a Gatan Enfina spectrometer with spatial resolution of ~ 0.2 nm. The main components of the conventional TEM are discussed in the following two sections.

2.3.1 The Electron Gun

There are three types of electron source used in TEMs: thermionic, cold field emission and Schottky field emission. Electrons are emitted from a thermionic source when it is heated to overcome the workfunction of the material, whereas a field emission source requires the application of an electric field to overcome the workfunction and emit electrons. Either tungsten filaments or lanthanum hexaboride (LaB_6) crystals are used as thermionic emitters due to their high melting point and low work function and field emitters are fine tungsten needles.

The FEI Tecnai 20 microscope utilises a LaB_6 thermionic emitter. In this case the source is bonded to a metal filament which is resistively heated, thus indirectly heating the LaB_6 crystal until thermionic emission occurs at 1700 K. The emitted electrons are then accelerated by a series of electrodes to gain a kinetic energy of 200 keV. A Wehnelt cylinder, positioned between the source and the accelerator stack, controls the emission and focuses the electrons to a cross-over.

The source in a cold field emission gun (FEG) is biased negatively with respect to two anodes. Intense electric fields are generated at the tip by application of a positive potential to the first anode. This potential is known as the extraction voltage as the fields generated enable electrons to quantum mechanically tunnel out of the tip. The second anode accelerates the electrons to their operating voltage and a cross-over is formed by combination of the fields from both anodes. For field emission to occur the tip must be in pristine condition, but even under UHV conditions build up of contaminants still occurs. Thermally assisted FEGs overcome this by moderately heating the tip to evaporate the contaminants. This also has the benefit of assisting the electrons in overcoming the energy barrier.

In a Schottky field emission gun the tip is coated with another material, e.g. zirconia (ZrO_2), which acts to reduce the work function. The

application of an electric field then gives the electrons enough energy to overcome the workfunction and escape from the tip. Both the Philips CM20 and the FEI Tecnai F20 have Schottky field emission sources and have operating voltages of 200 keV.

In both the thermionic and field emission cases a virtual electron source is created from the first cross-over formed from the electron gun. The characteristics of this virtual source dictate the brightness, β , of the gun which is given by:

$$\beta = \frac{4i_e}{(\pi d_0 \alpha_0)^2} \quad (2.1)$$

where i_e is the emission current, d_0 the virtual source diameter and α_0 the convergence half angle. The virtual source size in the FEG is $\sim 100x$ smaller than in the LaB₆ thermionic gun. This results in a far greater brightness in the FEG (of the order of 10^{13} A/m²sr compared to 10^{10} A/m²sr in the LaB₆ gun). FEGs also have a smaller energy spread than thermionic sources making them more suitable for applications such as HRTEM and Lorentz microscopy which require a small coherent source. Thermionic sources are more suitable for standard TEM as the greater source size allows larger areas of the specimen to be illuminated without the loss of intensity on the screen.

2.3.2 The Microscope Column

Electrons leaving the gun region pass into the microscope column. A schematic illustration of a conventional TEM column is shown in figure 2.2. The illumination system consists of a range of lenses and apertures which determine how the specimen is illuminated and the mode of operation of the microscope.

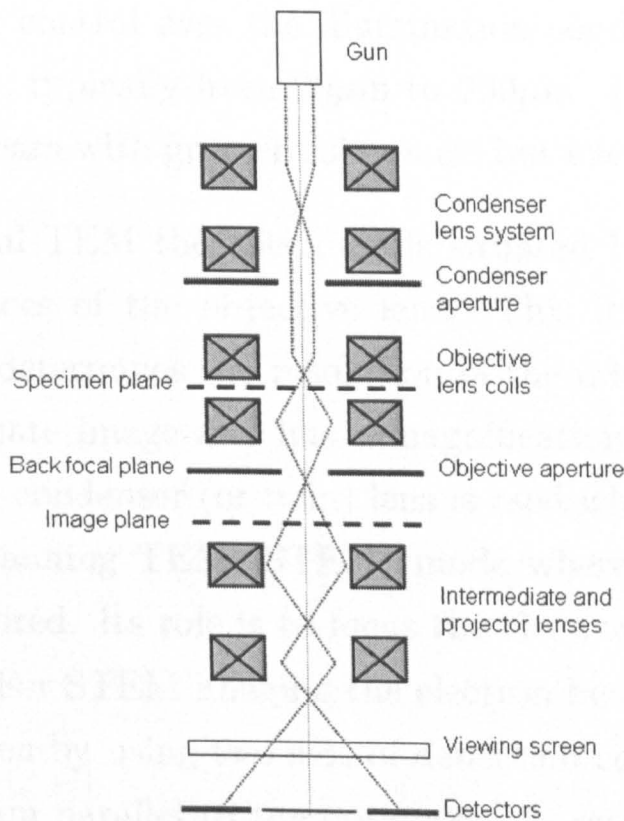


Figure 2.2: Simplified ray diagram for image formation in conventional TEM.

TEMs use magnetic lenses to focus and magnify the electron beam. These consist of a polepiece made up of a soft magnetic material with a hole (or bore) drilled through it, copper coils which surround the polepiece and a lens body. There are usually two polepieces in one lens and the distance between them is called the gap. The bore to gap ratio controls the focussing action of the lens. A magnetic field is generated in the bore when a current is passed through the coils and the lens body provides a path for the magnetic field to flow through completing the magnetic circuit. The user can control the strength of the field and subsequently, through the Lorentz force, the path of the electrons by changing the current through the coils.

In all three microscopes used for the work in this thesis there are two main condenser lenses, C_1 and C_2 . The C_1 lens forms a demagnified image of the gun cross-over and controls the beam diameter at the specimen. The angular convergence of the beam is controlled by the C_2 lens. The condenser aperture strip lies below the condenser lens system and

this allows further control over the illumination conditions. The apertures range in size, typically from $20\mu\text{m}$ to $200\mu\text{m}$. Inserting a smaller aperture gives a beam with greater coherence, but lower current density.

In the conventional TEM the specimen is situated between the upper and lower polepieces of the objective lens. This lens is the primary imaging lens and determines the resolution of the microscope. It forms the first intermediate image and has a magnification in the range 50 - 100 times. A mini-condenser (or twin) lens is used when the microscope is operating in scanning TEM (STEM) mode where a probe size less than 10 nm is desired. Its role is to focus the electron beam to a probe at the specimen. For STEM imaging the electron beam is then rastered across the specimen by using two sets of deflection coils which keep the motion of the beam parallel to the optic axis. A series of intermediate and projector lenses further magnify the image and project it onto the phosphor viewing screen. The first intermediate lens is responsible for selecting whether the microscope operates in an imaging or diffraction mode.

In most modern microscopes images are recorded with a charge coupled device (CCD) camera situated below the viewing screen. A scintillator plate converts the electron image into a light image which is then transferred to the surface of the pixelated CCD through a fibre optic plate. To control the exposure and prevent burning of the CCD array the electron beam is blanked and unblanked for a specified time. The image data is read out directly by computer allowing real time viewing and processing of the data. It is still possible to acquire images with film, however, the CCD camera is a far quicker way of recording images. Diffraction patterns still tend to be recorded with film to prevent burning the CCD array.

2.3.3 Diffraction

Electrons incident on a crystalline specimen are diffracted from crystallographic planes through Bragg scattering. These diffracted electrons form a diffraction pattern close to the back focal plane of the objective lens. By adjusting the post-specimen lens set up so that the back focal plane of the objective lens acts as the object plane for the first intermediate lens the diffraction pattern can be viewed on the phosphor screen (fig. 2.3(a)).

2.3.4 Bright Field and Dark Field Imaging

The simplest modes of operation in a TEM are bright field and dark field imaging. In both modes the intermediate lens is adjusted so that its object plane is the image plane of the objective lens. For the bright field mode the image is formed by electrons from the central diffraction spot, i.e. the direct electrons (figure 2.3b), whereas in the dark field mode the scattered electrons form the image (figure 2.3c). An aperture is inserted into the back focal plane to select the electrons to form the image. The contrast formed in the bright field image is from variations in electron scattering across the specimen. The dark field mode can be performed in two ways: either the aperture can be displaced from the optic axis to a specific diffracted beam or the illumination can be tilted so that the diffracted beam remains on axis. When the aperture is displaced the selected electrons are off-axis and are subject to aberrations and it can be difficult to focus the image. Hence, for the dark field imaging carried out in this thesis, the electron beam has been tilted so that the diffracted electrons travel down the optic axis and the aberrations are avoided. The image formed in this mode is predominantly dark with bright areas indicating crystallites whose orientation is appropriate for excitation of the selected diffracted beam.

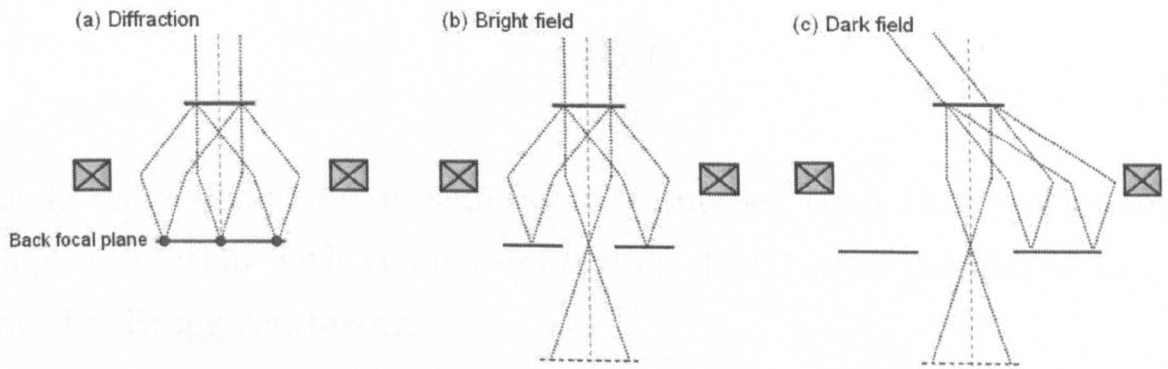


Figure 2.3: Schematic of (a) diffraction, (b) bright field and (c) dark field imaging modes.

2.3.5 Magnetic Imaging

In Lorentz microscopy [2] image contrast is generated from the deflection of the electrons as they pass through a magnetic specimen. The deflection is a consequence of the classical Lorentz force, \mathbf{F}_L , which is given by:

$$\mathbf{F}_L = -e(\mathbf{v} \times \mathbf{B}) \quad (2.2)$$

where e is the electron charge, \mathbf{v} the velocity of the electrons and \mathbf{B} the magnetic induction (of the specimen). For electrons incident perpendicular to the specimen the deflection angle, β_L , is proportional to the integrated induction along the path of the electrons. The deflection angle in the x direction due to the y component of induction, B_y , is expressed as:

$$\beta_L(x) = \frac{e\lambda}{h} \int_{-\infty}^{\infty} B_y(x, z) dz \quad (2.3)$$

where x and y are the directions in the plane of the specimen, λ is the de Broglie wavelength and h is Planck's constant. For a uniform film of thickness t with uniform in-plane magnetisation and saturation magnetic induction B_s , the deflection angle β_L is given by

$$\beta_L = \frac{e\mathbf{B}_s t \lambda}{h} \quad (2.4)$$

The Lorentz deflection is significantly smaller than that arising from Bragg diffraction with typical deflections 1-100 μrad compared to ~ 10 mrad for Bragg scattering.

Lorentz microscopy can also be considered from a quantum wave-optical approach and this is necessary to extract the maximum quantitative information. From this approach the deflection of the electrons is replaced by a phase shift, ϕ , experienced by the electron waves when passing through the specimen [3].

$$\phi = \frac{2\pi e N}{h} \quad (2.5)$$

where N is the magnetic flux enclosed by the paths of two electron rays. The phase shift between two points, x_1 and x_2 can then be described by:

$$\phi(x_2 - x_1) = \frac{2\pi e}{h} \int_{x_1}^{x_2} \int_{-\infty}^{\infty} B_y(x, z) dz dx \quad (2.6)$$

which can be written as:

$$\phi(x_2 - x_1) = \frac{2\pi e t}{h} \int_{x_1}^{x_2} B_y(x) dx \quad (2.7)$$

Hence, it can be seen that the magnitude of the phase shift is proportional to the integrated magnetic induction along the electron trajectory.

2.4 The Philips CM20

The Philips CM20 microscope has a column specifically modified for Lorentz microscopy investigations [4]. The principal modifications to the

column are the introduction of two super mini-lenses above and below the objective polepieces and an increased gap (figure 2.4). The objective lens is switched off to avoid significantly altering the magnetic fields around and within the specimen. The mini-lenses act as the condenser and imaging lenses allowing the specimen to be in field-free space and the magnetic microstructure to be observed. The objective lens can, however, be excited weakly to act as a source of magnetic field perpendicular to the plane of the specimen. A component of field can then be introduced in the plane of the specimen through tilting the specimen in its holder; thereby in-situ magnetising experiments can be performed [5]. For the films investigated here vertical fields of typically 100 - 300 Oe were used, although the maximum field available is ~ 6300 Oe.

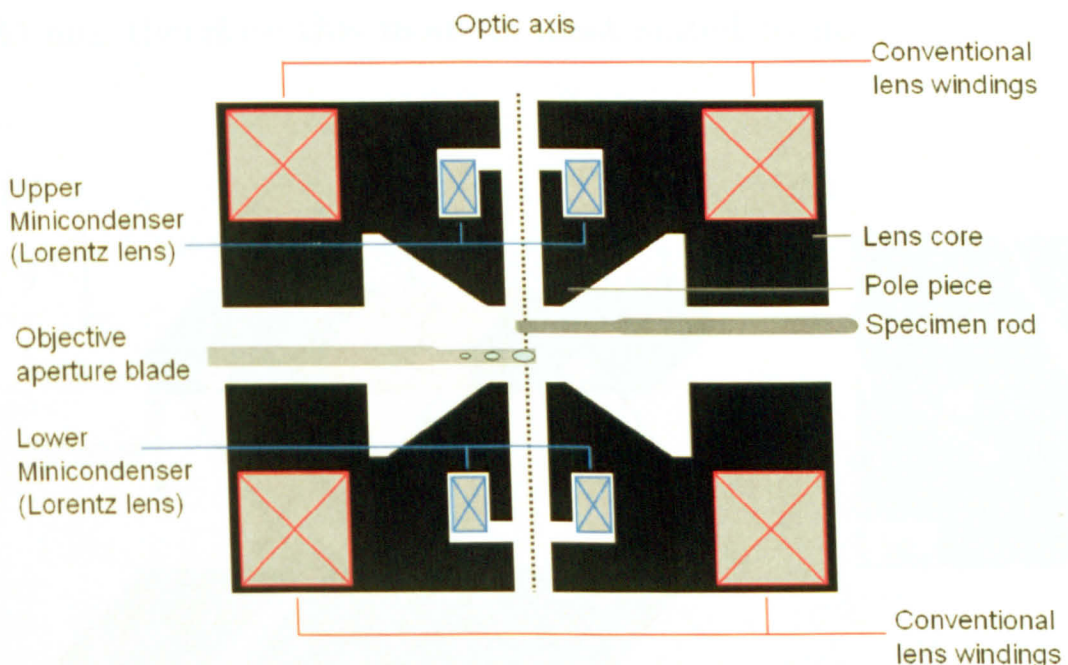


Figure 2.4: Modified objective lens region in the Philips CM20 microscope.

2.4.1 Fresnel Imaging

The Fresnel mode of Lorentz microscopy is one of the most commonly used techniques for imaging magnetic microstructure and is easy to implement in the TEM. By over or underfocusing of the imaging lenses the intensity distribution of electrons at a distance Δz above or below the specimen can be imaged [6]. Domain walls are revealed as narrow bright

and dark bands on a near uniform background as illustrated in figure 2.5. The magnetic contrast can be inverted by changing from overfocus to underfocus. In polycrystalline specimens magnetisation ripple is often seen within the domains themselves [7]. The ripple arises from the variations in anisotropy, a consequence of the different orientations of the individual crystallites. The ripple direction is known to be perpendicular to the mean direction of magnetisation [8] and thus can be used to orient the specimen in the microscope such that the applied field is parallel to either the easy or hard axis of the film.

The Fresnel mode is a relatively quick and simple method of obtaining good qualitative magnetic images. The main disadvantage of the technique is the limited resolution due to defocusing the imaging lens, at best 30 nm; therefore this mode is most suited to imaging continuous films.

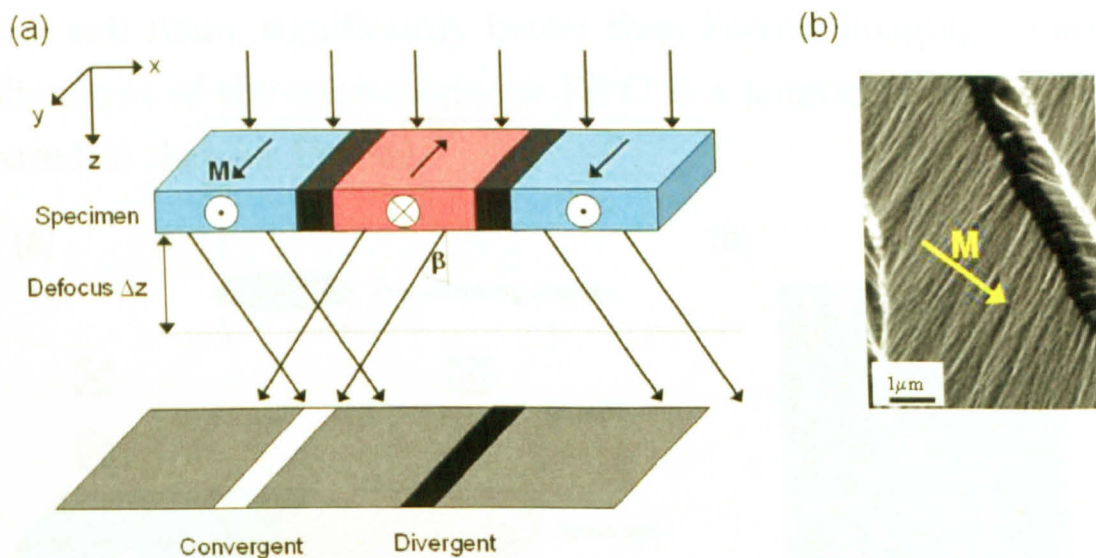


Figure 2.5: (a) Schematic ray diagram for image formation in the Fresnel imaging mode and (b) Example Fresnel image. The yellow arrow indicates the magnetisation direction.

2.4.2 Differential Phase Contrast (DPC)

The differential phase contrast (DPC) [9] mode is a technique which enables determination of the local direction and magnitude of the in-plane component of magnetic induction and, as such, is more suitable

for quantitative studies. It is a STEM technique in which the electron beam is focused to a small probe and rastered across the specimen by a set of scan coils. The electrons are deflected by the Lorentz force as they pass through the specimen and form a cone which is then descanned by a second set of coils and projected onto a quadrant detector as illustrated in figure 2.6. Due to the Lorentz deflections the projected cone is not centred on the detector giving different signal levels from each of the quadrants. Taking difference signals from opposite quadrants gives a direct measure of orthogonal components of β_L , therefore the components of magnetic induction can be found and a complete map of the in-plane induction from an untilted specimen can be built up. Summing the signals from all four quadrants gives a bright field image of the specimen, thus structural and magnetic information can be compared directly. The resolution of DPC imaging is dependent on the probe size which is determined from the pre-specimen optics. In the Philips CM20 the resolution is sub 10nm, significantly better than Fresnel imaging. However, the alignment of the microscope for DPC is a lengthy procedure when compared to that for Fresnel.

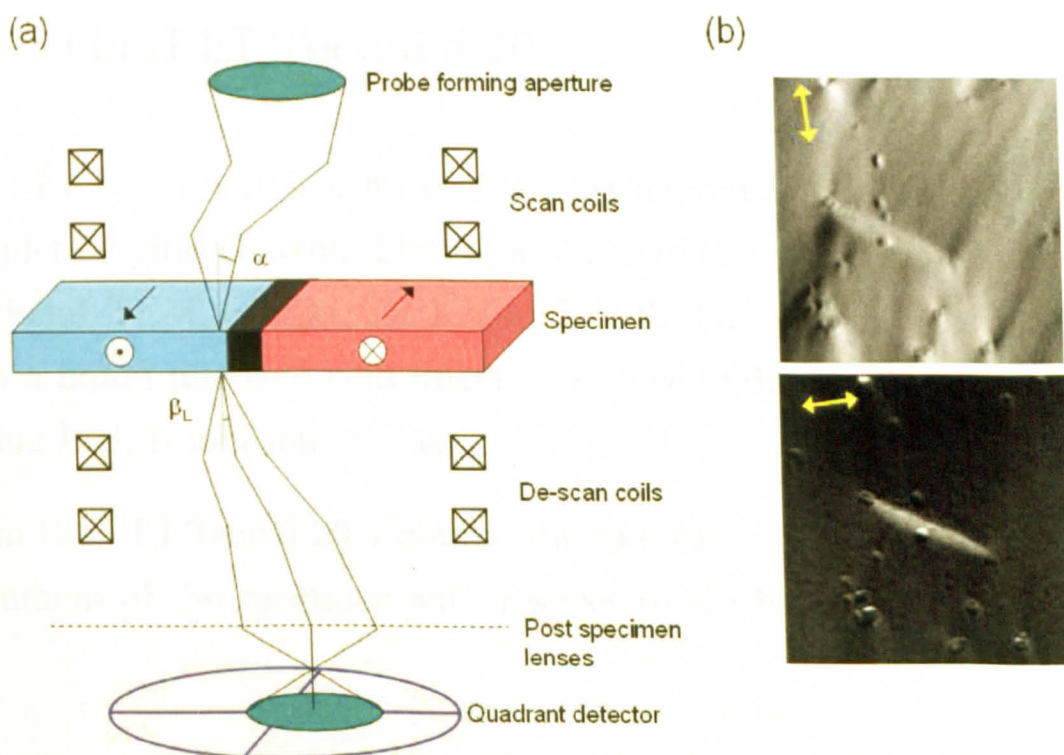


Figure 2.6: (a) Schematic of image formation in DPC and (b) Example DPC images. The yellow arrows indicate the direction of induction which the corresponding image is sensitive to.

2.5 The FEI Tecnai 20

For the work in this thesis the FEI Tecnai 20 was primarily used for conventional TEM. It is also capable of Fresnel imaging, although the magnetic imaging in this thesis was mainly carried out in the Philips CM20.

For the cross-sectional multilayer samples under investigation a double tilt rod was used to ensure the sample was aligned such that the incident electron beam was parallel to the layer interfaces. The rod enabled tilts of $\pm 40^\circ$ in the α -direction and $\pm 30^\circ$ in the β -direction as illustrated in figure 2.7.

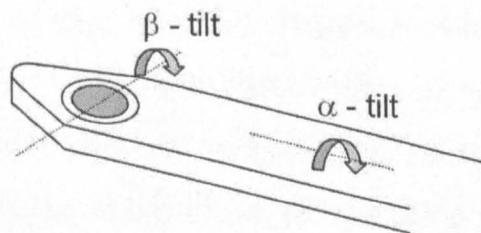


Figure 2.7: Schematic illustration of the Tecnai double tilt rod.

2.6 The FEI Tecnai F20

The FEI Tecnai F20 is a state-of-the-art nanoanalytical microscope with complete digital control. The capabilities of the microscope include conventional TEM, STEM, EDX and EELS. The column has been fitted with a liquid nitrogen cold finger to reduce hydrocarbon contamination during high resolution studies.

As in the FEI Tecnai 20 a double tilt rod was used to ensure the correct alignment of the specimen with respect to the incident electron beam.

2.6.1 STEM Bright and dark field Imaging

In the STEM mode electron detectors are used to form the images. These act in a similar way to the apertures in CTEM allowing only specific electrons to contribute to the image formation. For bright field images the detector is centred on the optic axis allowing the direct beam to form the image, thus bright field imaging in STEM produces similar images to standard TEM bright field images. This is true provided the reciprocity theorem holds, i.e. if the range of angular integration in the STEM detector plane is the same as the beam convergence angle in CTEM. For dark field STEM, annular detectors which surround the bright field detector are used to collect scattered electrons, hence images are formed from a large fraction of the annular range of electrons unlike in TEM where only one specific reflection forms the image. In the FEI Tecnai F20 there are two dark field detectors; an annular dark field (ADF) and a high angle annular dark field (HAADF) as illustrated in figure 2.8. The ADF detector is mainly used for dark field STEM imaging. The HAADF detector only collects those electrons which are scattered through large angles, $\theta > 50$ mrad [10], therefore the contrast observed in the images is dependent on the atomic number. Hence this technique is often referred to as Z-contrast imaging.

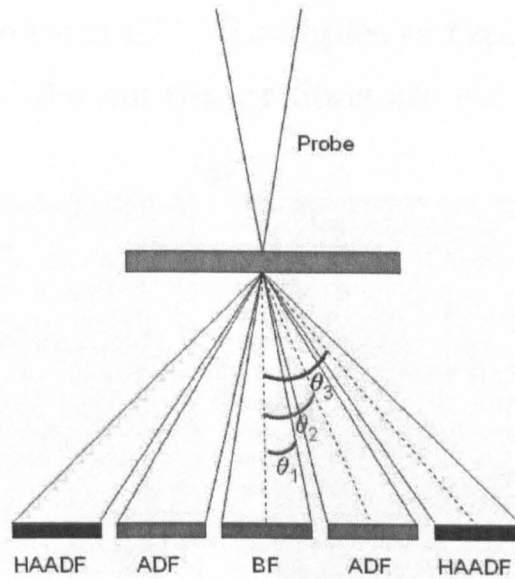


Figure 2.8: Schematic illustration of STEM detectors on the Tecnai F20 where the collection angles follow the following relationship $\theta_3 > \theta_2 > \theta_1$. The BF detector collects the direct electron beam and low angle scattered electrons whereas the ADF and HAADF detectors collect those electron scattered to higher angles.

2.6.2 Electron Energy Loss Spectroscopy (EELS)

In electron energy loss spectroscopy a monoenergetic electron beam is fired at a thin specimen (the beam energy in the FEI Tecnai F20 is 200keV). The incident electrons can be inelastically scattered from the atoms through excitation of inner shell electrons to unoccupied states [11]. This process results in an ionisation edge in the energy loss spectrum at an energy equal to the binding energy of the shell, thus the edges are characteristic of the material being investigated. An energy loss spectrum is obtained by measuring the energy distribution of the transmitted electron beam and information on local chemistry and bonding can be extracted from the resulting spectrum.

In the EELS spectrum there are two areas of interest: the low loss region and the core loss region. The low loss spectrum contains the zero loss peak which results from electrons having lost no energy and the plasmon peak where the electrons have lost energy from plasmon excitations which are resonant oscillations of the valence electrons in a solid. The core loss region contains the characteristic ionisation edges superimposed

on a background of the form E^{-r} . Examples of typical low loss and core loss spectra from the CoFe multilayer films are shown in figure 2.9.

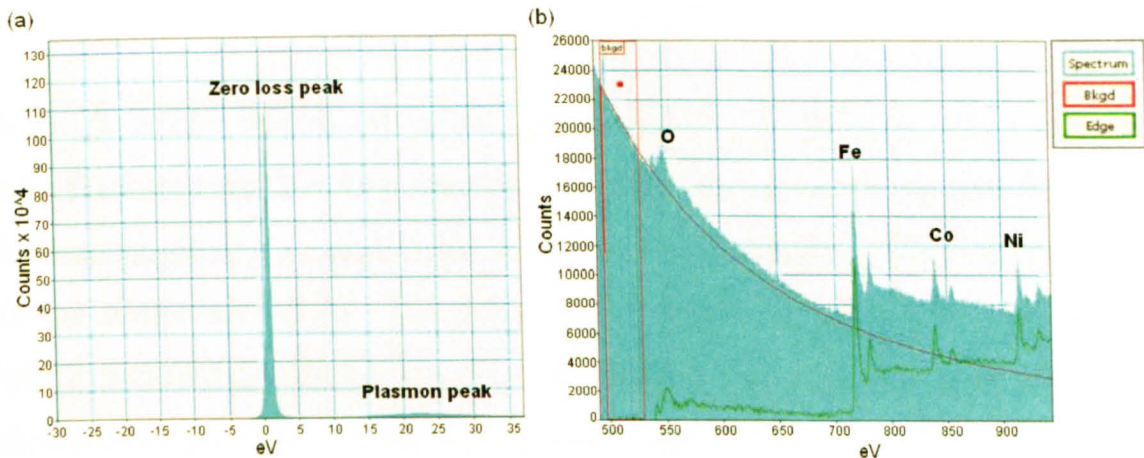


Figure 2.9: Example of an EELS spectra from the CoFe multilayer samples showing (a) the low loss region and (b) the core loss region.

For EELS investigations the sample thickness is extremely important and is limited to ~ 100 nm as the peak to background ratio rapidly decreases with thickness. However, if the specimen is too thin there is very little scattering and the signal to noise ratio is low. The probability of multiple scattering increases as the thickness of the specimen increases. The probability of a scattering event should obey Poisson statistics where the probability of an electron undergoing n scattering events is given by [11]:

$$P_n = \left(\frac{1}{n!}\right) \left(\frac{t}{\lambda_T}\right)^n \exp\left(-\frac{t}{\lambda_T}\right) \quad (2.8)$$

where t is the specimen thickness and λ_T is the total mean free path. Thus the specimen thickness can be found from the intensity relationship:

$$I_0 = I_t \exp\left(-\frac{t}{\lambda_T}\right) \quad (2.9)$$

where I_0 is the intensity of the zero loss peak and I_t is the transmitted intensity. It is also possible to extract quantitative information from the

peak intensities through the following relationship:

$$I_k(\Delta, \alpha, \beta) = N\sigma_k(\Delta, \alpha, \beta) I_0 \quad (2.10)$$

where Δ is the width of an energy window, I_k and σ_k are the intensity and cross-section for the energy window Δ . I_k and σ_k are functions of the convergence, α , and collection, β , semi angles. The energy window can be constrained by the presence of multiple edges in the spectrum. This relationship allows atomic ratios for two elements, a and b , to be calculated through the following equation:

$$\frac{N_a}{N_b} = \frac{I_{ka}(\Delta_a, \alpha, \beta) \sigma_{ka}(\Delta_a, \alpha, \beta)}{I_{kb}(\Delta_b, \alpha, \beta) \sigma_{kb}(\Delta_b, \alpha, \beta)} \quad (2.11)$$

For the work on the CoFe multilayers in this thesis this is useful in determining if the relative composition of the elements varies throughout the film.

2.6.3 The EELS spectrometer

The Tecnai F20 is fitted with a Gatan EnfinaTM parallel detection electron energy loss spectrometer. A schematic illustration of the spectrometer is shown in figure 2.10. Electrons entering the spectrometer are focused by the quadrupole and sextupole lenses. They are then separated out according to their energies by the magnetic prism and an energy spectrum is formed. The quadrupole lenses increase the dispersion of the spectrum before detection with a yttrium aluminium garnet (YAG) scintillator coupled to a 1340×100 CCD camera. The dispersion can be set to a range of values from 0.05 eV to 1.0 eV per channel. Typical values used for the EELS work on the CoFe multilayers were 0.3 eV and 0.5 eV per channel, these settings ensured simultaneous detection of all the elemental edges being investigated. Applying a voltage to the elec-

tronically isolated drift tube enables an energy off-set of the spectrum allowing correction of energy drift.

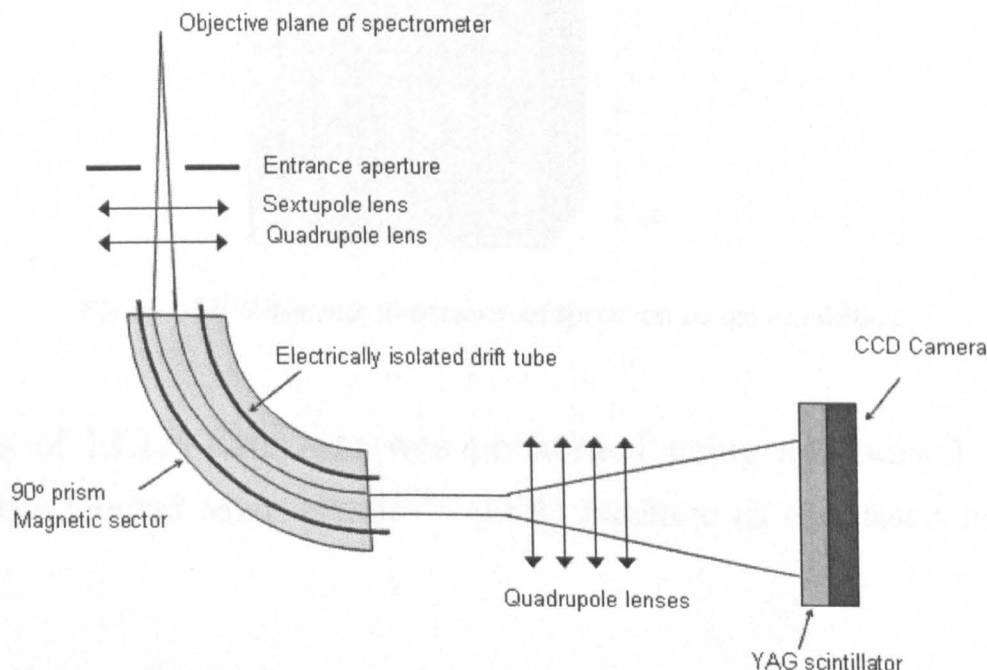


Figure 2.10: Schematic illustration of the main parts of the Gatan Enfina spectrometer.

2.6.4 Spectrum Imaging

It is possible to observe changes in local composition across interfaces and grain boundaries through spectrum imaging. This is a scanning technique which involves collecting spectra at points across a line or area and produces a digital image in which every pixel corresponds to an EELS spectrum. The data can be processed from the whole spectrum image simultaneously allowing consistent analyses, such as elemental profiles across the specimen, to be produced. A schematic illustration of the 3D nature of spectrum images is shown in figure 2.11. Spectrum imaging can be quite time consuming as it is a point by point technique. Therefore, although it is possible to record spectra over an area it is usual to record 2D line traces in which the dimensions are Δx and ΔE .

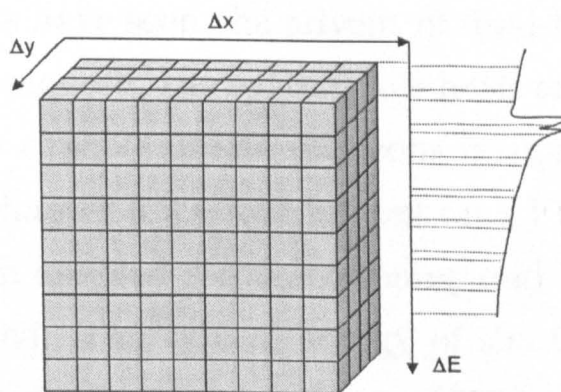


Figure 2.11: Schematic illustration of spectrum image acquisition.

Analysis of EELS data sets was performed using specialised software within the Digital MicrographTM (DM) package as discussed in section 6.4.

2.7 The Scanning Electron Microscope and Focused Ion Beam System

A scanning electron microscope is capable of imaging the surface of materials. In this system an electron beam is focused by a series of apertures and lenses and rastered across the specimen. Collection of the secondary electrons, which are emitted as the electron beam interacts with the specimen, enables an image of the specimen surface to be formed and topographic information can be determined.

The focused ion beam (FIB) system is similar to the SEM in that it rasters a beam across the specimen and an image can be formed from the secondary electrons. Ions are field extracted from a liquid metal ion source, commonly Ga^+ , and accelerated by an electric field. The ions are then collimated and focused with a series of apertures and electrostatic lenses. FIBs are most commonly used for milling materials, performing tasks such as trimming of write heads for perpendicular recording [12] and preparation of TEM specimens [13].

Recent developments have seen the advent of dual-beam SEM/FIB systems. As the name suggests the system has both an electron beam and an ion beam thus is capable of simultaneous imaging and milling. The SEM/FIB work in chapter 6 was carried out on a FEI xT Nova Nanolab 200 SEM/FIB which enabled serial sectioning and imaging of the CoFe films to be performed. The typical energy of the Ga^+ beam is 30 keV with beam currents ranging from 1 pA to 20000 pA. The best quoted resolution of the Ga^+ beam is 6 nm [14]. The electron beam is a FEG-SEM column with an energy range of 500 eV to 30 keV. The instrument also has the capability to deposit Pt by gas ion injection. This is useful in protecting specific areas of the specimen before milling is performed.

2.8 Preparation of Cross-sectional Specimens

In order to look at materials in a TEM they must be electron transparent, i.e. a maximum thickness of ~ 100 nm for 200 keV electrons. For the high resolution studies of the magnetic films cross-sectional specimens need to be thinned down to see what is happening through the multilayer stack. An established encapsulation method which involves dimpling followed by ion-milling to electron transparency was used here [15]. Electron transparent regions are typically a few hundred nm. A schematic of a cross-sectional specimen before and after ion beam thinning is shown in figure 2.12.

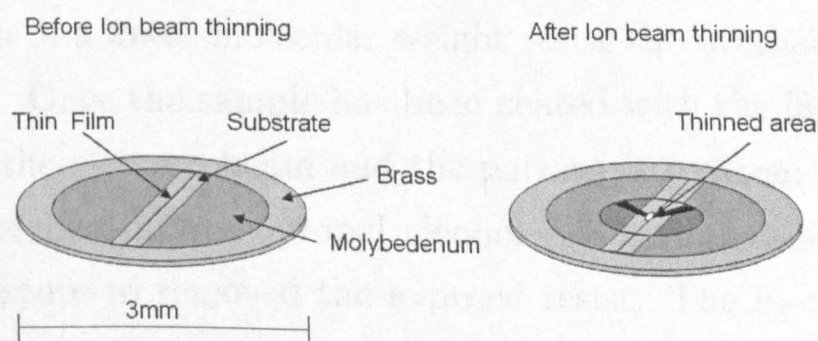


Figure 2.12: Schematic illustration of a cross-sectional specimen.

2.9 Electron Beam Lithography and the Lift-off Process

Although useful information is obtained from the characterisation of continuous films, characterising elements with similar dimensions to those of a recording head provides a better indication of the behaviour of the heads. For this reason patterned films were prepared by electron beam lithography. This is a well established technique for defining very small structures and a technique has been developed for the fabrication of elements on Si_3N_4 membranes for viewing in the transmission electron microscope [1]. The electron beam is focused to a spot by a series of magnetic lenses and scanned across the sample surface by deflecting the beam and moving the sample stage under computer control. The pattern to be written is designed with computer software then transferred to the beam writer.

The basic steps involved in the lift-off process used to fabricate the patterned structures are illustrated in figure 2.13. The sample is coated with a material which is responsive to the electron beam known as a resist. Polymethyl methacrylate (PMMA) is one of the highest resolution resists [16] and was used here. In order for the deposited material to have a clean separation from the resist an overhang profile is desired. This is achieved by depositing two separated layers of resist with different molecular weights. A higher molecular weight resist produces smaller line widths for a give dose, thus by coating a higher molecular weight resist on top of a lower molecular weight resist the overhang profile can be achieved. Once the sample has been coated with the layer resist it is exposed to the electron beam and the pattern is written. The material is then developed in an isopropyl alcohol (IPA):methyl-isobutyl ketone (MiBK) mixture to removed the exposed resist. The metal is then deposited (a process known as metallisation) and the resist removed with acetone. The metal which was on the resist is lifted-off and the desired

pattern is left on the sample.

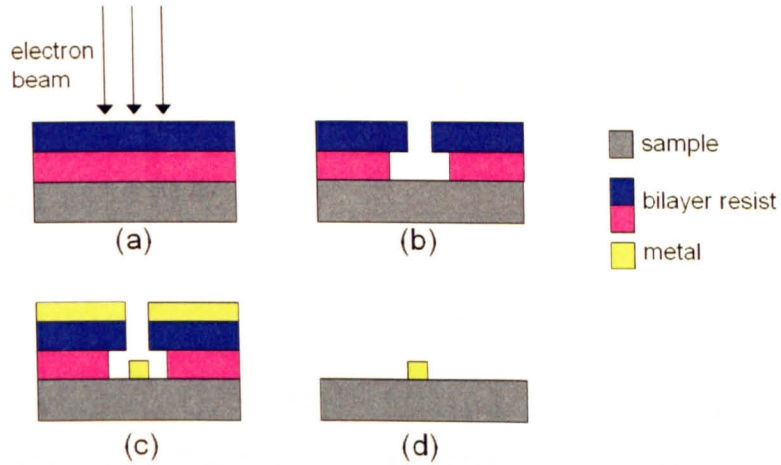


Figure 2.13: Schematic of the steps involved in the lift-off process. (a) the two layers of resist on top of the sample, (b) the overhang profile created after e-beam exposure and developing, (c) metallisation and (d) after lift-off.

Bibliography

- [1] B. Khamsehpour, C. D. Wilkinson, J. N. Chapman, and A. B. Johnston, *J. Vac. Sci. Technol. B* **14** (5), 3361 (1996).
- [2] J. N. Chapman, *J. Phys. D* **17**, 623 (1984).
- [3] Y. Aharonov and D. Bohm, *Phys. Rev. B* **115**, 485 (1959).
- [4] J. N. Chapman *et al.*, *IEEE Trans. Magn.* **30**, 4479 (1994).
- [5] S. McVitie, J. N. Chapman, L. Zhou, L. J. Heyderman, and W. A. P. Nicholson, *J. Magn. Magn. Mater.* **148**, 232 (1995).
- [6] J. N. Chapman, P. E. Batson, E. M. Waddell, and R. P. Ferrier, *Ultramicroscopy* **3**, 203 (1978).
- [7] H. Hoffman, *IEEE Trans. Magn.* **4** (1), 32 (1968).
- [8] M. F. Gilles, J. N. Chapman, and J. C. S. Kools, *J. Appl. Phys.* **78**, 5554 (1995).
- [9] J. N. Chapman, P. R. Aitchison, K. J. Kirk, and S. McVitie, *J Appl. Phys.* **83**, 5321 (1998).
- [10] D. B. Williams and C. B. Carter, *Transmission Electron Microscopy* (Kluwer Academic).
- [11] R. F. Egerton, *Electron Energy-Loss Spectroscopy in the Electorn Microscope* (Plenum Press, New York, 1985).
- [12] T. Koshikawa, A. Nagai, Y. Yokohama, T. Hoshino, and Y. Ishizuki, *IEEE Trans. Magn.* **34**, 1471 (1998).

- [13] R. M. Langford and A. K. Petford-Long, *J. Vac. Sci. and Technol. A* **19** (5), 2186 (2001).
- [14] *xT Nova Nanolab User's Manual 4022 262 52351* .
- [15] C. P. Scott, A. J. Craven, P. Hatto, and C. Davies, *J. Microscopy* **182**, 186 (1996).
- [16] D. R. S. Cumming, S. Thoms, S. P. Beaumont, and J. M. R. Weaver, *Appl. Phys. Lett.* **68**, 332 (1996).

Chapter 3

Characterisation of extremely soft ferromagnetic thin films

3.1 Introduction

The magnetic anisotropy of thin films is important for the control of magnetic properties and soft magnetic films have attracted a lot of interest due to their applications in sensors. Previous studies have shown it is possible to induce anisotropy during deposition of thin films [1] or with a post-deposition anneal [2]. Egelhoff et al have looked at the properties of as deposited alloy films and, of the films investigated, found $\text{Ni}_{77}\text{Fe}_{14}\text{Cu}_5\text{Mo}_4$ had the softest properties [3].

As an introduction to the magnetisation reversal behaviour observed in the soft CoFe films which make up the majority of this thesis, two soft films which show comparatively simple reversal behaviour have been investigated. The samples were deposited by magnetron sputtering, as described in chapter 2, onto Si_3N_4 TEM membranes at the National Institute of Science and Technology in the USA and are described below.

SF1: $\text{Ni}_{77}\text{Fe}_{14}\text{Cu}_5\text{Mo}_4$ 25 nm / Al_2O_3 2.5 nm annealed in a rotating field of 200 Oe at 250° for 1 minute in air

SF2: $\text{Co}_{40}\text{Fe}_{40}\text{B}_{20}$ 7.5 nm / Al_2O_3 2 nm not annealed

The annealing step for film SF1 was carried out to stabilise the film, i.e. to prevent easy and hard axes forming over time. Film SF2 was not annealed to preserve the amorphous structure of the CoFeB as it was unclear whether annealing would partially crystallise the film. The films have been investigated using the Fresnel mode of Lorentz microscopy and with conventional transmission electron microscopy (CTEM).

3.2 Physical microstructure of NiFeCuMo and CoFeB thin films

Figure 3.1 shows bright field TEM images and diffraction patterns of SF1 and SF2. It can be seen from the bright field TEM image and diffraction pattern of SF1 the film has a crystalline structure (figure 3.1a). Over 100 measurements of the grain diameter were made using the particle sizing feature in the imaging software package Digital MicrographTM and the mean grain size was found to be 9.5 nm with a standard deviation of 1.6 nm. The bright field TEM image of CoFeB indicates the structure is amorphous as expected and this is backed up from the diffraction pattern which shows diffuse rings. It is also worth noting, in figure 3.1b, the presence of areas with black contrast of not dissimilar size to the crystallites in SF1 can be seen. The cause of this is unclear, but it is possible that there has been partial crystallisation of the film.

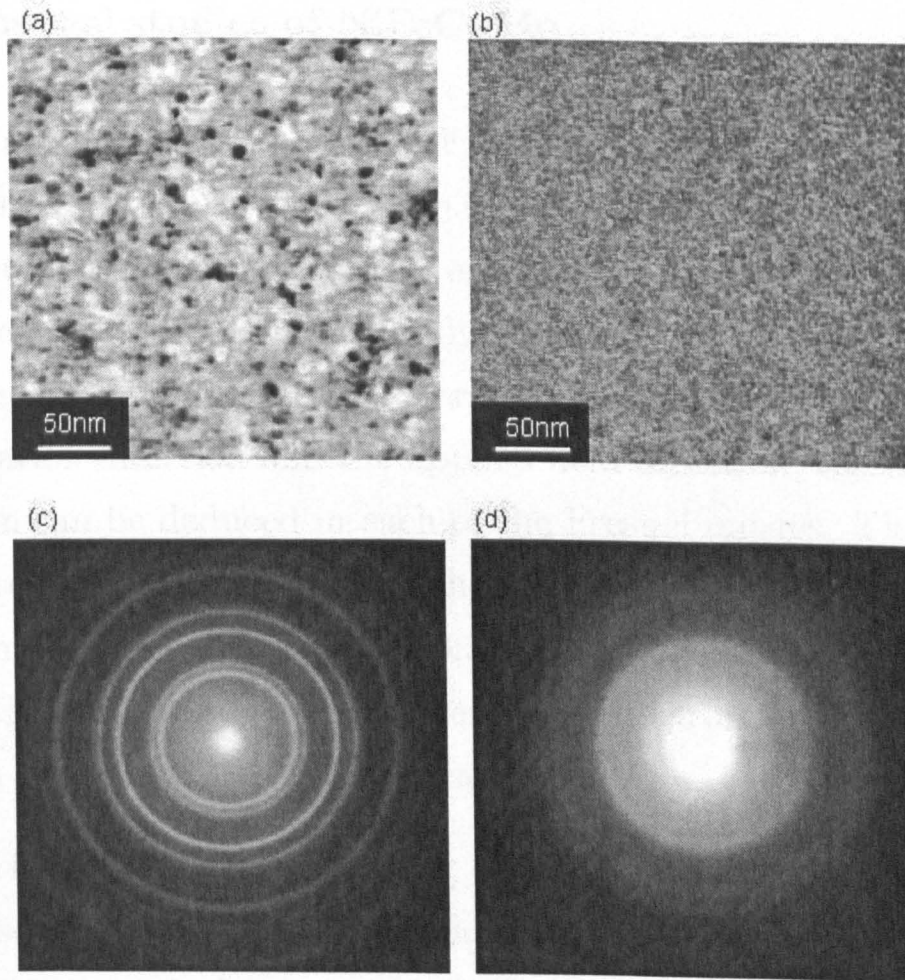


Figure 3.1: (a) and (b) Bright field TEM images of NiFeCuMo and CoFeB respectively and (c) and (d) corresponding diffraction patterns of NiFeCuMo and CoFeB.

3.3 Reversal mechanisms of NiFeCuMo and CoFeB thin films

The evolution of the magnetisation distribution of the two films have been investigated for orthogonal directions of applied field. The orthogonal directions were selected by varying the direction of applied field in 30° increments until mostly rotational behaviour was observed. The direction of applied field was then changed in 1° increments until purely rotational behaviour was observed consistent with a hard axis reversal. Images at various fields during the magnetisation reversal are shown for this direction of applied field and for the orthogonal direction. The applied field and magnetisation directions are indicated by red and white arrows respectively.

3.3.1 Fresnel studies of NiFeCuMo

Reversal along the hard axis of SF1 is shown in figure 3.2. The outward path (figures 3.2a-e) and the return path (figures 3.2f-j) were in agreement with reversal occurring entirely through magnetisation rotation. Given that there are generally simple processes occurring during reversal and assuming $M \propto \cos\theta$, where θ is the angle between the net magnetisation direction and the applied field direction, the net moment of the film can be deduced in each of the Fresnel images. This can then be used to plot the M-H loops. The hysteresis plot, deduced from the Fresnel images, is shown in figure 3.3 and is indicative of a hard axis reversal. The anisotropy field can then be found from the hysteresis loop as shown in figure 3.3 and in this case is ~ 1 Oe.

Figure 3.4 shows the reversal along the easy axis (the orthogonal direction to the hard axis) of SF1. On decreasing the applied field the ripple contrast was seen to increase (figure 3.4b). At -0.3 Oe regions of well-defined magnetisation orientation separated by low angle domain walls could readily be identified (figure 3.4c). A 180° domain wall, viewable in a transitory manner on the screen but not captured by the CCD camera, swept through effecting reversal leaving near-uniform magnetisation. An image after reversal is shown in figure 3.4d. The magnetisation direction then rotated through $\sim 8^\circ$ (measured using Digital MicrographTM) as the field was increased to -4.7 Oe (figure 3.4e) and reversal was completed. In a typical easy axis reversal the ripple dispersion would increase followed by a domain wall flashing through and a decrease in the ripple dispersion. The rotation observed here is not typical of an easy axis reversal and the reason for it is still unclear. The return path was entirely consistent with the outward path (figures 3.4f-j). The hysteresis loop for this reversal, deduced from the images,

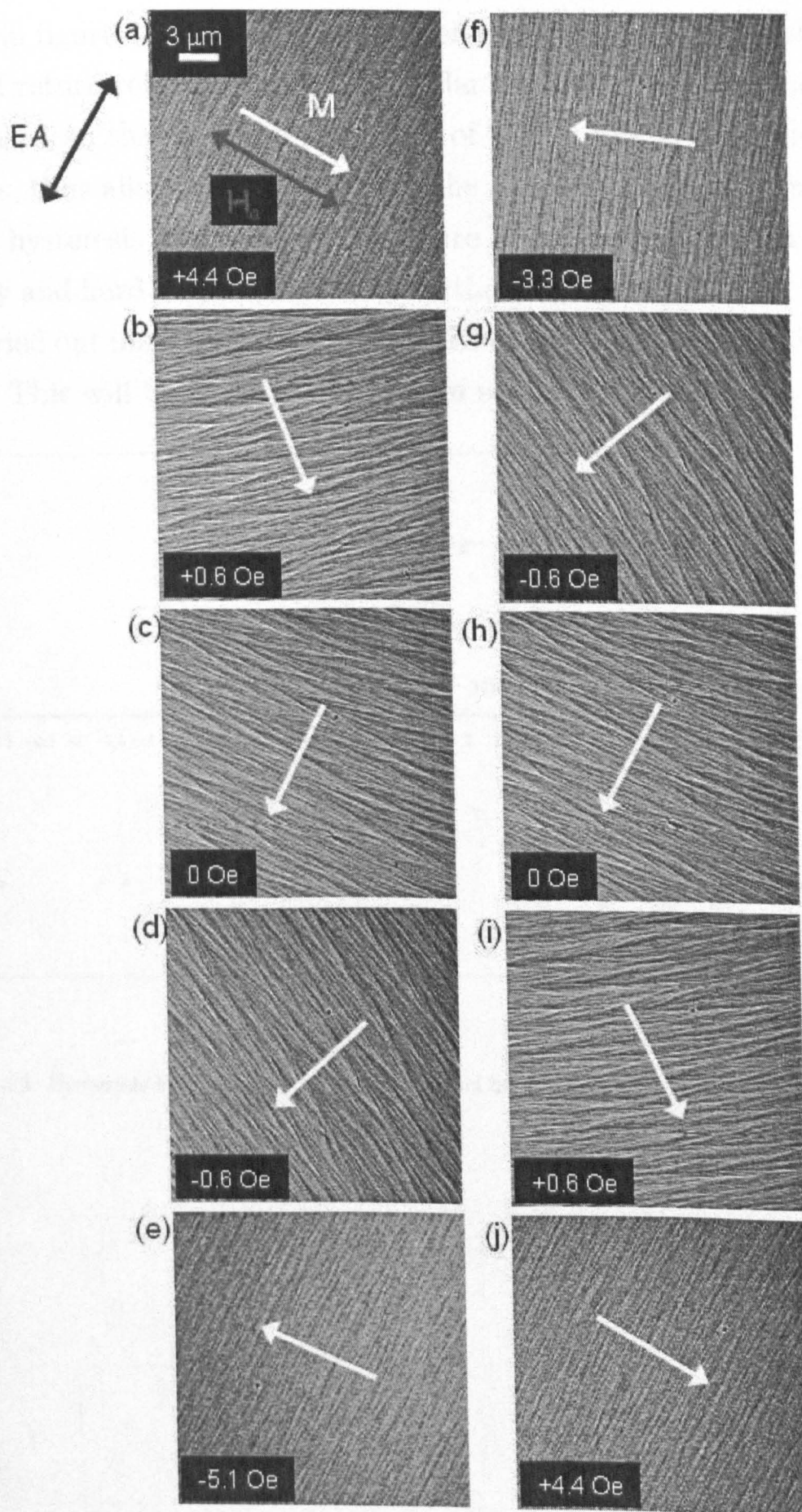


Figure 3.2: Reversal along the hard axis of NiFeCuMo with red arrows indicating the direction of applied field and the white arrows the magnetisation direction

is shown in figure 3.5 and indicates a coercivity of ~ 0.4 Oe. As the outward and return reversal were very similar the hysteresis plot has been symmetrised so that a greater number of points are included in both directions, thus allowing a better fit of the shape of the loop. The symmetrised hysteresis plot is shown in figure 3.6. The observation of distinct easy and hard axes is in contrast to the looper measurements which were carried out immediately after deposition and indicated isotropic behaviour. This will be discussed further in section 3.4.

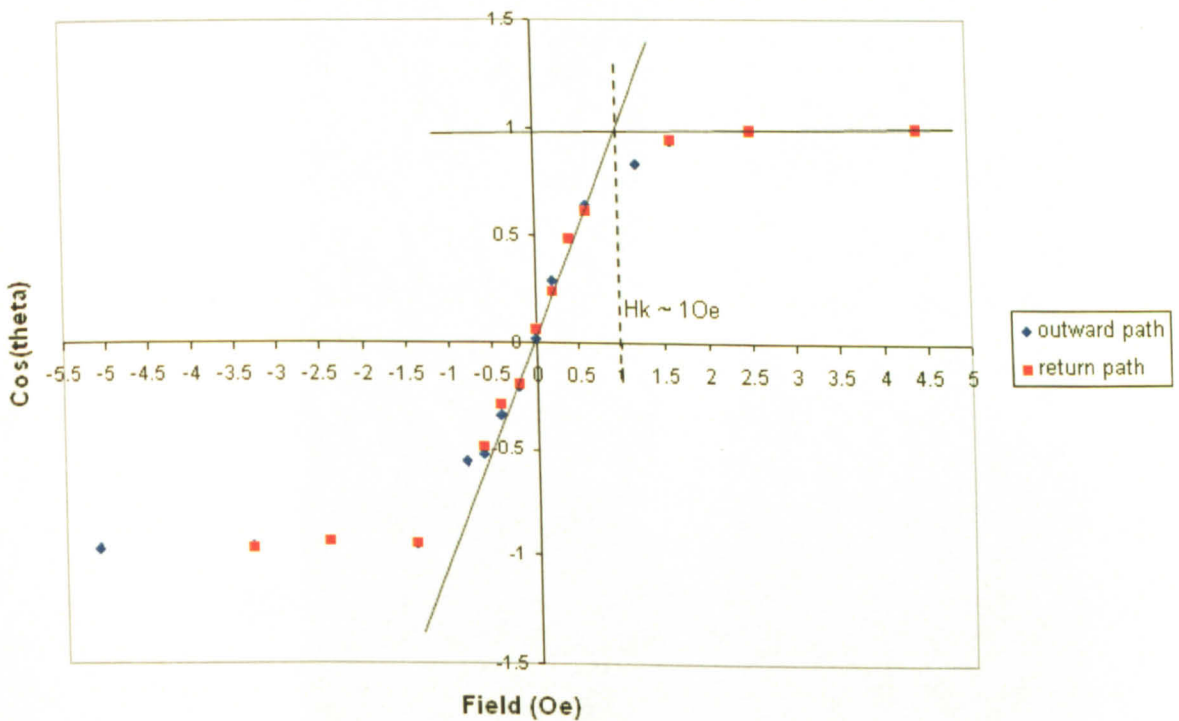


Figure 3.3: Hysteresis loop calculated from the Fresnel images for the hard axis of NiFeCuMo

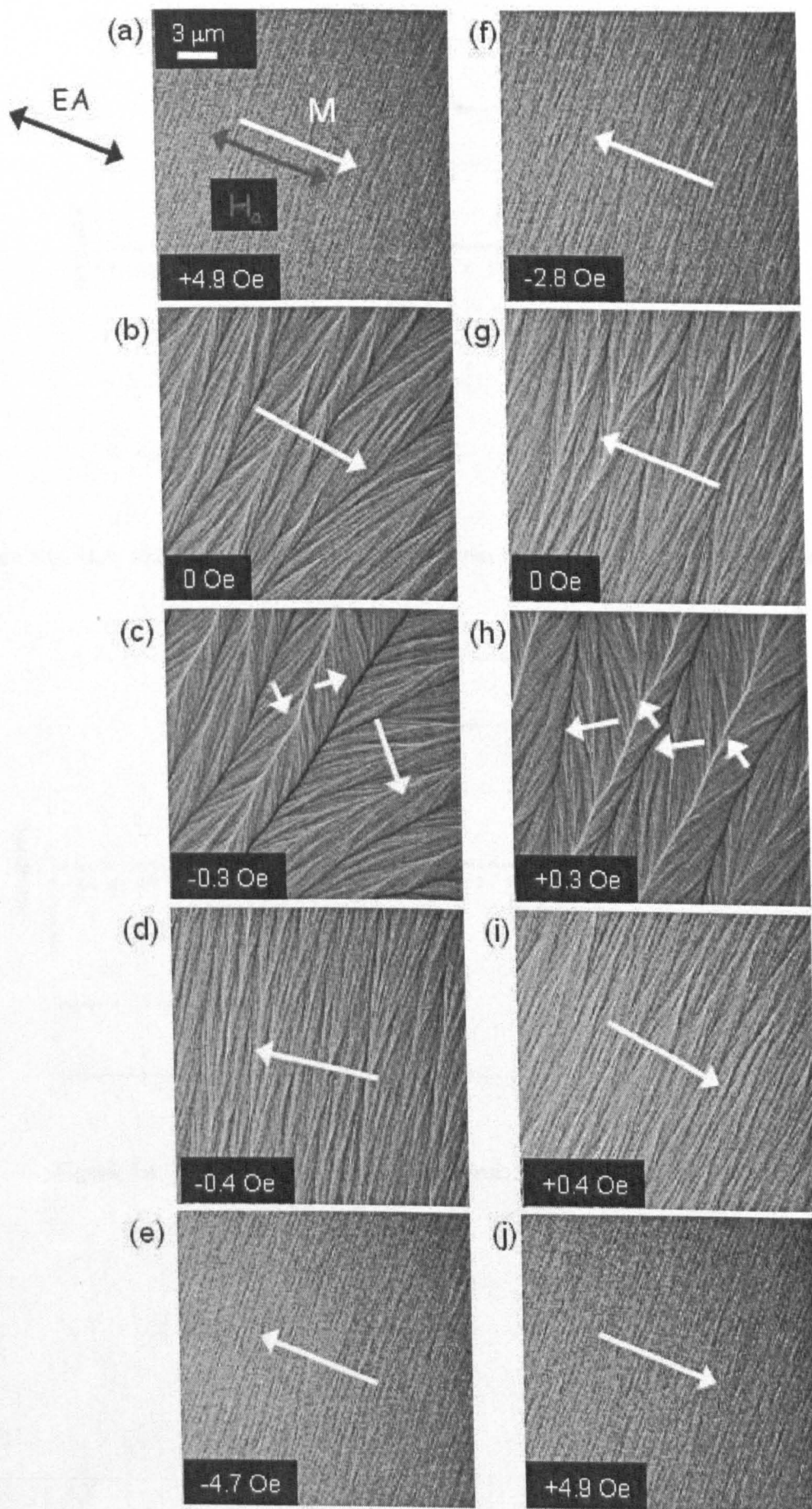


Figure 3.4: Reversal along the easy axis of SF1, NiFeCuMo, with red arrows indicating the direction of applied field and the white arrows the magnetisation direction

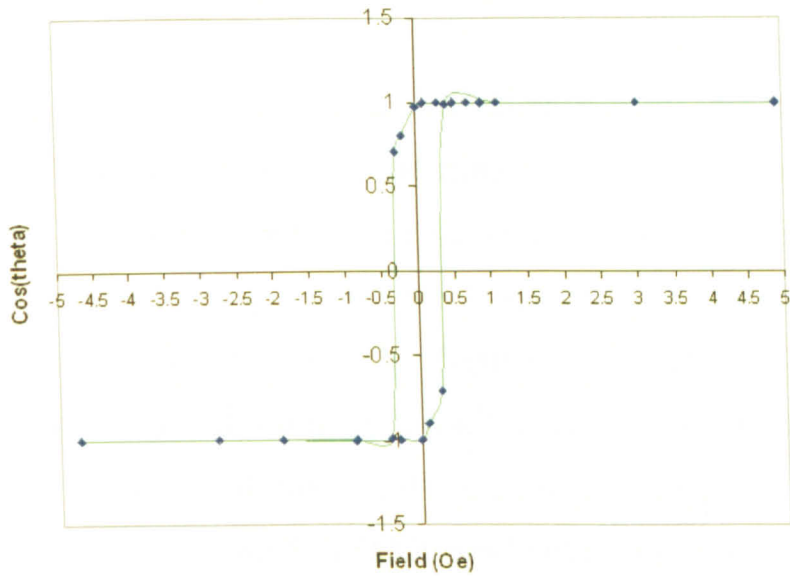


Figure 3.5: Easy axis hysteresis loop calculated from the Fresnel images for NiFeCuMo

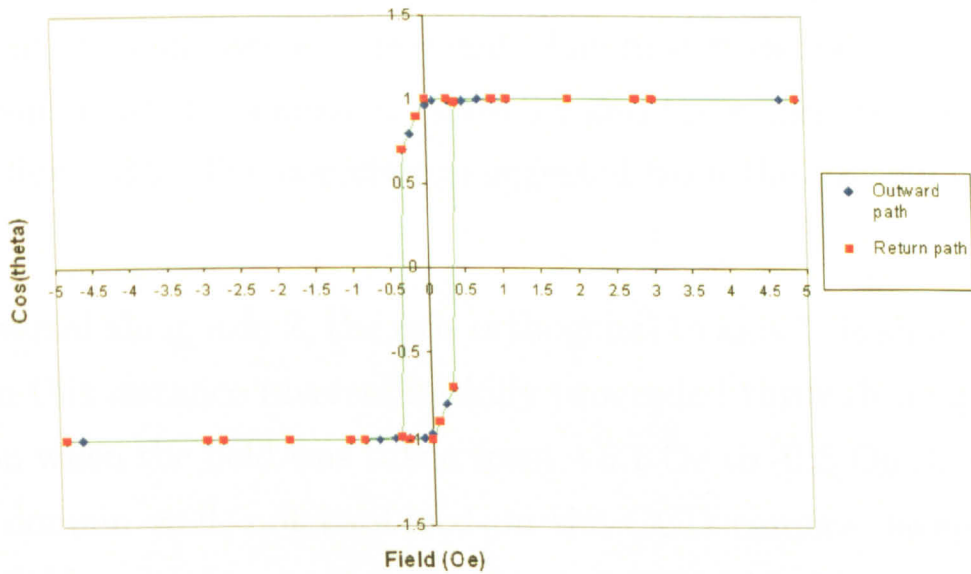


Figure 3.6: Easy axis symmetrised hysteresis loop for SF1, NiFeCuMo.

3.3.2 Fresnel studies of CoFeB

The second film studied was SF2, a CoFeB thin film. As with SF1 the applied field direction was varied until magnetisation processes consistent with a primary axis was observed, in this case an easy axis magnetisation reversal. The reversal along a this axis is shown in figure 3.7. As the field was taken from +5.7 Oe to -0.8 Oe (figure 3.7a-c the ripple contrast intensified. Reversal was effected by a highly mobile domain wall, observed on the viewing screen, but not captured on the CCD camera, sweeping through between -0.8 Oe and -1.0 Oe and reversal was completed (figure 3.7d). As the field was further increased to -5.0 Oe the ripple contrast decreased in intensity as expected (figure 3.7e). The return path was entirely consistent with the outward path (figure 3.7f-j). The images are consistent with an easy axis reversal. The hysteresis loop deduced from the Fresnel images is shown in figure 3.8 and the symmetrised hysteresis plot in figure 3.9. The coercivity suggested from the Fresnel study is ~ 0.9 Oe.

The reversal along axis 2, the axis orthogonal to axis 1, is shown in figure 3.10. In this instance reversal initially proceeded through magnetisation rotation when the field was taken from +5.7 Oe to -0.5 Oe (figure 3.10a-c). A domain wall, not captured on the CCD camera, swept through as the field was taken to -1.0 Oe (figure 3.10d). At this point there has been an over shoot of the magnetisation direction. On further increasing the field to -5.0 Oe the magnetisation rotated back to the applied field direction and reversal was completed (figure 3.10e). Again the return path was in agreement with the outward path, although in this instance the domain wall which effected reversal was captured on the CCD camera (figure 3.10i). Figures 3.11 and 3.12 show the hysteresis plot deduced from the images and the symmetrised plot respectively. The film reversed at a similar field to axis 1, ~ 0.8 Oe.

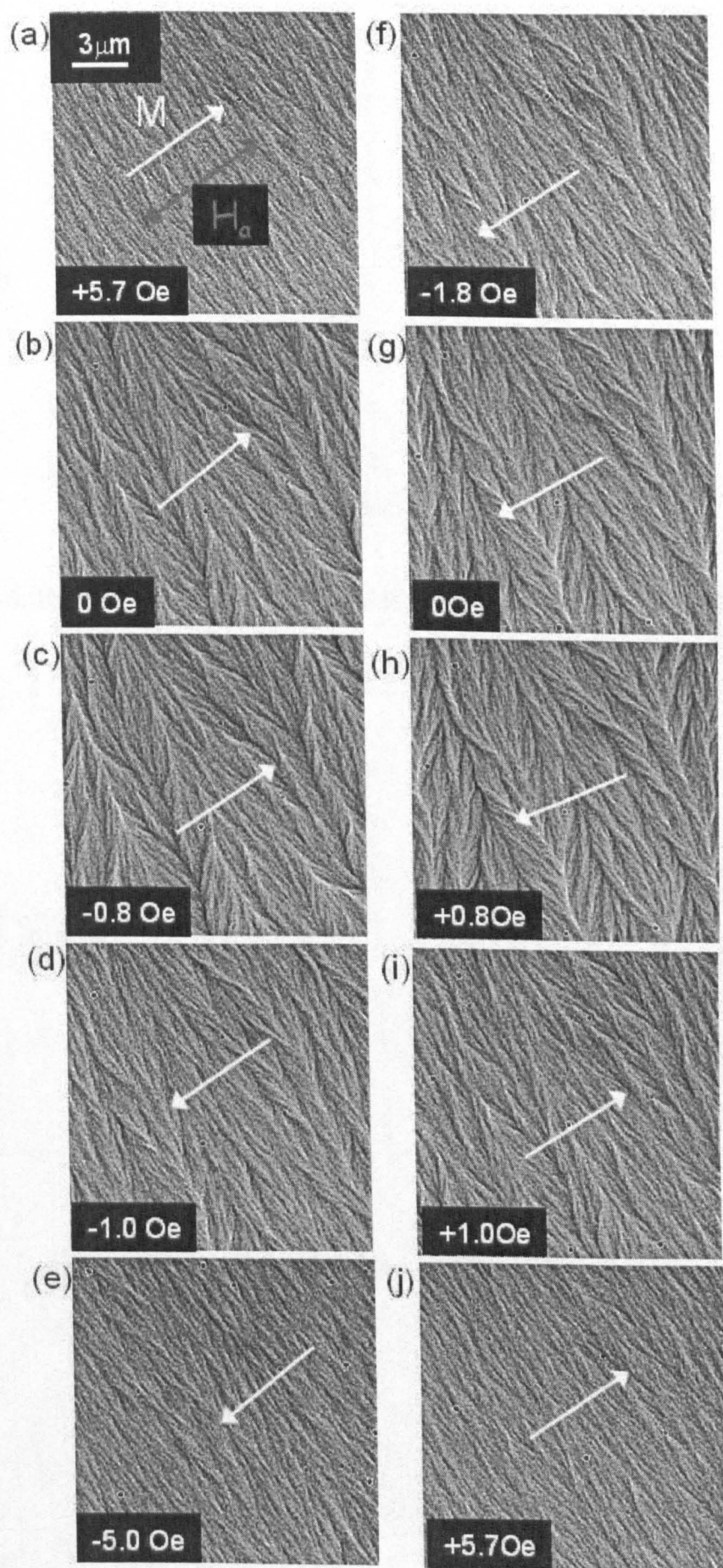


Figure 3.7: Reversal along axis 1 of SF2, CoFeB, with red arrows indicating the direction of applied field and the white arrows the magnetisation direction

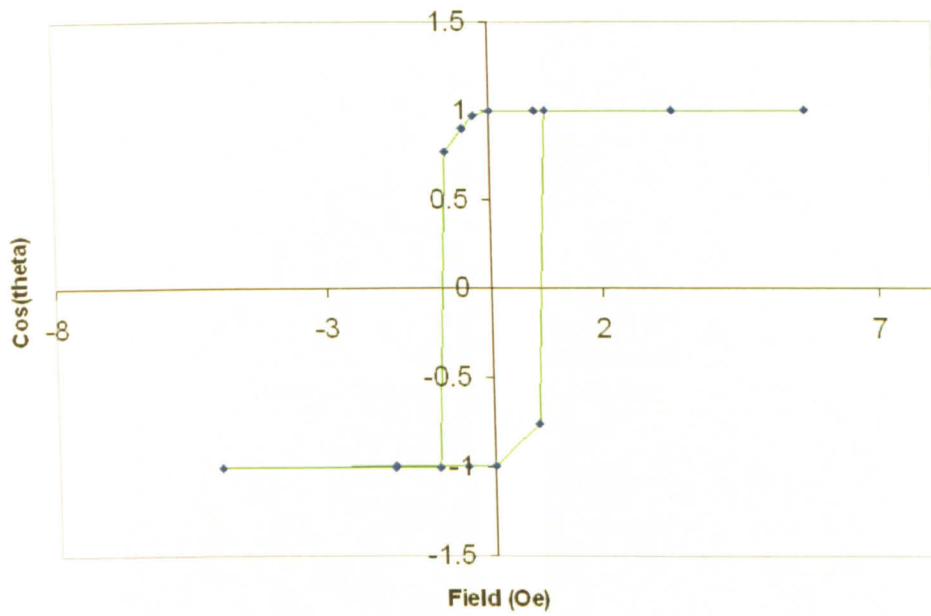


Figure 3.8: Hysteresis loop calculated from the Fresnel images for SF2, CoFeB, axis 1

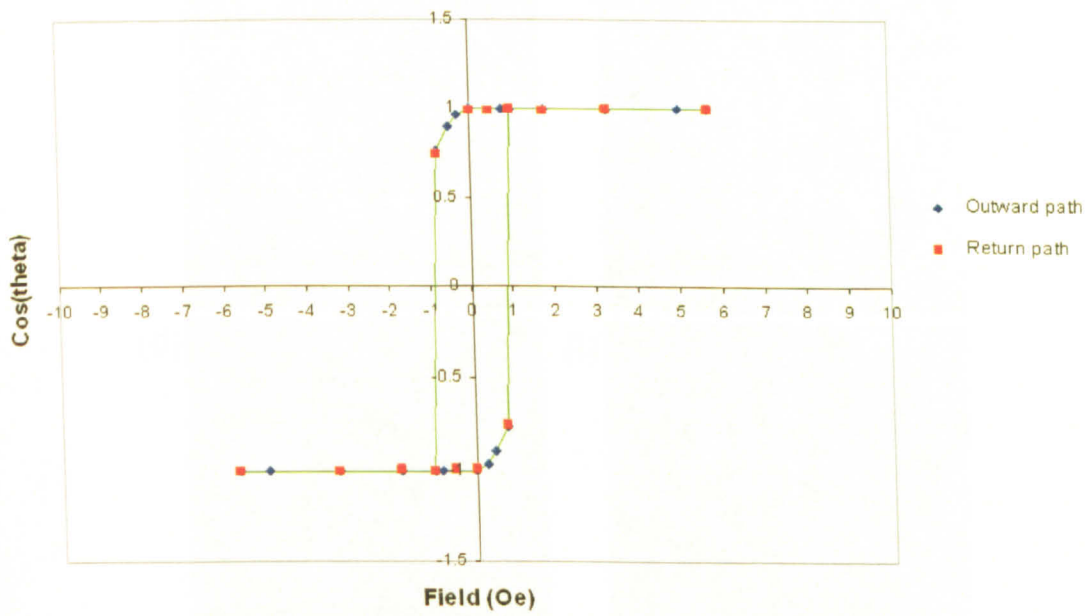


Figure 3.9: Symmetrised hysteresis loop for SF2, CoFeB, axis 1

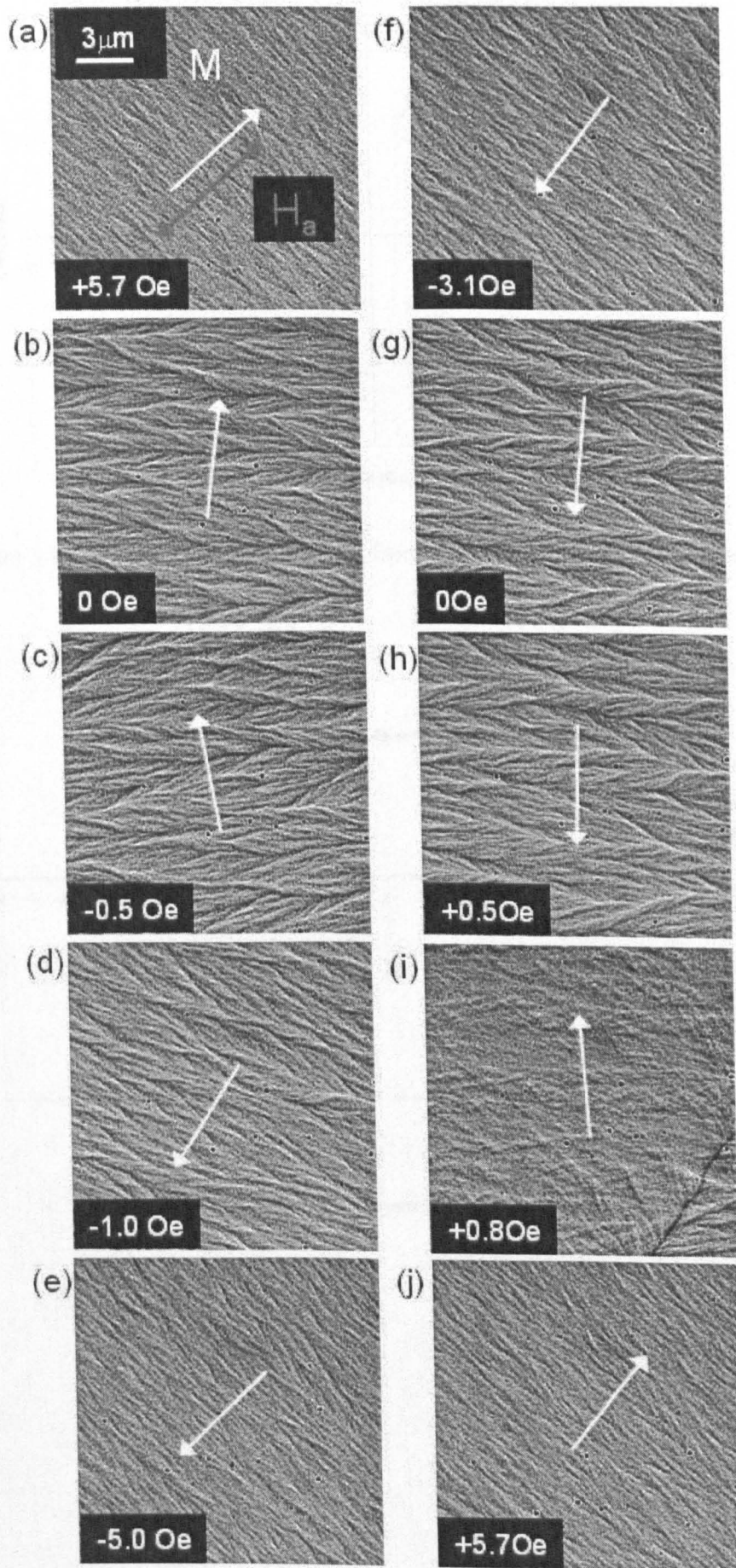


Figure 3.10: Reversal along axis 2 of SF2 with red arrows indicating the direction of applied field and the white arrows the magnetisation direction

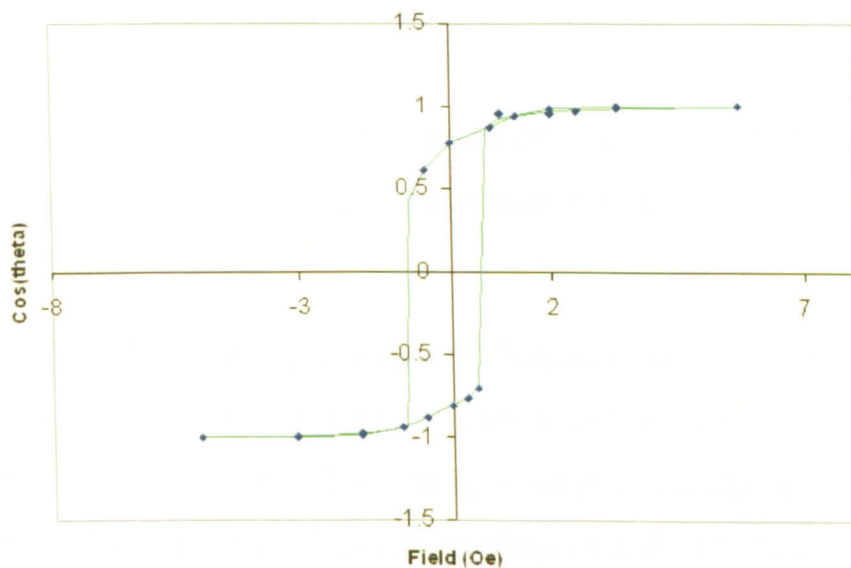


Figure 3.11: Hysteresis loop calculated from the Fresnel images for SF2 axis 2

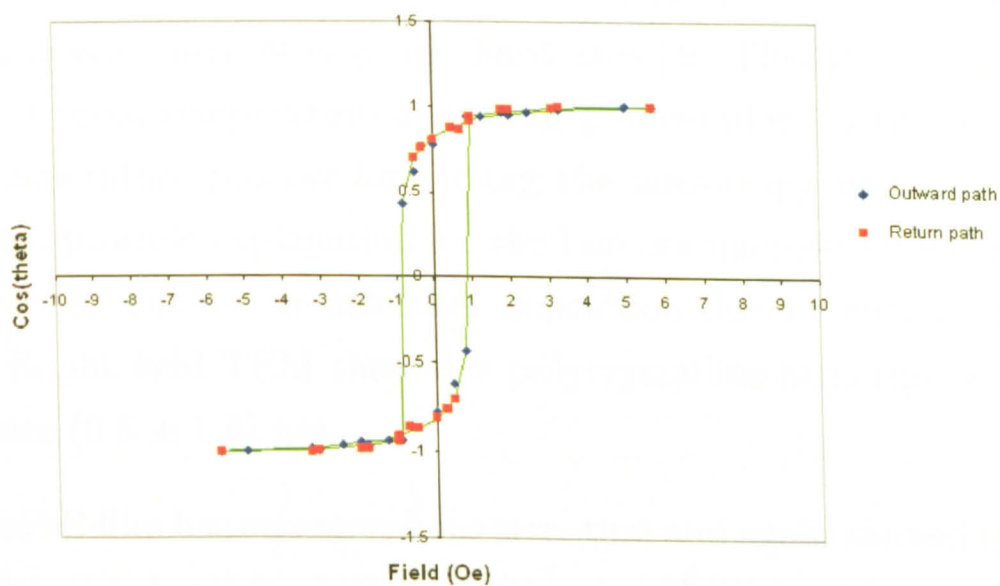


Figure 3.12: Symmetrised hysteresis loop for SF2 axis 2

3.4 Discussion

The Fresnel mode of Lorentz microscopy has provided insight into the magnetisation processes occurring during reversal in NiFeCuMo and CoFeB thin films.

For the NiFeCuMo film anisotropic behaviour was observed with an easy axis coercivity of ~ 0.4 Oe. The hard axis reversal indicated an anisotropy field of ~ 1 Oe. This is in contrast to the results of Egelhoff et al [3] which indicated as deposited films of NiFeCuMo showed isotropic behaviour with a coercivity of ~ 0.4 Oe. However, previous studies on films (which, unlike SF1, have not been stabilised by an annealing step) at NIST indicated that there was a loss of softness over time accompanied by development of easy and hard axes [4]. This was thought to be due to a room temperature annealing process akin to the well known high-temperature process for setting the anisotropy of permalloy and may be a possible explanation for the Lorentz microscopy results which were carried out ~ 1 month after deposition due to microscope problems. Bright field TEM showed a polycrystalline structure with mean grain size (9.5 ± 1.6) nm.

The CoFeB film has an amorphous structure and again showed quite simple reversal behaviour. Although the reversal mechanism in orthogonal directions differed, the film switched at the same field value indicating a coercivity of ~ 0.8 Oe and it was difficult to distinguish a strong anisotropy axis in the film.

A significant difference between the two films investigated is the appearance of the magnetisation ripple. This can be seen by comparison of the hard axis magnetisation reversal of NiFeCuMo (figure 3.2) and the reversal along axis 2 of the CoFeB film (figure 3.10). The appearance of the ripple during the reversal of the NiFeCuMo film did not significantly change whereas during the CoFeB reversal the magnetisation ripple became less coherent as the field was reduced to 0 Oe. This is entirely

consistent with the fact that the NiFeCuMo has a defined anisotropy axis as opposed to the lack of anisotropy in the CoFeB film.

This chapter has shown some of the reversal mechanisms which can occur in soft magnetic thin films and similar reversal processes to those observed in both the NiFeCuMo and the CoFeB film are observed during the reversal of soft CoFe films. Results from four initial CoFe based films are presented in chapter 4.

Bibliography

- [1] A. Miktus, J. Wenda, and K. Kulakowski, *J. Magn. Magn. Mater.* **160**, 341 (1996).
- [2] D. Garcia *et al.*, *IEEE Trans. Magn.* **34** (4), 1153 (1998).
- [3] W. E. Egelhoff *et al.*, *Thin Solid Films* **505**, 90 (2006).
- [4] W. E. Egelhoff, Private Communication .

Chapter 4

Magnetic characterisation of CoFe single and multilayer films

4.1 Introduction

To gain a greater understanding of the properties of write pole materials the effect on the micromagnetic structure of a seedlayer, a spacer layer and of laminating CoFe films has been investigated. Lorentz microscopy, as discussed in chapter 2, has been used to observe the magnetisation reversal processes of four CoFe films and cross-sectional transmission electron microscopy (TEM) has been used to correlate the observations with the physical microstructure.

Four films of similar total thickness, 50 nm, were investigated. In all cases the composition of the magnetic layers was $\text{Co}_{35}\text{Fe}_{65}$ (written hereafter as CoFe). Only in one case was the film a single magnetic layer; in the other three films one or more seed and/or spacer layers were also present. Seed layers were 1nm thick $\text{Ni}_{82.5}\text{Fe}_{17.5}$ (written hereafter as NiFe) layers and spacer layers were of Al_2O_3 , 1.5nm thick. The structure of the four films can be written as CoFe (M1), NiFe/CoFe (M2), NiFe/CoFe/ Al_2O_3 /NiFe/CoFe (M3) and NiFe/CoFe/(Al_2O_3 /CoFe/NiFe) $\times 3$ (M4) as illustrated in figure 4.1 and table 4.1. All layers were grown by sputter deposition; RF sputtering

was used for Al_2O_3 and DC sputtering for CoFe and NiFe. For TEM observations the films were deposited on ~ 50 nm thick Si_3N_4 membranes supported by Si with a $100 \mu\text{m} \times 100 \mu\text{m}$ electron transparent window [1]. A uniaxial anisotropy was induced in the films by depositing them in a field of ≈ 60 Oe, around the same order of magnitude as previous studies on high moment materials [2]. Easy and hard axis hysteresis loops for each film were determined using a SHB model 109 hysteresis loop tracer operating at 50 Hz.

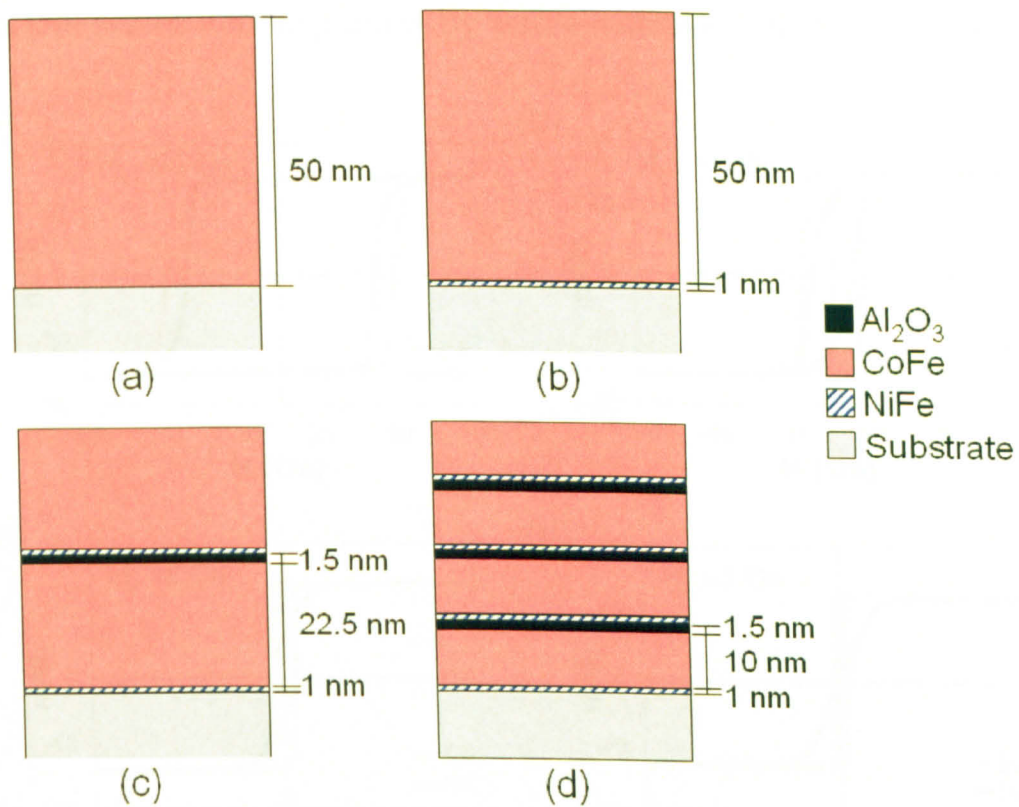


Figure 4.1: Schematic showing the structures of (a) CoFe (M1), (b) NiFe/CoFe (M2), (c) NiFe/CoFe/ Al_2O_3 /NiFe/CoFe (M3) and (d) NiFe/CoFe/(Al_2O_3 /CoFe/NiFe) $\times 3$ (M4).

Film name	Total t (nm)	CoFe t (nm)	Number of CoFe layers	Seed t (nm)	Spacer t (nm)	Total number of layers
M1	50	50	1	-	-	1
M2	51	50	1	1	-	2
M3	48.5	22.5	2	1	1.5	5
M4	48.5	10	4	1	1.5	11

Table 4.1: Reference table for film structures M1, M2, M3 and M4

4.2 B-H loop measurements

Figure 4.2 shows the hysteresis loops from the B-H loop measurements on the four films. The single CoFe layer film, figure 4.2a, showed near-isotropic behaviour with a coercivity of 55 Oe as expected from previous studies [3]. The other three films had well-defined uniaxial hysteresis loops with easy axis coercivities of around 17 Oe, 5 Oe and 3 Oe respectively, figures 4.2b-d. The widths of the hard axis loops decreased through the series accompanied by some variation in their shape.

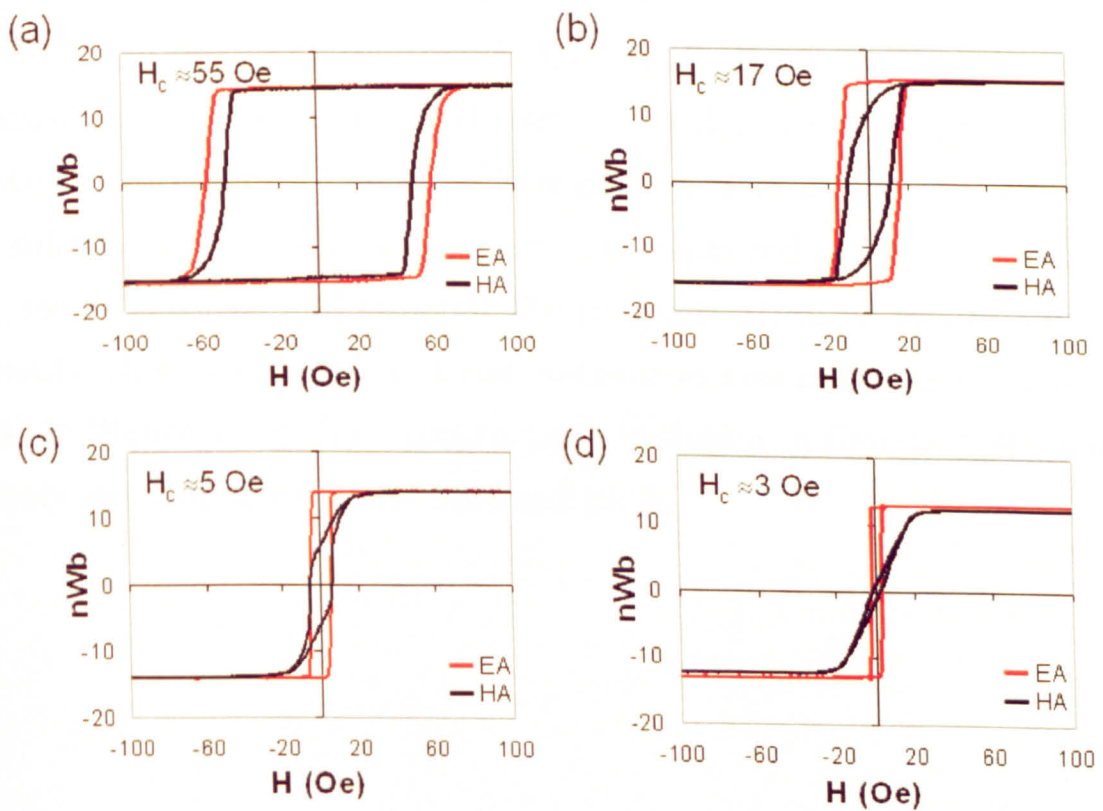


Figure 4.2: Easy and Hard axis B-H loops for (a) M1, (b) M2, (c) M3 and (d) M4

4.3 Easy and hard axis reversal mechanisms of CoFe single layer films

TEM observation of the magnetisation reversal of film M1, the CoFe single layer, is shown in figure 4.3. Magnetisation ripple is apparent in all images and is of higher contrast and much more irregular than in the other three films. These observations are consistent with a high degree of magnetisation dispersion and an ill-defined uniaxial anisotropy axis. Indeed, rather similar behaviour, consistent with the small difference between the easy and hard axis loops, was observed irrespective of the direction of the applied field. In a typical reversal sequence, ripple contrast intensified as the field was changed from a high negative to a positive field (figures 4.3a-c). Thereafter, a domain wall, observable on the microscope viewing screen but not captured using the CCD camera, swept through and effected the magnetisation reversal. The ripple intensity then decreased and magnetisation reversal was completed by +76 Oe (figure 4.3e). The return path is shown in figures 4.3f-j and was entirely consistent with the outward path.

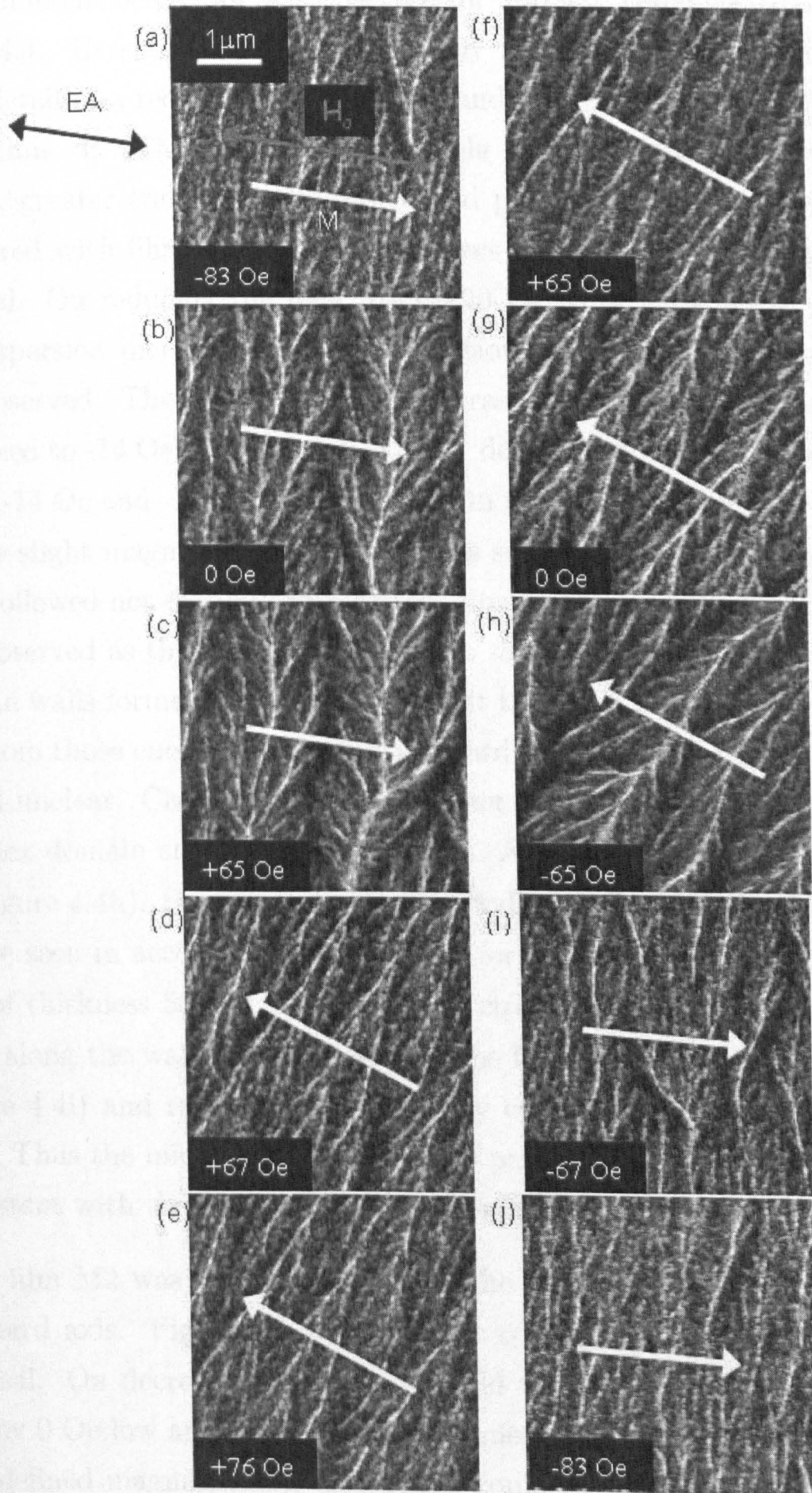


Figure 4.3: Easy axis magnetisation reversal of M1, CoFe50 nm, with red arrows indicating the direction of applied field and the white arrows the mean magnetisation direction.

Quite different behaviour was observed for film M2, the NiFe/CoFe film, figure 4.4. Here the results more closely resembled those analysed in some detail in a recent paper on ripple and wall structures in soft magnetic films [4]. The magnetisation ripple showed much improved regularity, greater transverse coherence and preferred directionality when compared with film M1. Figure 4.4 shows the easy axis magnetisation reversal. On reducing the field from +20 Oe to -3 Oe (figures 4.4a-b) the dispersion increased and the formation of low angle domain walls was observed. The ripple and wall contrast intensified as the field was increased to -14 Oe (figure 4.4c). A 180° domain wall swept through between -14 Oe and -15 Oe (figure 4.4d). On further increasing the field to -25 Oe slight magnetisation rotation was seen (figure 4.4e). The return path followed not dissimilar processes. However, magnetisation rotation was observed as the field was reduced to -3 Oe (figure 4.4f). After this, domain walls formed (Figure 4.4g), albeit the walls were at different angles from those encountered in the outward reversal. The reason for this is still unclear. Changing the field by just 1 Oe led to a comparatively complex domain structure (figure 4.4h). A wall swept through at +14 Oe (figure 4.4h). Here cross-tie domain walls (as discussed in chapter 1) can be seen in accord with expectation for 180° domain walls in a soft film of thickness 50 nm [5]. The green circles indicate vortex/cross-tie pairs along the wall. The majority of the film had reversed by +15 Oe (figure 4.4i) and reversal was essentially completed by +20 Oe (figure 4.4j). Thus the microscope observations predict a coercivity of ≈ 15 Oe, consistent with the hysteresis loop measurements (figure 4.2b).

Next film M2 was oriented such that the field was applied parallel to the hard axis. Figures 4.5a-e show the outward and 4.5f-j the return reversal. On decreasing the applied field the ripple contrast increased and by 0 Oe low angle domain walls formed (figure 4.5b). Regions with well-defined magnetisation orientation could readily be identified by -3 Oe (figure 4.5c). In essence the magnetisation in some local areas of film began rotating clockwise towards one easy direction whilst elsewhere the

magnetisation rotated counterclockwise towards the other. At a field of -3 Oe, the magnetisation, as gauged from the ripple directions in the various domains, had rotated through approximately 45° so that the resulting walls are 90° in character. Hence the magnetic moment in the field direction was still $\approx 70\%$ of its initial value. Thereafter the walls were swept away leaving near-uniform magnetisation at -8 Oe (figure 4.5d) whereafter further increase of field simply rotated the magnetisation towards the field direction (figure 4.5e). The return path again showed similar processes to the outward path (figs 4.5f-j). From the corresponding hysteresis loop in figure 4.2b it is expected that reversal proceeds slowly and then more rapidly, which is in agreement with the Lorentz microscopy study.

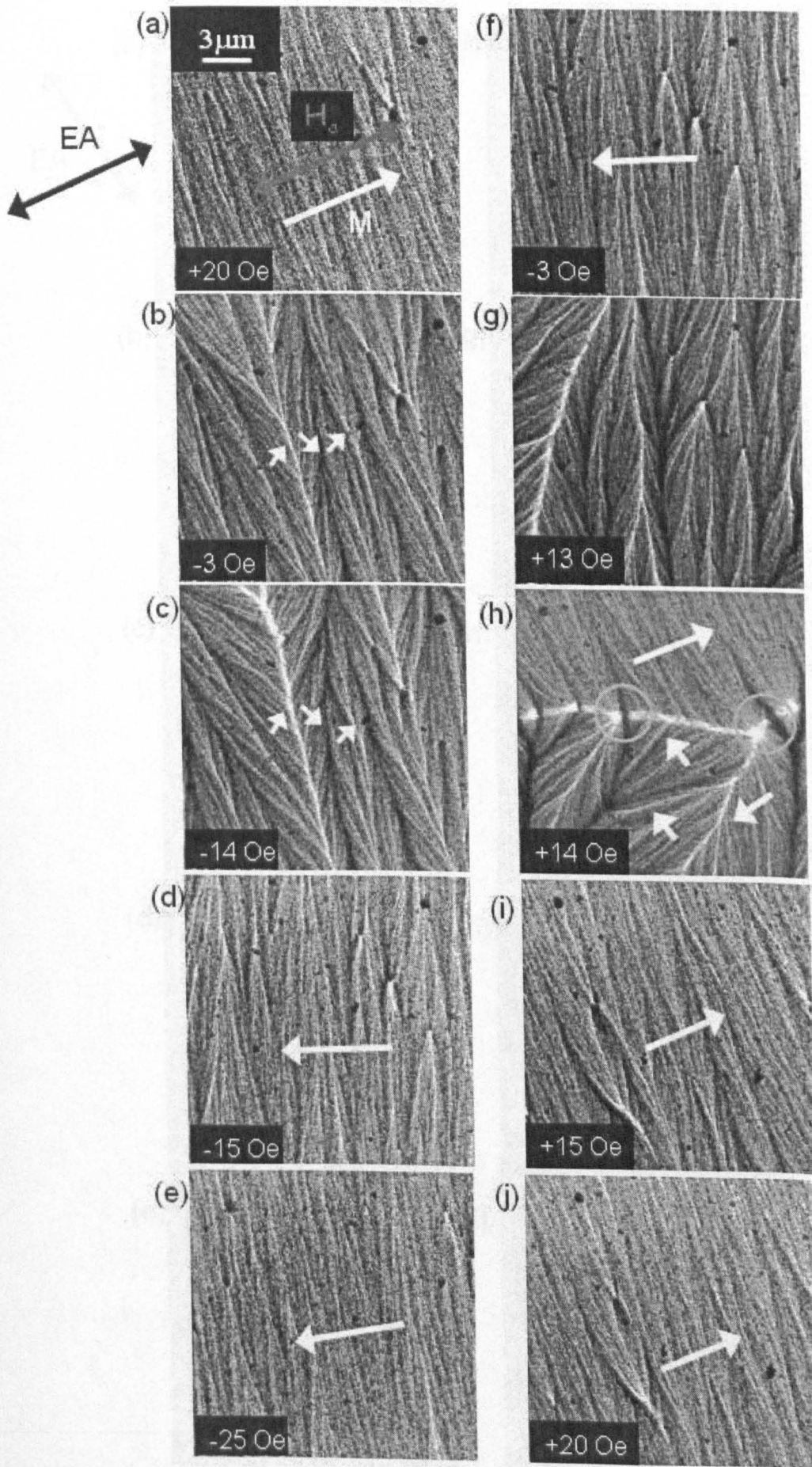


Figure 4.4: Easy axis magnetisation reversal of M2, NiFe1nm/CoFe50nm, with red arrows indicating the direction of applied field and the white arrows the magnetisation direction. The green circles indicated vortex/cross-tie pair along the cross-tie domain wall.

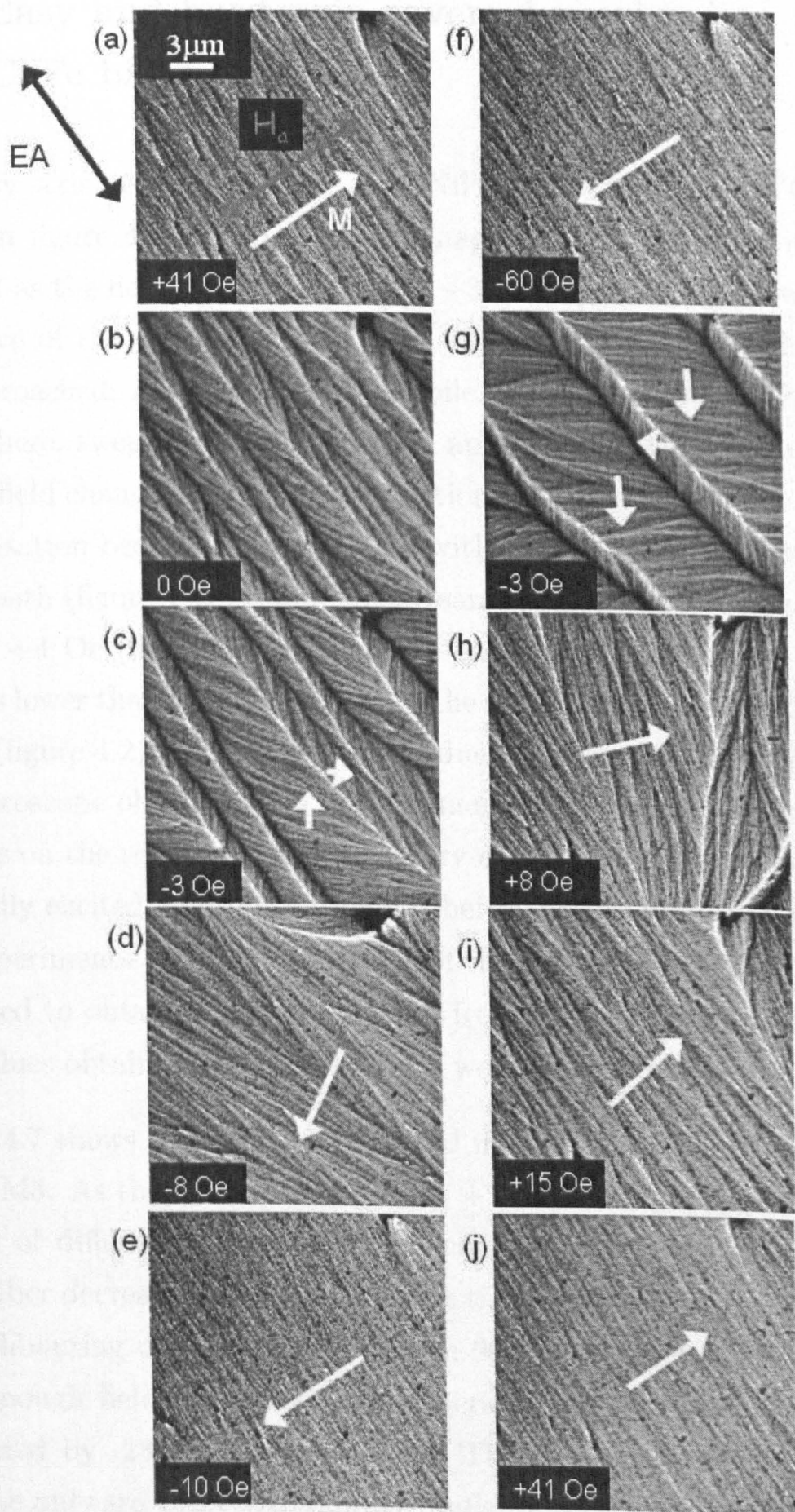


Figure 4.5: Hard axis magnetisation reversal of M2, NiFe1nm/CoFe50nm, with red arrows indicating the direction of applied field and the white arrows the magnetisation direction.

4.4 Easy and hard axis reversal mechanism of the CoFe bilayer system

The easy axis reversal of film M3, NiFe/CoFe/Al₂O₃/NiFe/CoFe, is shown in figure 4.6. As before, the magnetisation ripple contrast intensified as the field was changed from +35 Oe to +5 Oe (figure 4.6a-c), indicative of the expected increase in dispersion as the switching field was approached. At -3 Oe a highly mobile domain wall, not visible in the images here, swept through leading to an abrupt reversal (figure 4.6d); further field change led only to a reduction of ripple contrast as the local magnetisation became better aligned with the field (figure 4.6e-f). The return path (figure 4.6f-j) followed the same process with reversal occurring by +4 Oe (figure 4.6i), giving an easy axis coercivity of $\sim 3-4$ Oe which is lower than the value given by the B-H loop measurements, i.e. 5.3 Oe (figure 4.2). This is most likely due to the hysteresis properties of the microscope objective lens. The remanent state of the objective lens depends on the recent excitation history of the lens. If the lens had not been fully excited and fully turned off before performing the magnetisation experiments, the remanent state of the lens would be different than that used to obtain a field calibration from the lens current, hence the field values obtained for the coercivity would be inaccurate.

Figure 4.7 shows images of the reversal mechanism along the hard axis of film M3. As the field was lowered to +7 Oe domain walls formed and regions of differing magnetisation orientation were seen (figure 4.7b). On further decreasing the field to -1 Oe the orientation of magnetisation in neighbouring domains changed from 90° to 180° (figure 4.7c). At a large enough field the domain walls were annihilated and reversal was completed by -23 Oe (figure 4.7d-f). The return path was consistent with the outward path with domain walls forming and remaining to +5 Oe followed by rotation of magnetisation (figure 4.7f-j). The images suggest the film has near zero remanence which is inconsistent with the

shape of the B-H loop in figure 4.2c. This can be explained by a slight misalignment of the applied field with the hard axis direction in the B-H loop measurement. Figure 4.8 shows the reversal mechanism with the applied field $\sim 1^\circ$ from the hard axis. The reversal proceeded through magnetisation rotation followed by a discrete jump in magnetisation as a wall swept through at -5 Oe (figure 4.8c). Thereafter further steady rotation with field completed the reversal process. This is in broad agreement with the shape of the B-H loop, figure 4.2c, which shows a jump at ≈ 5 Oe. From these results it is apparent that the shape of the hysteresis loop is quite sensitive to orientation in the vicinity of the hard axis.

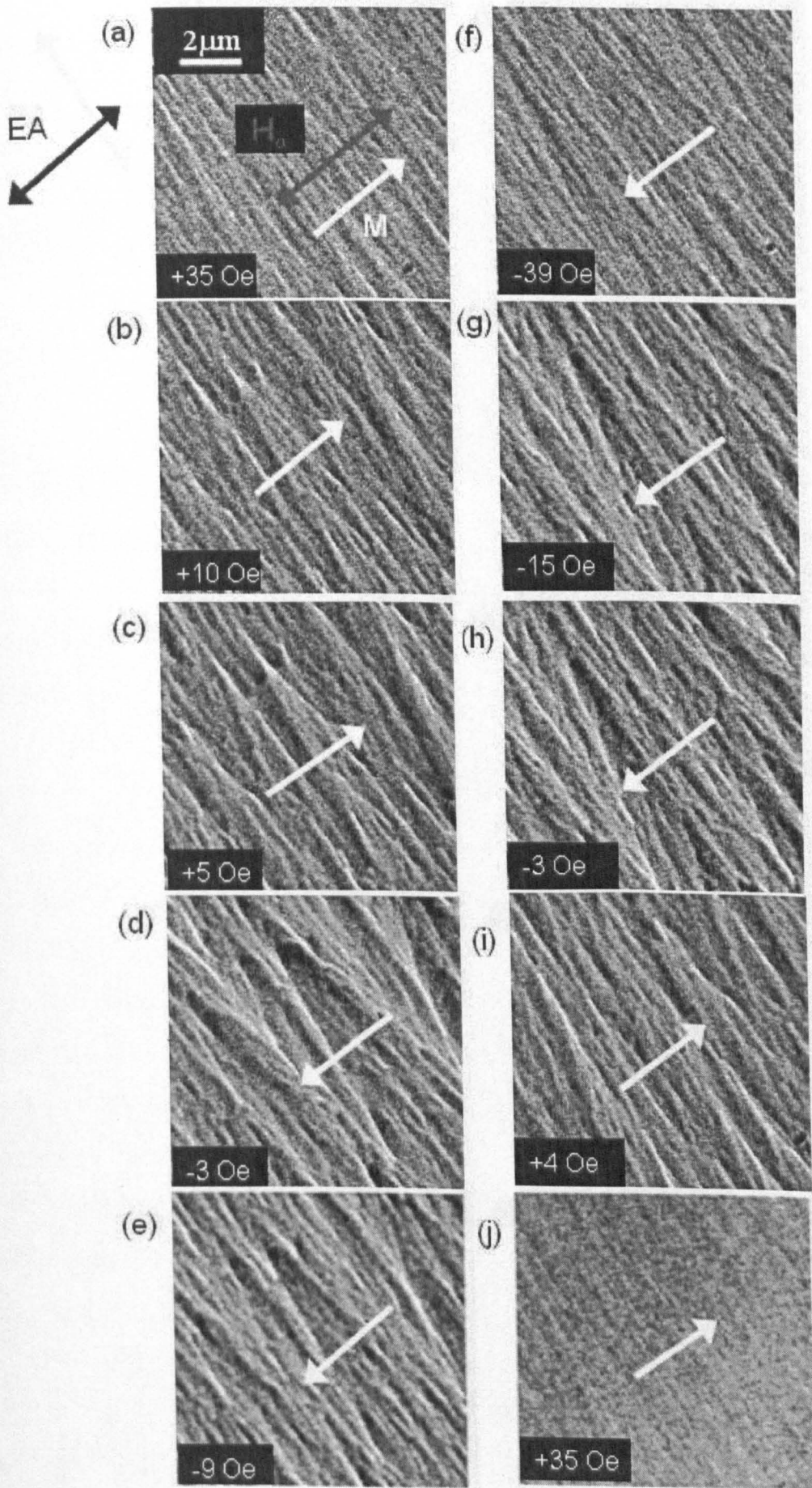


Figure 4.6: Easy axis magnetisation reversal of M3, NiFe1nm/CoFe22.5nm/Al₂O₃1.5nm/NiFe1nm/CoFe22.5nm, with red arrows indicating the direction of applied field and the white arrows the magnetisation direction.

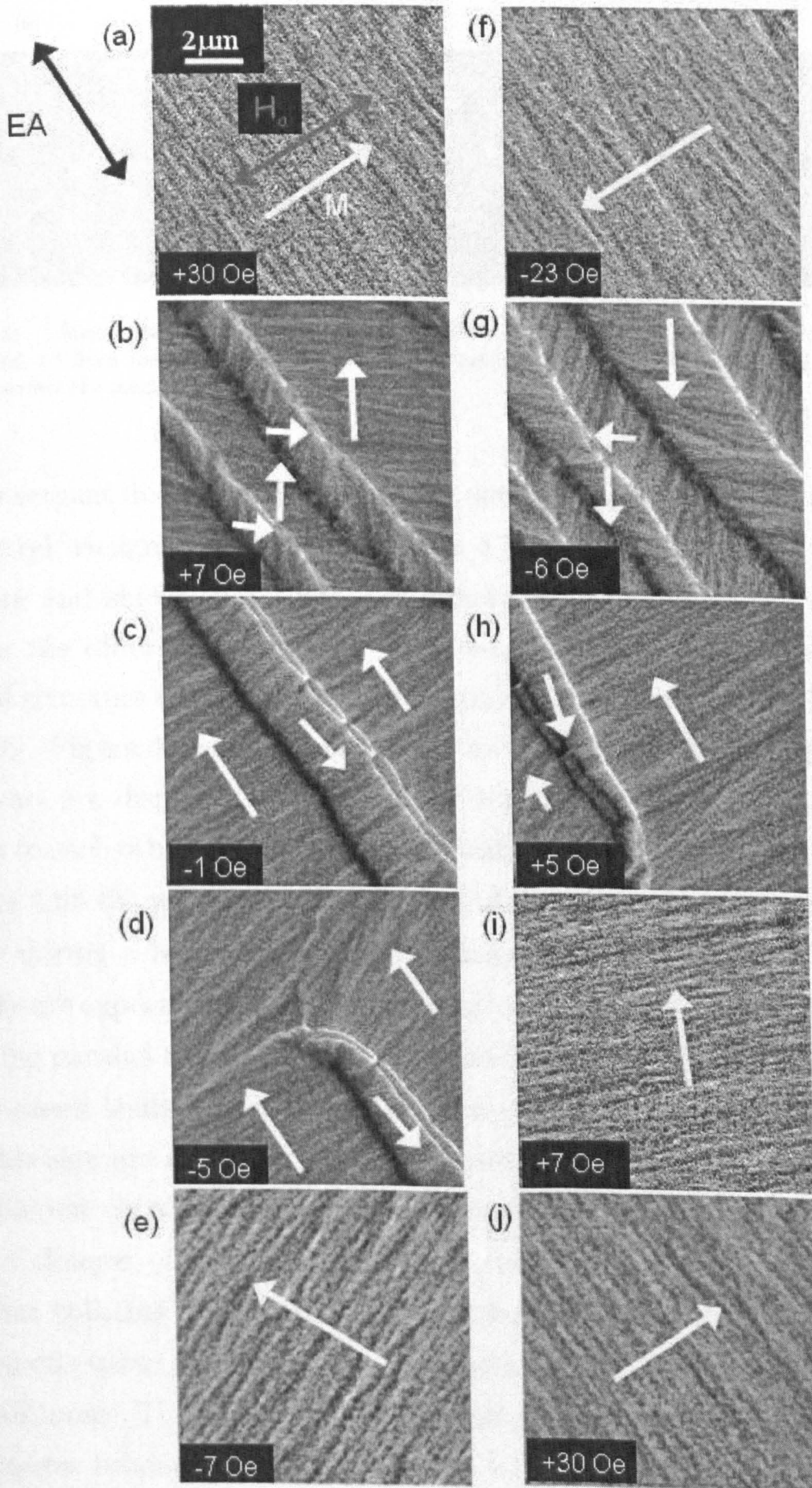


Figure 4.7: Hard axis magnetisation reversal of M3, NiFe1nm/CoFe22.5nm/Al₂O₃1.5nm/NiFe1nm/CoFe22.5nm, with red arrows indicating the direction of applied field and the white arrows the magnetisation direction.

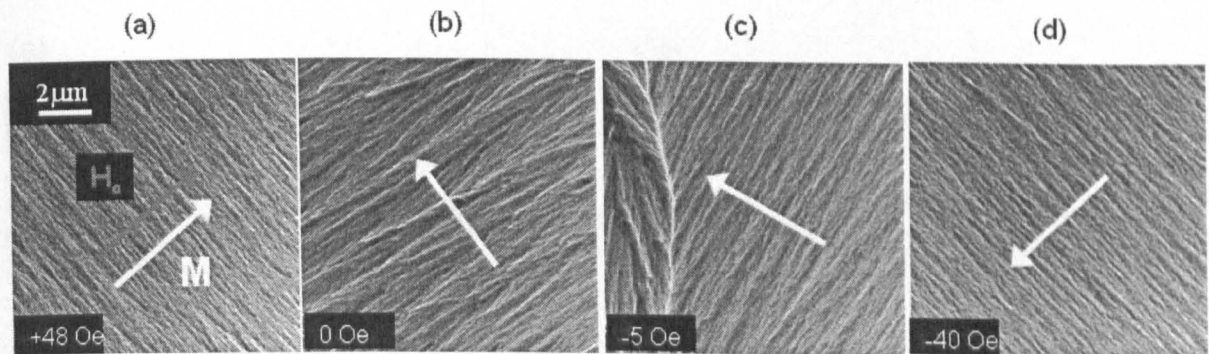


Figure 4.8: Magnetisation reversal of M3, NiFe1nm/CoFe22.5nm/Al₂O₃1.5nm/NiFe1nm/CoFe22.5nm, 1° from the hard axis with red arrows indicating the direction of applied field and the white arrows the magnetisation direction.

The convergent domain wall image (the one that appears bright against the neutral background) is split in figure 4.7c. This is due to the layered structure and shows that there is a small displacement of the domain walls in the different layers; this has been seen before for Néel walls, the wall structure expected given the reduced thickness of the individual layers [6]. Figure 4.9 shows that the key to whether the Néel walls in the two layers are displaced or superposed depends on their chirality with respect to each other. In figure 4.9a the walls have the same chirality and in figure 4.9b the walls have opposite chirality. Given that the walls were formed during a hard axis demagnetisation process, walls of the same chirality are expected with the magnetisation in the centre section of each wall lying parallel to the initial applied field. Under these conditions wall displacement leads to a lowering of energy in that magnetic charges of the same sign are no longer directly above each other [6]. Had the walls had different chiralities, superimposed walls would have been expected as here charges of opposite sign in the two layers align closely. The fact that splitting is not observed in divergent domain wall images at the defocus value used is simply a consequence of the greater width of the wall image [7]. By changing from underfocus to overfocus divergent wall images become convergent domain wall images and vice versa. In this way it can be shown that all walls formed during the hard axis demagnetisation are displaced from each other.

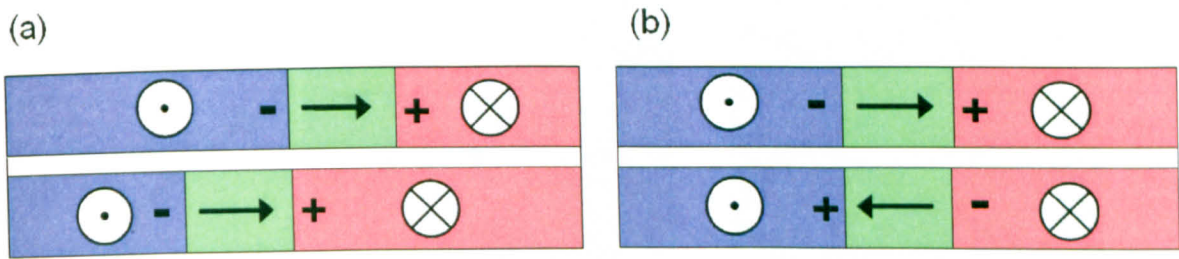


Figure 4.9: Schematic diagram showing (a) displaced and (b) superposed Néel walls.

4.5 Easy and hard axis reversal mechanism of the CoFe quadrilayer system

The final film to be studied was M4, NiFe/CoFe/(Al₂O₃/NiFe/CoFe)_{x3}. The easy axis reversal for the film is shown in figure 4.10. In a similar fashion to the previous film the magnetisation ripple contrast intensified as the switching field was approached and a highly mobile domain wall swept through effecting reversal at -2 Oe (figure 4.10d); subsequently there was a reduction in the ripple contrast. Figure 4.11 shows the application of the field along the hard axis of M4. In this case reversal proceeded entirely through magnetisation rotation. At zero field, the magnetisation had rotated through 90°, which is wholly consistent with the narrow B-H loop shown in figure 4.2d.

Whilst the behaviour described above was observed for most areas of this film, a small number of regions in these quadrilayer films showed markedly different behaviour during reversal. The images in figure 4.13 show a typical reversal with the field applied parallel to the easy axis in one of these regions. A complex domain structure formed and its occurrence in the same location on repeating the magnetisation cycle suggested some kind of defect must be present. However, standard bright field images, which reveal the crystallite structure, taken from regions where the anomalous magnetic behaviour was observed were indistinguishable from the rest of the film (figure 4.12).

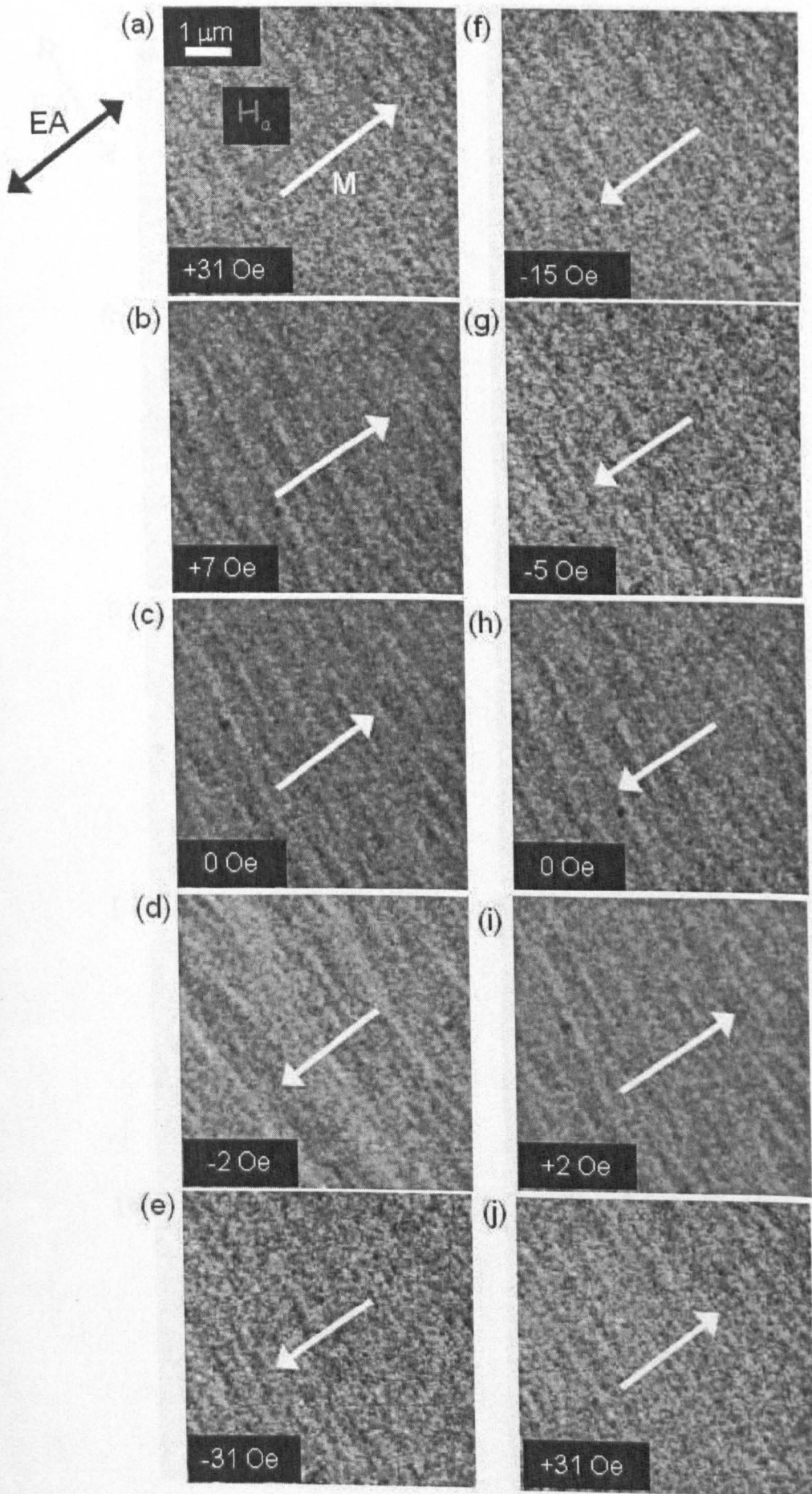


Figure 4.10: Easy axis magnetisation reversal of film M4, NiFe1nm/CoFe10nm/(Al₂O₃1.5nm/NiFe1nm/CoFe10nm)x3, with red arrows indicating the direction of applied field and the white arrows the magnetisation direction.

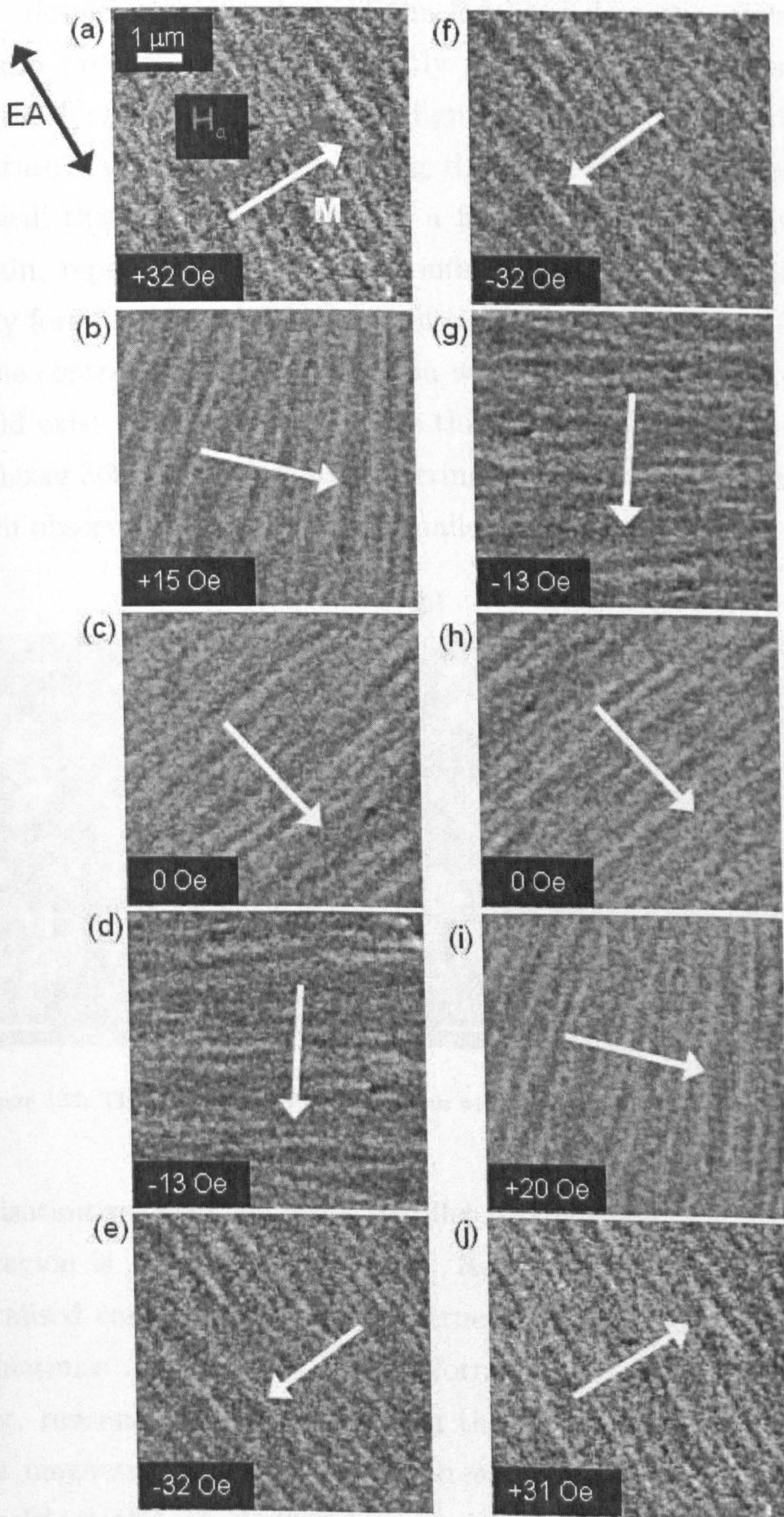


Figure 4.11: Hard axis magnetisation reversal of M4, NiFe1nm/CoFe10nm/(Al₂O₃1.5nm/NiFe1nm/CoFe10nm)x3, with red arrows indicating the direction of applied field and the white arrows the magnetisation direction.

Moreover, despite the formation of the localised domains, reversal occurred as in previous cases by a highly mobile domain wall sweeping through the film at a field ≈ -3 Oe (figure 4.13c-d). One further unusual feature was observed, this being the formation of a zigzag 360° domain wall that was annihilated by a field of $+30$ Oe (figure 4.13i). Once again, repetition of the cycle confirmed that 360° domain walls frequently formed close to the region of anomalous behaviour. Comparison of the contrast of the 360° domain wall with other walls suggested that it did exist throughout the whole thickness of the laminate. Quite similar zigzag 360° domain walls occurring at specific sites within a film have been observed previously in permalloy multilayer films [6].

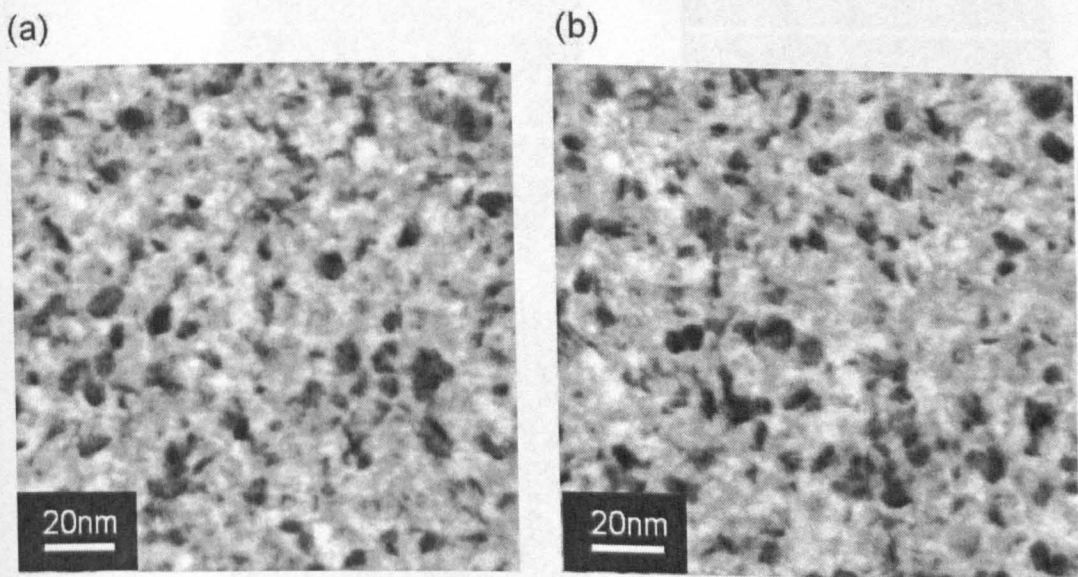


Figure 4.12: TEM images of M4 (a) at a region without a defect (b) at defect region

Magnetisation reversal for fields parallel to the hard axis at the same defect region is shown in figure 4.14. Here, the formation once again of a localised complex domain wall structure was observed; again this was sometimes accompanied by the formation of 360° domain walls. However, reversal a few microns from the defect region was primarily through magnetisation rotation. Figures 4.14f-j show the return path was consistent with the outward reversal.

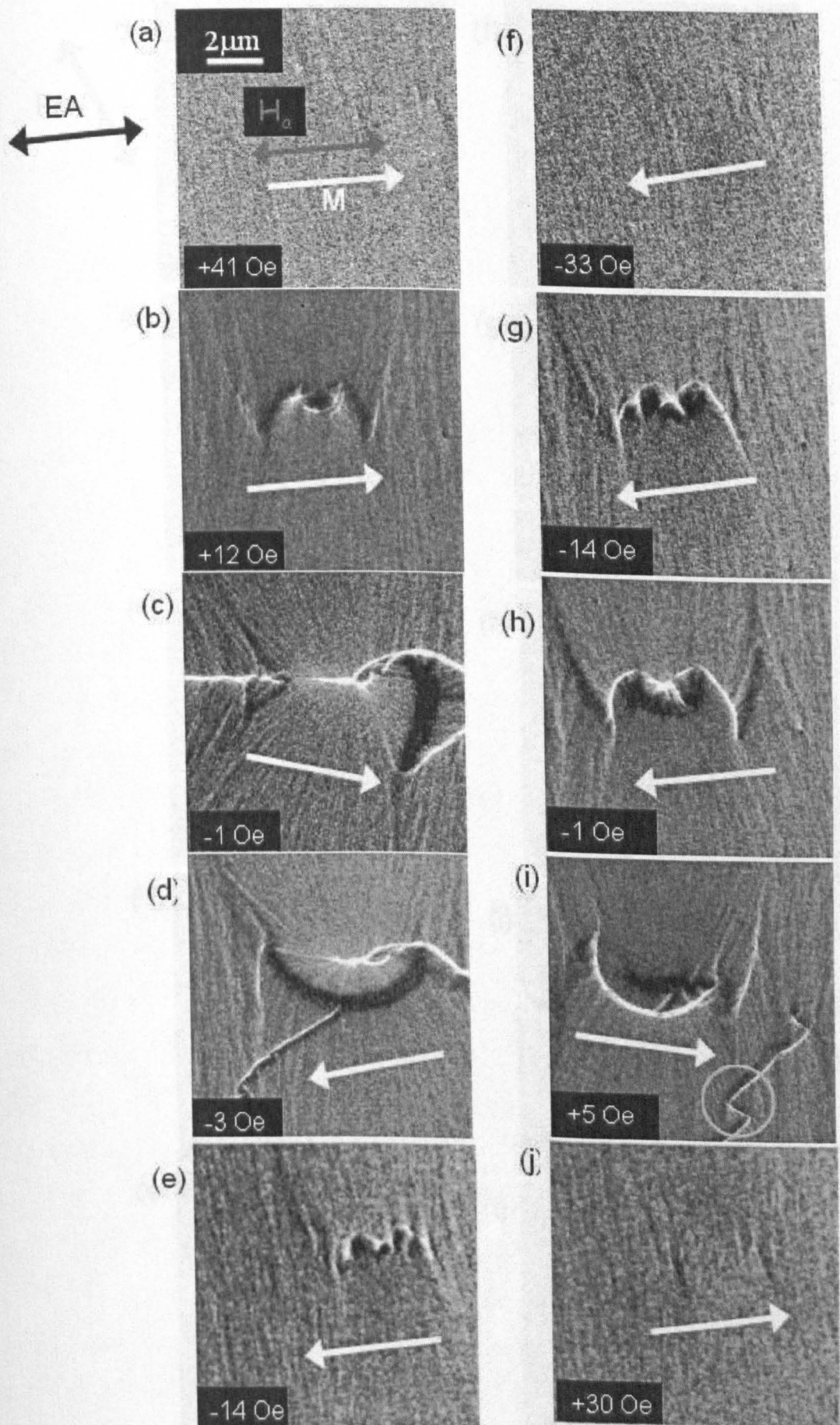


Figure 4.13: Easy axis magnetisation reversal of M4, NiFe1nm/CoFe10nm/(Al₂O₃1.5nm/NiFe1nm/CoFe10nm)x3, at a defect region with red arrows indicating the direction of applied field and the white arrows the magnetisation direction. The green circle indicates a 360° domain wall.

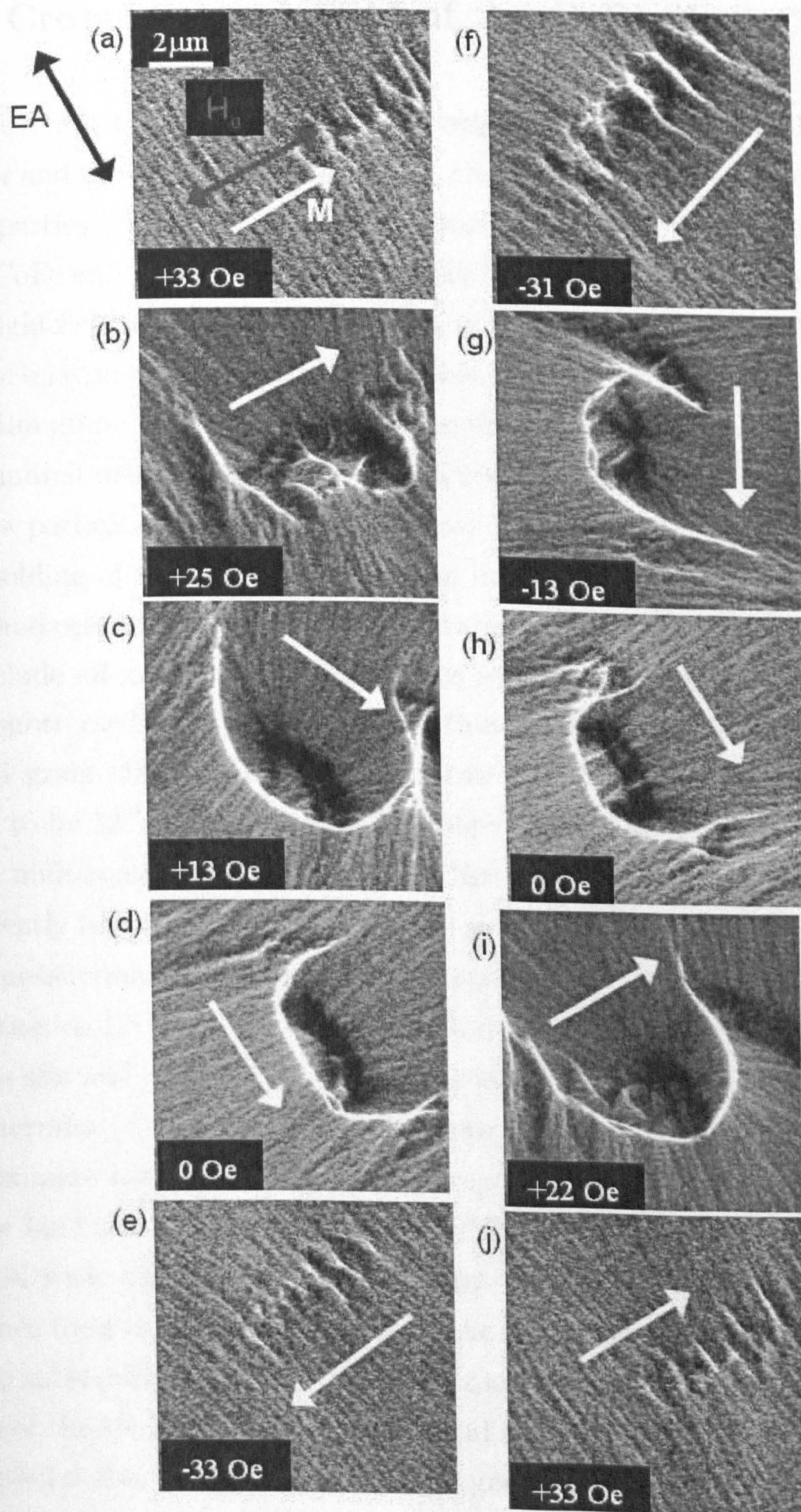


Figure 4.14: Hard axis magnetisation reversal of M4, NiFe1nm/CoFe10nm/(Al₂O₃1.5nm/NiFe1nm/CoFe10nm)x3, at a defect region with red arrows indicating the direction of applied field and the white arrows the magnetisation direction.

4.6 Cross-sectional TEM of the CoFe films

In an attempt to gain insight into the origin of both the anomalous behaviour and the reason why, that aside, there was a general improvement of properties with increasing lamination, cross-sectional specimens of NiFe/CoFe and NiFe/CoFe/(Al₂O₃/NiFe/CoFe)_{x3} were prepared. Typical bright field images are shown in figure 4.15. Columnar growth within the CoFe layers is observed in both cases. For the single layer with seed layer film grains tended to extend throughout the entire thickness. Over five hundred measurements were taken and the grain size calculated using the particle sizing facility in Digital MicrographTM. This requires thresholding of the contrast within the image which is a matter judgement and optimum levels for smaller grains differ from the larger grains. To include all grains the threshold was set for larger grains then these were subtracted from the image and thresholding was set again and a second grain size measurement performed. The mean grain size was found to be 12.5 nm with a standard deviation of 2.8 nm. By contrast, in the multilayer the location of grain boundaries in different layers was apparently uncorrelated, and the mean grain size (again calculated from fifty measurements) was significantly smaller at 7.9 nm with standard deviation of 1.5 nm. The exact distribution of the grain sizes depends on the size and distribution of the bins [8], therefore, it is often difficult to determine, although, the results were not in disagreement with the approximate log-normal distribution reported by Vopsaroiu et al. [9]. In the laminated film the roughness of the spacer layers noticeably increased with distance from the substrate. Forty measurements of the distance from the boundary region of the spacer layer to a reference line at the substrate were made. From the measurements the rms roughness value of the third spacer layer was found to be 0.9 nm with a maximum value ≈ 1.6 nm. This is significantly greater than the rms roughness value of 0.3 nm of the first spacer layer with maximum values ≈ 0.6 nm. Earlier studies on Fe-Cr superlattices showed a similar scaling of rough-

ness and established that it is strongly affected by the growth conditions [10, 11]. The implications of the increase in roughness are discussed in the following section.

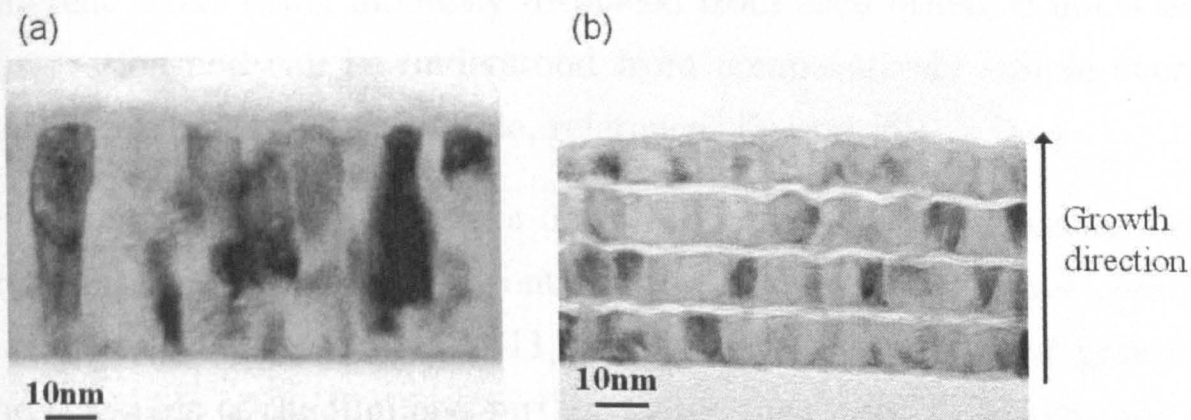


Figure 4.15: Bright field TEM image of (a) NiFe10nm/CoFe500nm and (b) NiFe10nm/CoFe100nm/(Al₂O₃15nm/NiFe10nm/CoFe100nm)_{x3}

4.7 Discussion

The Fresnel mode of Lorentz microscopy provides a detailed description of the magnetisation processes occurring during the reversal of four different CoFe thin films. Furthermore it has been shown how the various reversal mechanisms are consistent with the different shapes observed in the hysteresis loops from B-H loop measurements.

Quite different magnetisation distributions in single layer films with and without a seedlayer were observed emphasising once again the importance of the seedlayer if films with a well defined anisotropy axis and comparatively low coercivities are required. Indeed, our results on single layer films are qualitatively consistent with those discussed at some length in section 4. The measured grain size of the NiFe/CoFe film was 12.5 nm whilst H_c was 17 Oe. This is in very good agreement with the results of Vopsaroiu et al. [9], who found that films with a mean grain size less than 15 nm had coercivities of 25 Oe or below.

The move to multilayer films led to an overall improvement in the shape of the hysteresis loops and, aside from the anomalous regions of figures

4.13 and 4.14, this was accompanied by generally simpler and more regular magnetisation distributions evolving during the observed reversals. That different wall types were observed, with in some cases walls in different layers being modestly displaced from each other, is not a new observation and can be understood from comparatively simple energy considerations (see, for example, references [5] and [6]).

The laminated films are superior on two counts. They have smaller mean crystallite sizes which is one contributing factor to their lower coercivities. However, as equation 1.11 makes clear, the number of grains in the thickness of the film is a further factor that must be taken into account. Figure 4.15 shows that the position and orientation of crystallites in individual layers are uncorrelated and the effect of this is to lower the effective value of the local anisotropy, whether its source is magnetocrystalline or magnetostrictive. Again with reference to equation 1.11, K_{local} is replaced by $K_{local}/n^{1/2}$ so that when this and the lower grain size are taken into account we expect that the coercivity of the NiFe/CoFe/(Al₂O₃/NiFe/CoFe)x3 film, when compared to that of the NiFe/CoFe film, will be lower by a factor of $(7.9/12.5)^{3/2}/2 \approx 4$. This is in very reasonable agreement with experiment where the coercivities of the two films are ≈ 17 Oe and ≈ 3 Oe respectively. It should be noted that the good agreement with the Hoffmann theory does not imply that the random anisotropy model is incorrect. The data are too sparse for a detailed comparison to be made and in any event the main focus of this study is to gain insight into microscopic magnetisation processes, not to compare different models of the coercivity.

A minor disadvantage of increasing the number of layers is that the moment of the film decreases as a greater proportion of the volume is occupied by the spacer layers. More serious, however, is the introduction of localised magnetic behaviour of the kind seen in figures 4.13 and 4.14. Whilst such regions occupied a very small fraction of the total film volume and, as such, were undetectable in the hysteresis loops, their effect

would be very marked in any device that contained such defective material. The cross-sectional images of figure 4.15 offer clues as to how the anomalous behaviour arises and suggest that the effects are likely to be confined to the upper layers where the roughness is greatest. It is clear that there is little local variation in the thickness of the spacer layers so that the top surface of one magnetic layer and the bottom surface of the layer immediately above have very similar profiles. With such conformal roughness Néel coupling between the layers is expected, the coupling field H_n being given by [12, 13]

$$H_n = \frac{\pi^2}{\sqrt{2} t_{CoFe} \lambda} \frac{h^2}{M_s} \exp\left(\frac{-2\pi\sqrt{2}t_{spacer}}{\lambda}\right) \quad (4.1)$$

Here λ and h are the lateral length scale and the amplitude of the roughness, t_{spacer} and t_{CoFe} are the thicknesses of the spacer and CoFe layers and M_s is the saturation magnetisation. Here the major contributing factor is the magnetostatic energy. Examination of figure 4.15 suggests that the lateral variation is on the scale of the crystallite diameter so λ can be taken as the mean grain size. For $\mu_0 M_s \approx 2.4T$ and the rms roughness values given previously, H_n at the third spacer layer is ≈ 100 Oe which is an order of magnitude greater than the value of ≈ 11 Oe at the first spacer layer. The coupling between the layers, even across the first interface, is hence considerably greater than the observed switching fields and is consistent with the observation that the layers reverse together. Moreover, significantly greater fields than 100 Oe can be expected where the local roughness is greatest and it is highly possible that these provide the necessary stabilisation of the complex magnetic structures observed in figure 4.13.

To investigate the complex reversal mechanisms observed in the laminate films, further multilayer films were deposited. The effect of varying the CoFe layer thickness and of lowering the spacer layer thickness to 1.25 nm has been investigated through Lorentz microscopy and conventional

TEM and is discussed in chapter 5.

Bibliography

- [1] B. Khameshpour, C. D. Wilkinson, J. N. Chapman, and A. B. Johnston, *J. Vac. Sci. Technol. B* **14** (5), 3361 (1996).
- [2] V. A. Vas'ko *et al.*, *J. Appl. Phys.* **91**, 6818 (2002).
- [3] H. S. Jung, W. D. Doyle, and S. Matsunama, *J. Appl. Phys.* **93**, 6462 (2003).
- [4] A. Gentils, J. N. Chapman, G. Xiong, and R. P. Cowburn, *J. Appl. Phys.* **98**, 053905 (2005).
- [5] J. E. E. Huber, D. O. Smith, and J. R. Goodenough, *J. Appl. Phys.* **29**, 294 (1958).
- [6] I. B. Puchalska and H. Niedoba, *IEEE Trans. Magn.* **27** (4), 3579 (1991).
- [7] R. H. Wade, *Proc. Phys. Soc.* **79**, 1237 (1962).
- [8] D. W. Park, R. Sinclair, B. B. Lal, S. Malhotia, and M. A. Russak, *J. Appl. Phys.* **87**, 5687 (2000).
- [9] M. Vopsaroiu *et al.*, *J. Appl. Phys.* **97**, 10N303 (2005).
- [10] M. E. Gomez *et al.*, *Eur. Phys. J. B* **30**, 17 (2002).
- [11] J. Santamaria, M. E. Gomez, J. L. Vicent, K. M. Krishnan, and I. K. Schuller, *Phys. Rev. Lett.* **89**, 19061 (2002).
- [12] J. C. S. Kools, *J. Appl. Phys.* **77**, 2993 (1995).

- [13] J. C. S. Kools, T. G. S. M. Rijks, A. E. M. D. Veirman, and R. Coehoorn, *IEEE Trans. Magn.* **31**, 3918 (1995).

Chapter 5

Investigation of 360° domain walls in CoFe multilayer films

5.1 Introduction

To investigate the origin of the complex domain walls previously found in sample M4 (section 4.5) further samples were deposited under the same deposition conditions described in chapter 4. Lorentz microscopy was carried out to investigate the magnetic microstructure of the films and their reversal behaviour. The films have been studied with Fresnel imaging, DPC imaging, conventional TEM and EELS with the aim of gaining a greater understanding of the origin and stability of the complex domain walls.

The main difference between the film structures and sample M4 was a reduction in the Al_2O_3 layer thickness from 1.5 nm to 1.25 nm. To establish whether the CoFe thickness had an influence on the presence of the defect regions, laminated films with 5 nm, 10 nm and 22.5 nm CoFe layers were deposited. A bilayer film with 10 nm thick CoFe layers was also deposited to establish whether the defect regions were only present in the quadrilayer samples. The film structures are detailed in figure 5.1 and table 5.1.

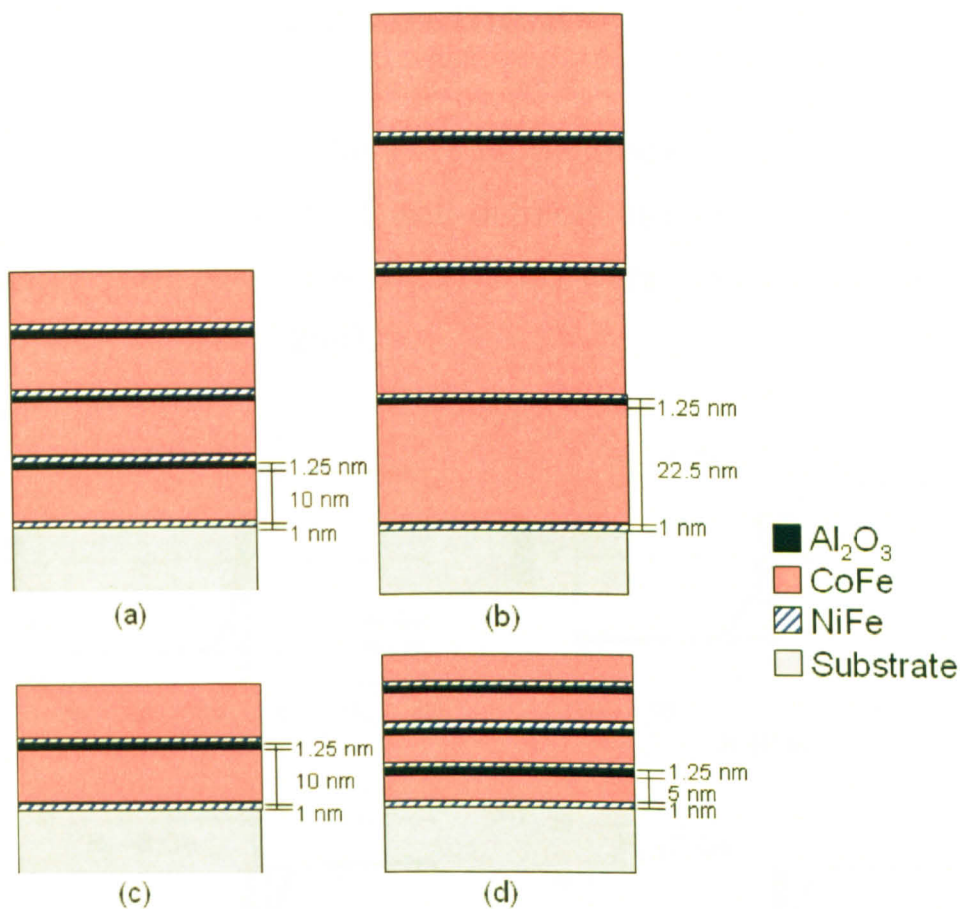


Figure 5.1: Schematic illustration of (a) M5, (b) M6, (c) M7 and (d) M8

Film name	Total t (nm)	CoFe t (nm)	Number of CoFe layers	Total number of layers
M5	47.75	10	4	11
M6	87.75	22.5	4	11
M7	23.25	10	2	5
M8	27.75	5	4	11

Table 5.1: Description of samples M5, M6, M7 and M8. All four films have a 1 nm NiFe seed layer and 1.25 nm Al₂O₃ spacer layer.

5.2 B-H looper measurements

The hysteresis loops from the B-H looper measurements are shown in figure 5.2. All four films had well-defined uniaxial hysteresis loops of similar shape. The easy axis coercivities were 4 Oe, 4 Oe, 6 Oe and 3 Oe respectively, figures 5.2a-d.

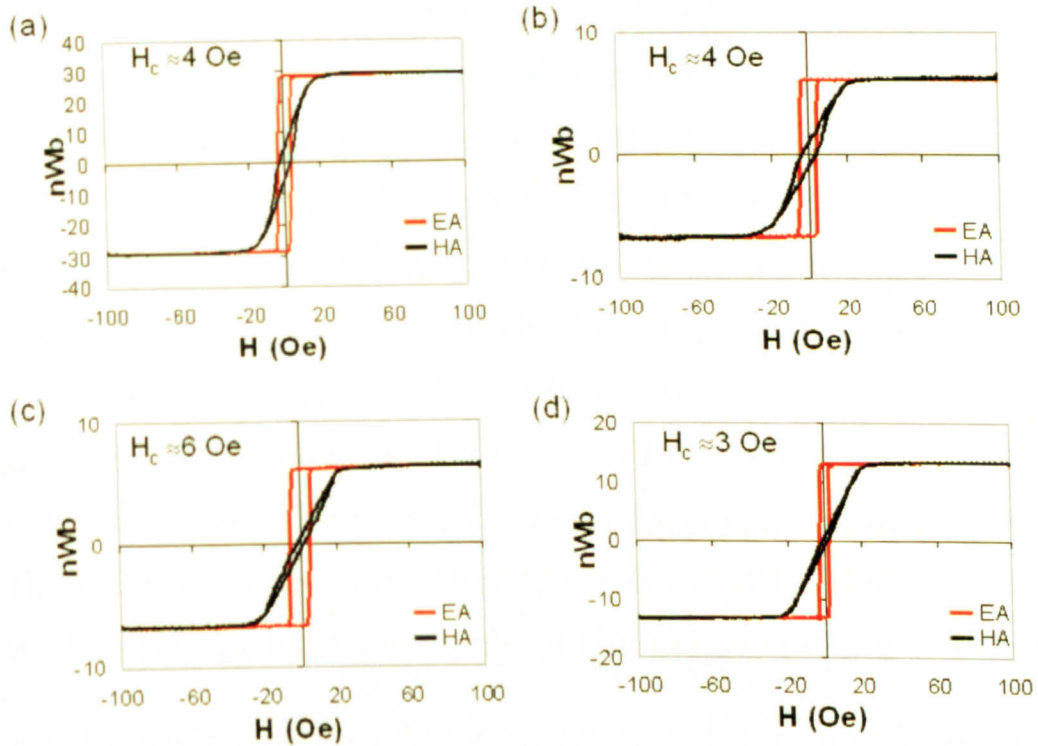


Figure 5.2: Easy and Hard axis B-H loops for (a) M5, (b) M6, (c) M7 and (d) M8

5.3 Observation of stable 360° domain walls

A high density of structural defects, different from the magnetic defects observed in the quadrilayer film in chapter 4, were observed in three of the films. These defects had a significant influence on the magnetisation reversal and are discussed later in this section. 360° domain walls, which persisted to high fields, formed in all the films. In a continuous film the existence of 360° domain walls does not have significant implications if present in a device such as a recording head the performance would be significantly hampered. That the 360° are of finite length is down to pinning by some inhomogeneity and investigations into the end points

of the walls is carried out later in this chapter and chapter 6. To establish how the 360° domain walls form, a full reversal of the bilayer film, M7, from a state without any 360° domain walls is presented initially. Thereafter typical reversal sequences along the easy and hard axis of the four films over a field range of $\sim \pm 10 H_c$, where H_c is the coercivity, are given.

Figure 5.3 shows the outward part of an easy axis reversal of M7 followed by images taken at the end points of repeated magnetisation cycles. A field > 700 Oe was applied to the film to wipe out the 360° domain walls (figure 5.3a). During the initial part of the reversal the ripple intensified as expected (figure 5.3a-c). A highly mobile domain wall, not captured on the CCD camera, swept through effecting reversal and 360° domain walls formed. An image at -7 Oe after reversal has occurred is shown in figure 5.3e. On repeating the reversal to ± 46 Oe 360° domain walls frequently remained. Figures 5.3e-o show the end points of the reversal with the coloured ovals indicating examples of 360° domain walls which remained during at least one cycle of the magnetisation reversal.

Further discussion of film M7 is presented later in this section. The results from film M5 will be presented now as this film more closely resembles the laminated film in chapter 4 which initiated this study.

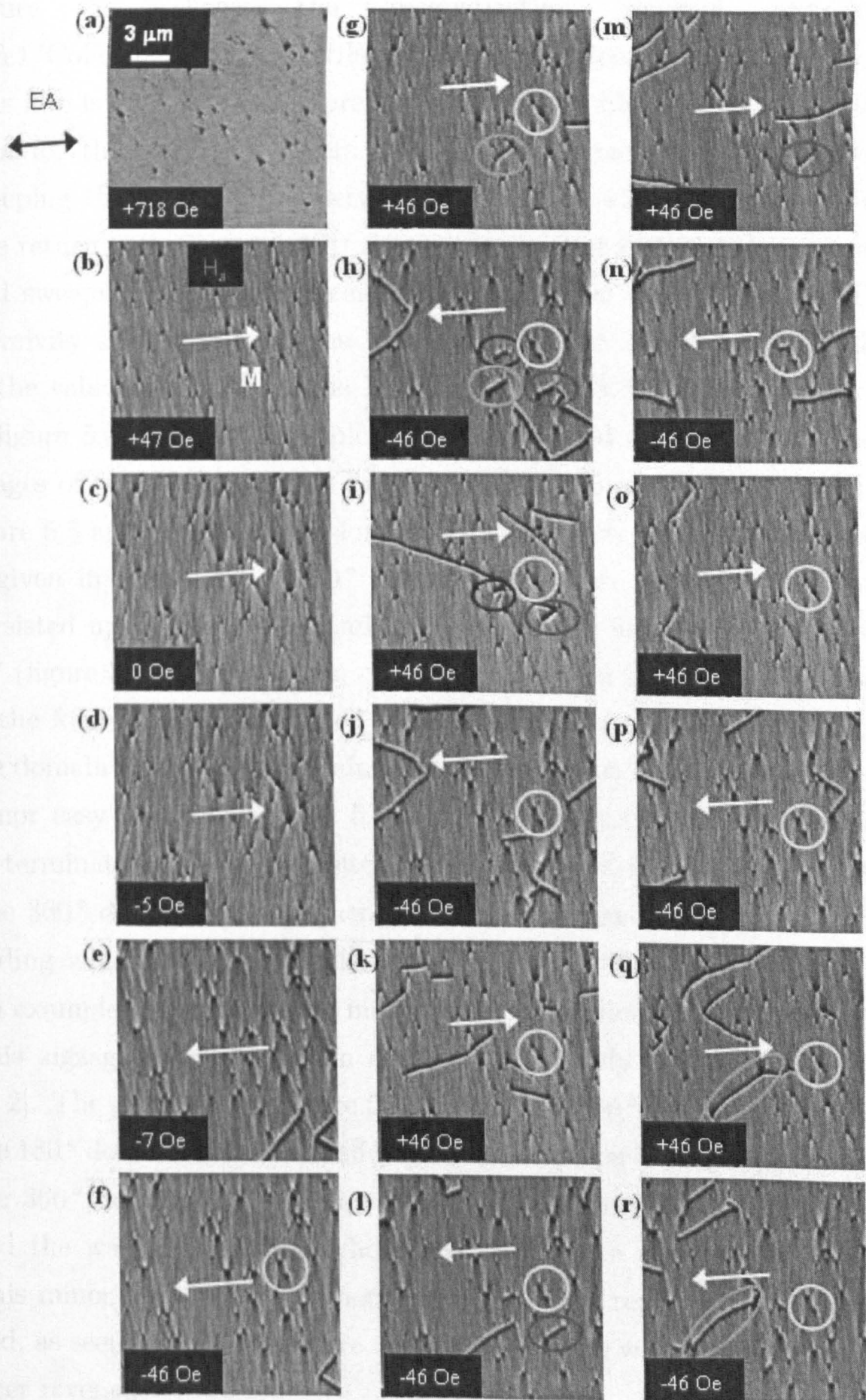


Figure 5.3: Easy axis magnetisation reversal of M7, NiFe1nm/CoFe10nm/Al₂O₃1.5nm/NiFe1nm/CoFe10nm, showing repeated end points of a magnetisation cycle. Red arrows indicate the direction of applied field and the white arrows the magnetisation direction. The coloured ovals highlight 360° domain walls which remain throughout at least one cycle of reversal.

Figure 5.4 shows the magnetisation reversal of M5, NiFe1/CoFe10/(Al₂O₃1.25/NiFe1/CoFe10)x3, close to the easy axis. This film is the same as the previous quadrilayer film in chapter 4 other than for thinner Al₂O₃ layers. Reversal occurred by a domain wall sweeping through the film between +2 Oe and +3 Oe (figure 5.4d-e). The return path (figure 5.4f-j) showed similar behaviour with a domain wall sweeping through between -2 Oe and -3 Oe (figure 5.4h-i). The coercivity suggested from the images is 2-3 Oe which is comparable to the value of 3 Oe from the B-H loop (figure 5.2a). The blue circles in figure 5.4a indicate examples of the structural defects. Bright field images of typical defect sites present in films M5 and M7 are shown in figure 5.5 and further discussion of the physical structure of the defects is given in section 5.5. 360° domain walls were observed and these persisted up to high fields similar to those seen in the reversal of film M7 (figure 5.3). Minor loops, not starting from a fully saturated state, of the four films are presented to investigate the reversal behaviour of the domain walls. 360° domain walls were present from the start of the minor easy axis loop (figure 5.4a). Some of the domain walls appear to terminate at the defect sites although this is not always the case. The 360° domain walls aligned with the hard axis often have a zigzag folding which concurs with the observations in film M4 (section 4.5). An example of such a wall is indicated by the yellow oval in figure 5.4b. This zigzag folding has been observed previously for permalloy films [1, 2]. The green oval in figure 5.4c indicates a 360° domain wall. When the 180° domain wall which effects reversal sweeps through (figure 5.4d) the 360° domain wall is not annihilated, but the contrast is reversed and the wall persists throughout the rest of the magnetisation cycle. This minor loop of the magnetisation cycle was repeated several times and, as seen in film M7 (figure 5.3), 360° domain walls always remained after reversal.

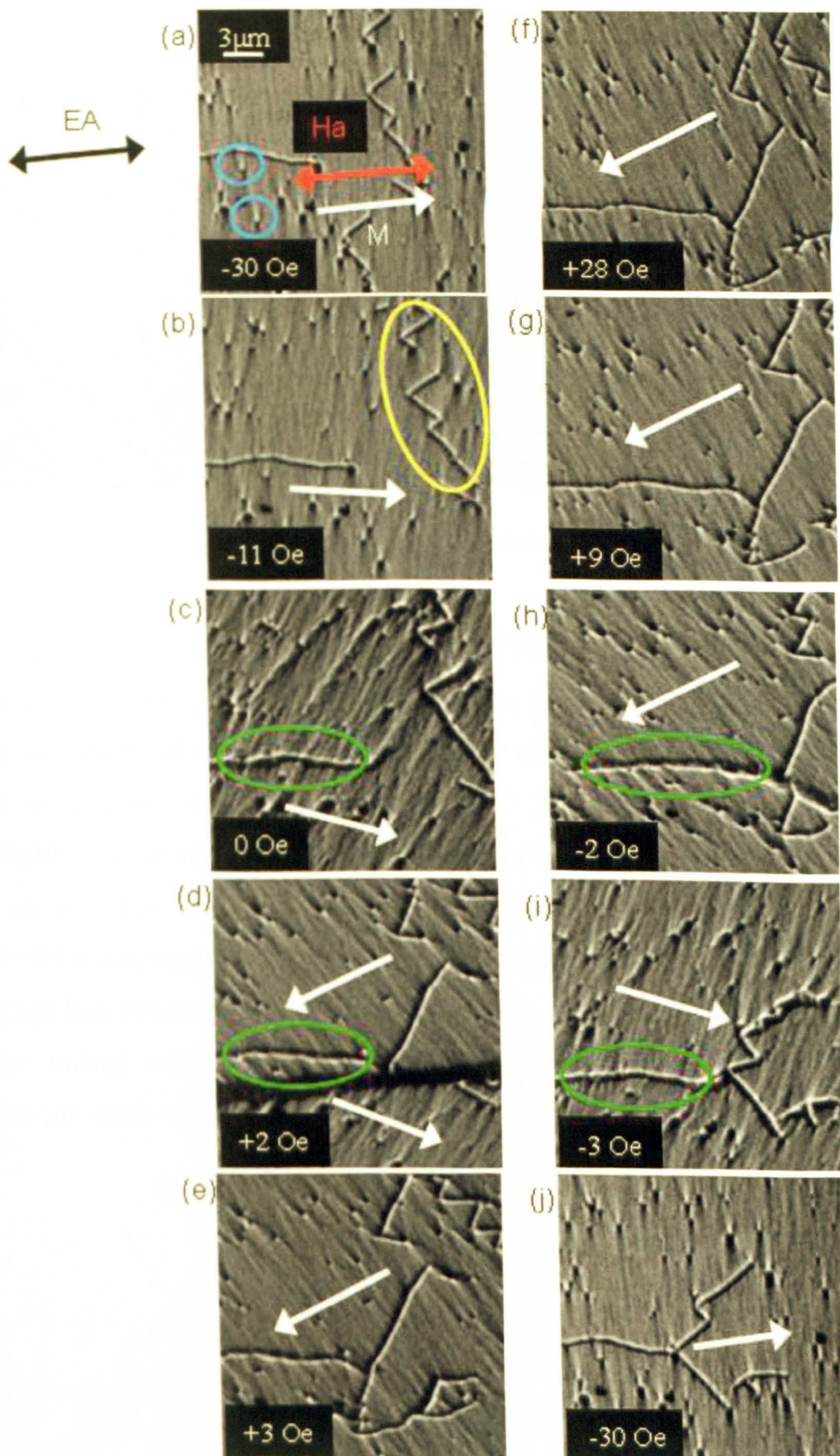


Figure 5.4: Easy axis magnetisation reversal of M5, NiFe1nm/CoFe10nm/(Al₂O₃1.5nm/NiFe1nm/CoFe10nm) \times 3 with red arrows indicating the direction of applied field and the white arrows the magnetisation direction. The green circles highlight a 360° domain wall which remains throughout reversal.

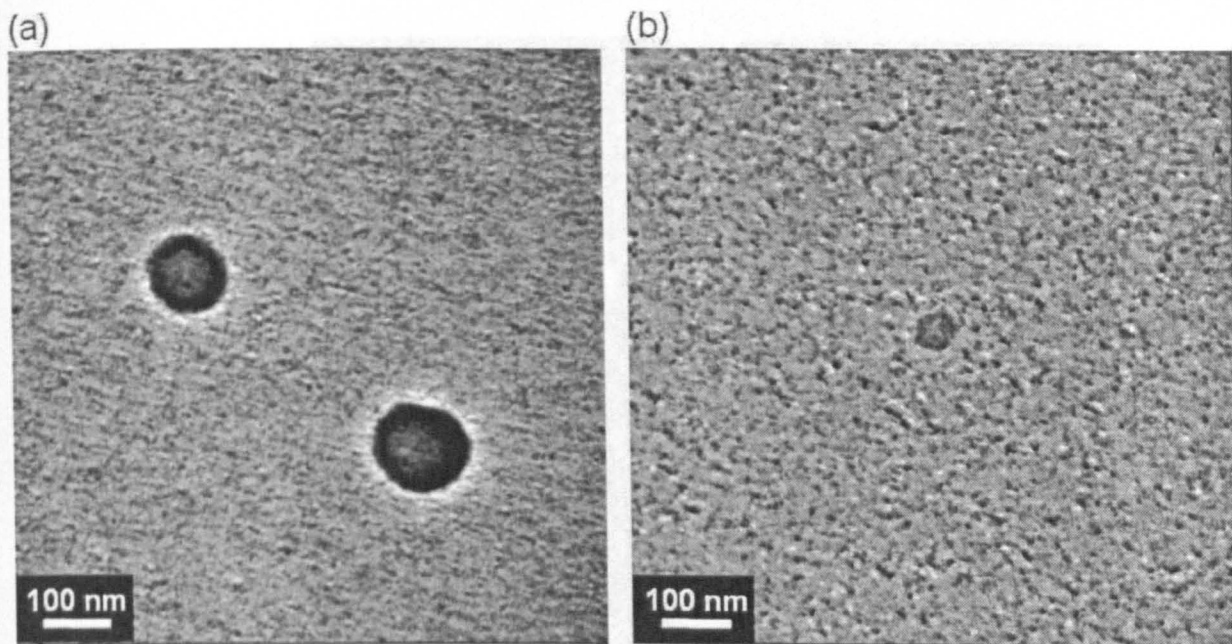


Figure 5.5: Bright field TEM images showing typical defect areas in films (a) M5 and (b) M7.

The hard axis magnetisation reversal of M5 is shown in figure 5.6. The reversal proceeded through magnetisation rotation as expected from the previous study of the quadrilayer film in chapter 4. Again 360° domain walls were observed during the reversal. The green ovals in figure 5.6 highlight two of the 360° domain walls. During the reversal the walls take on a zigzag folding as the magnetisation aligns along the easy axis, i.e. at 0 Oe applied field (figure 5.6c). In figure 5.6d the 360° domain wall contrast has reversed, seen from the black contrast at the top compared to the initial white contrast at the top. The return path is entirely consistent with the outward reversal.

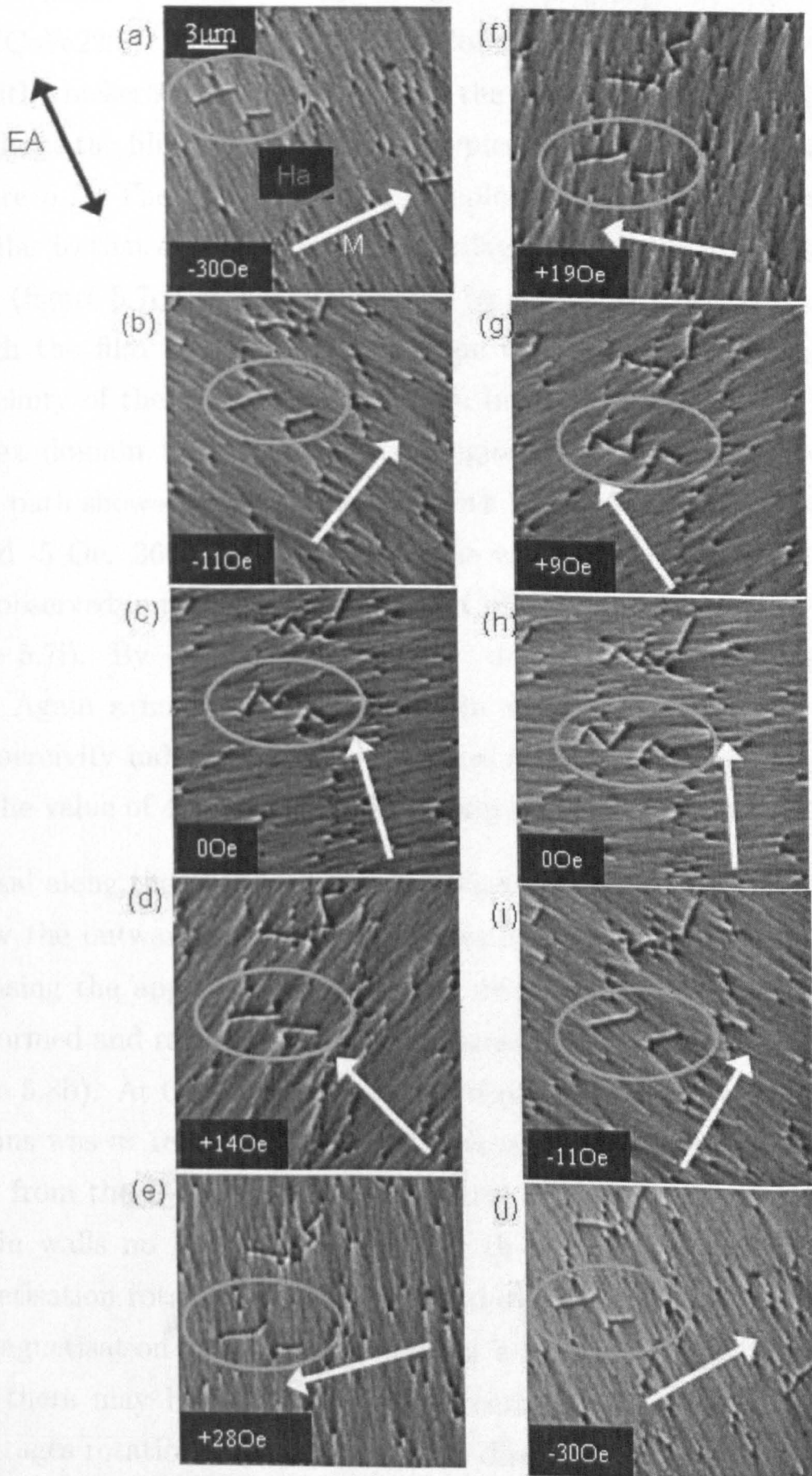


Figure 5.6: Hard axis magnetisation reversal of M5, NiFe1nm/CoFe10nm/(Al₂O₃1.5/NiFe1nm/CoFe10nm)x3 with red arrows indicating the direction of applied field and the white arrows the magnetisation direction. The green circles highlight a 360° domain wall which remains throughout reversal.

The next film to be studied was M6, NiFe1/CoFe22.5/(Al₂O₃1.25/NiFe1/ CoFe22.5)x3, i.e. a quadrilayer film with thicker CoFe layers. Again the presence of physical defects throughout the film was observed. A typical easy axis reversal is shown in figure 5.7. The formation of a complex domain wall structure not dissimilar to that observed in the quadrilayer film in chapter 4 is seen at +3 Oe (figure 5.7c). Reversal occurred by a 180° domain wall sweeping through the film at +5 Oe. The angle of the wall was disturbed in the vicinity of the defect region as seen in figure 5.7d. By +46 Oe the complex domain wall at the defect region no longer remained. The return path showed similar processes with reversal occurring between -3 Oe and -5 Oe. 360° domain walls some with zigzag folding, similar to those observed in the film with thinner CoFe layers formed after reversal (figure 5.7i). By -49 Oe very few 360° domain walls remained (figure 5.7j). Again a number of 360° domain walls formed during reversal. The coercivity indicated from the images is 4-5 Oe which is consistent with the value of 4 Oe from the B-H loop measurement (figure 5.2b).

Reversal along the hard axis of M6 is shown in figure 5.8. Figures 5.8a-e show the outward reversal and figures 5.8f-j the return reversal. On decreasing the applied field to -13 Oe domain walls orthogonal to the field formed and regions of differing magnetisation orientation were seen (figure 5.8b). At 0 Oe the orientation of magnetisation in neighbouring domains was $\approx 180^\circ$ (figure 5.8c). This suggests a narrower loop than found from the B-H loop measurements (figure 5.2b). At +7 Oe the domain walls no longer remained and the reversal continued through magnetisation rotation (figures 5.8d and e). The return path proceeded via magnetisation rotation. The modest asymmetry in the reversal suggests there may be some small unidirectional coupling present which encourages rotational behaviour in one direction.

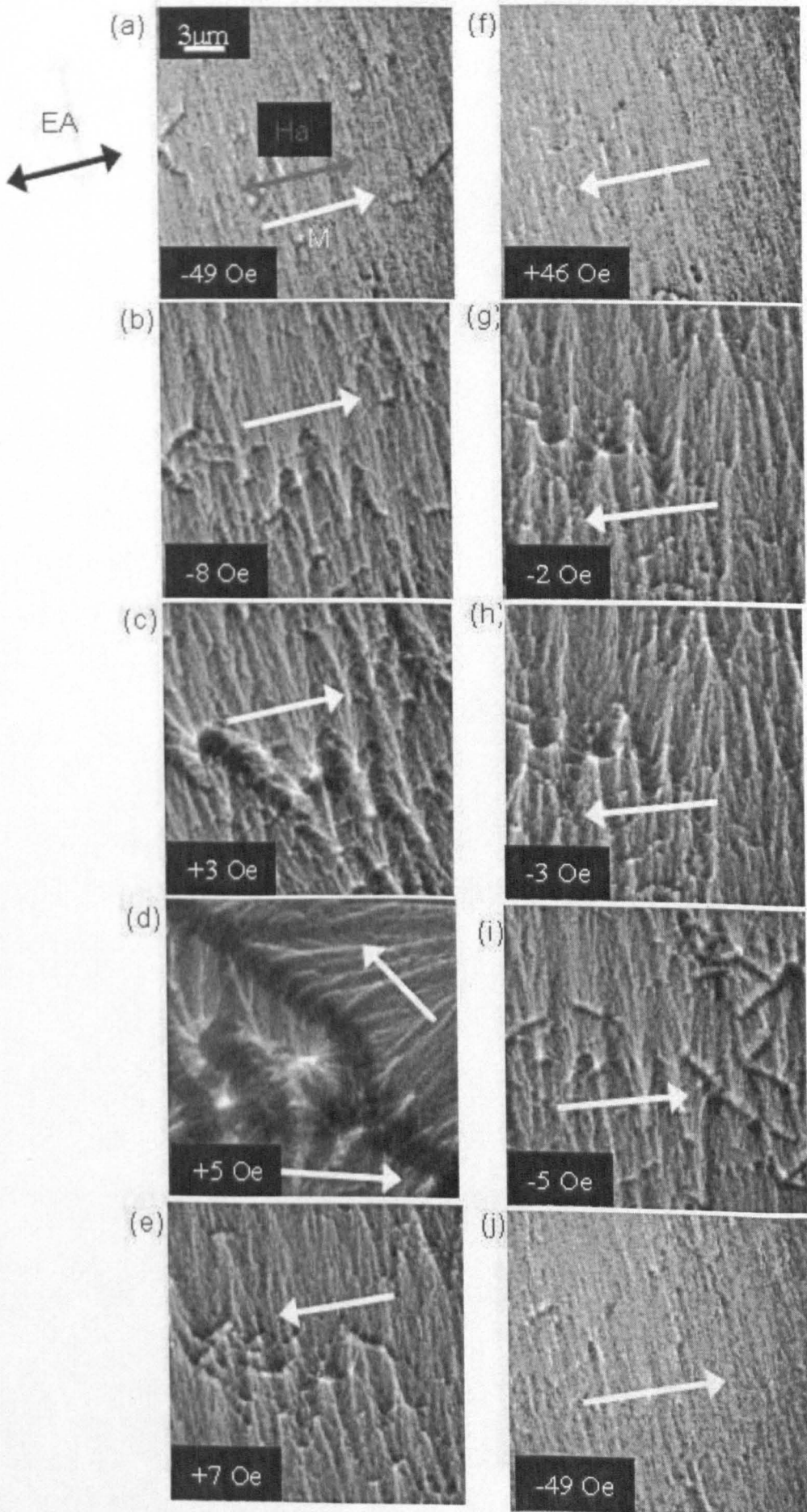


Figure 5.7: Easy axis magnetisation reversal of M6, NiFe1nm/CoFe22.5nm/(Al₂O₃1.5nm/NiFe1nm/CoFe22.5nm)x3 with red arrows indicating the direction of applied field and the white arrows the magnetisation direction.

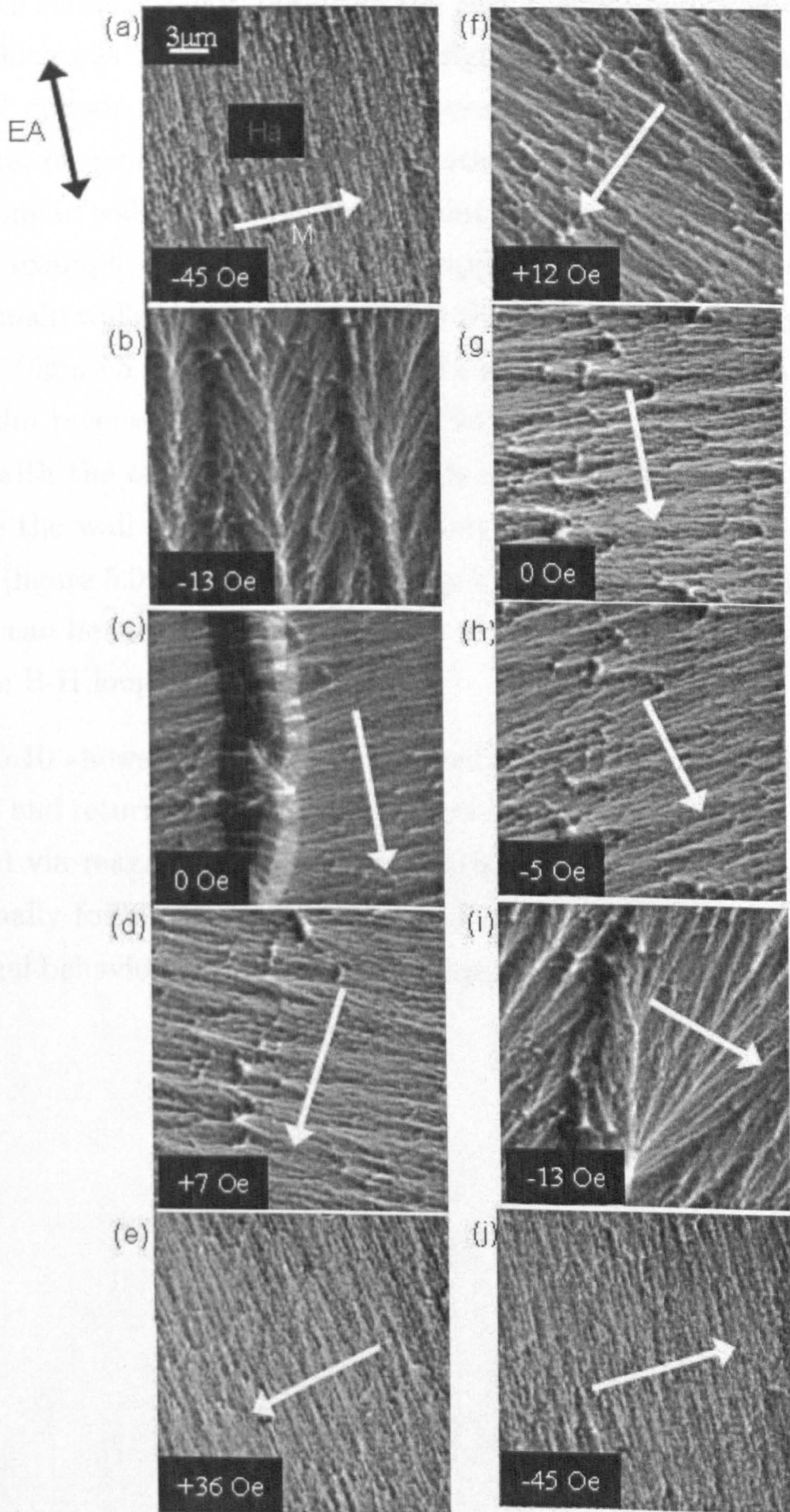


Figure 5.8: Hard axis magnetisation reversal of M6, NiFe1nm/CoFe22.5nm/(Al₂O₃1.5nm/NiFe1nm/CoFe22.5nm)x3 with red arrows indicating the direction of applied field and the white arrows the magnetisation direction.

Figure 5.9 shows a minor loop from the easy axis magnetisation reversal of M7 which was discussed previously (figure 5.3). As in the quadrilayer film 360° domain walls were initially present for the minor loop reversal. As before, on repetition of a magnetisation cycle, there were instances of the domain walls remaining throughout reversal. The green oval indicates an example of such a wall. The ripple intensified and some of the 360° domain walls began to separate as the field was taken from +46 Oe to -6 Oe (figure 5.9a-c). A domain wall swept through and the majority of the film reversed at -7 Oe (figure 5.9d). The return reversal is consistent with the outward reversal and is shown in figure 5.9f-j. In this instance the wall which effects the reversal was captured on the CCD camera (figure 5.9h) and the complexity of the domain structure during reversal can be seen. The images agree with the coercivity value of 6 Oe from the B-H loop (figure 5.2c).

Figure 5.10 shows the hard axis reversal of M7. The outward (figures 5.10a-e) and return (figures 5.10f-j) reversals were in agreement. Reversal occurred via magnetisation rotation with short lengths of domain wall occasionally forming between the defect sites, figures 5.10g and h. The rotational behaviour agrees with the shape of the B-H loop in figure 5.2c.

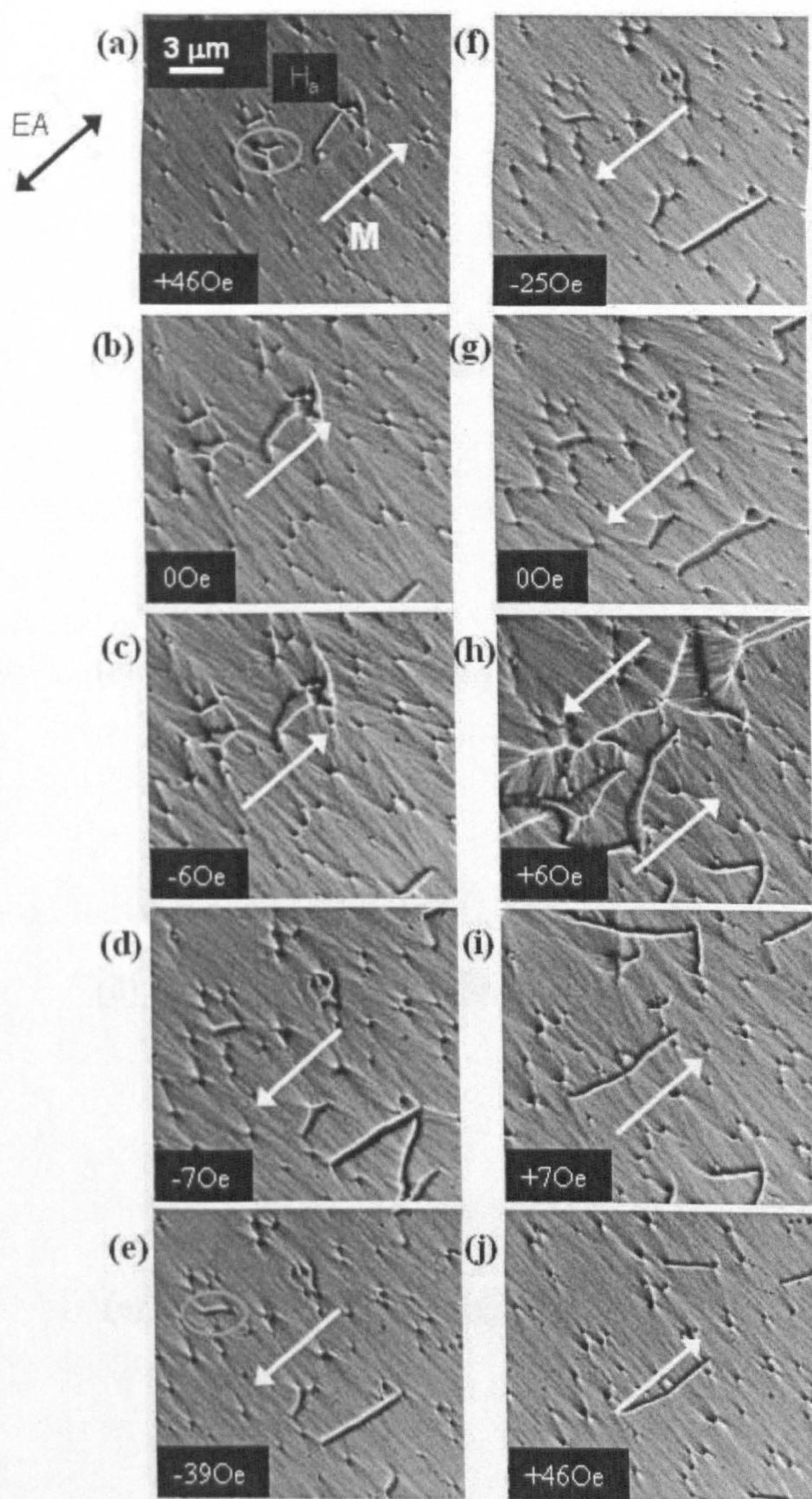


Figure 5.9: Easy axis magnetisation reversal of M7, NiFe1nm/CoFe10nm/Al₂O₃1.5nm/NiFe1nm/CoFe10nm, with red arrows indicating the direction of applied field and the white arrows the magnetisation direction. The green circles highlight a 360° domain wall which remains throughout reversal.

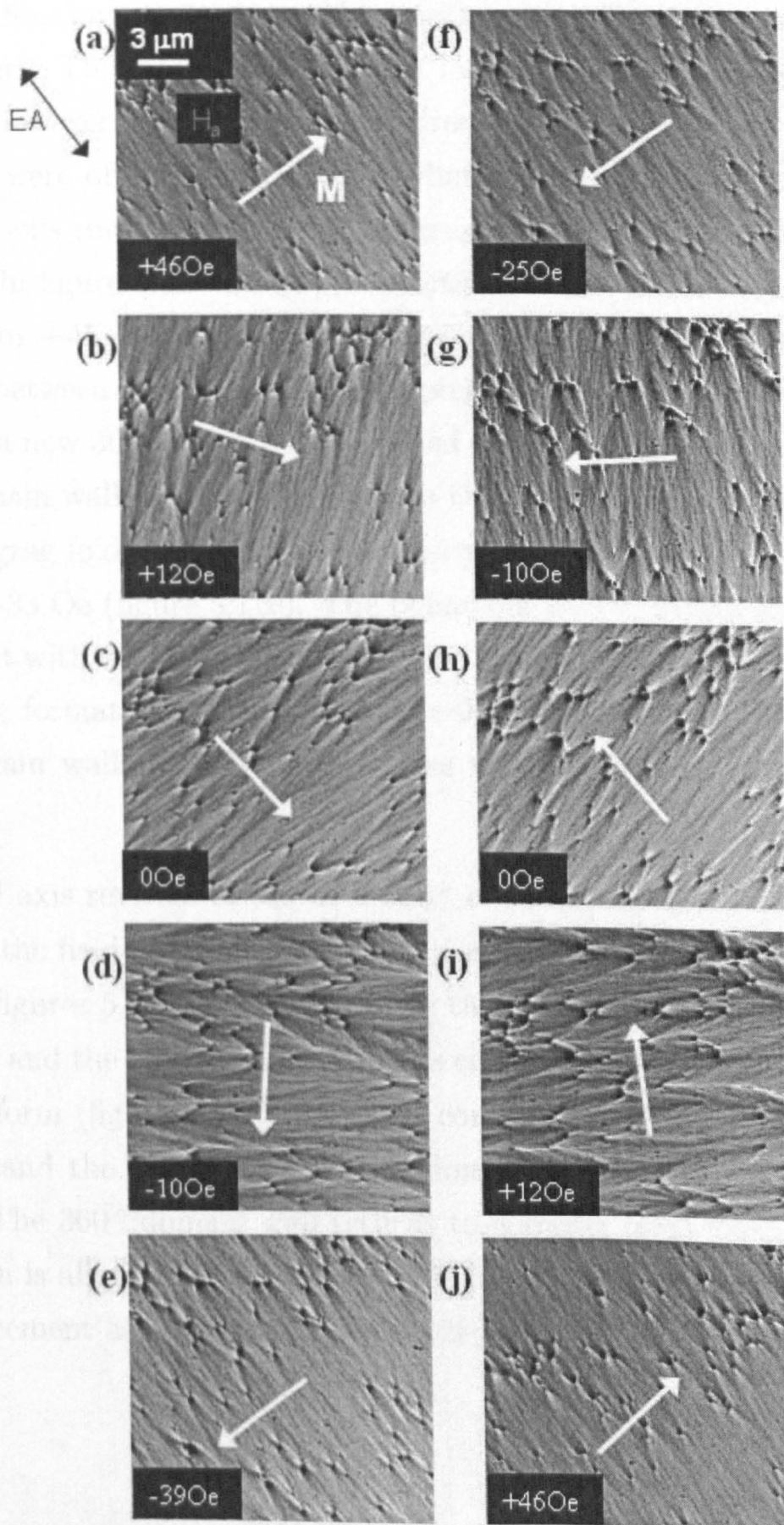


Figure 5.10: Hard axis magnetisation reversal of M7, NiFe1nm/CoFe10nm/ Al_2O_3 1.5nm/NiFe1nm/CoFe10nm with red arrows indicating the direction of applied field and the white arrows the magnetisation direction.

The final film investigated was M8, another quadrilayer film with 5 nm CoFe layers. The majority of the film looked clean without any defect regions. However, 360° domain walls frequently formed during reversal and they were often zigzag in form when aligned along the hard axis. The easy axis reversal with a 360° zigzag domain wall initially present is shown in figure 5.11. The ripple contrast intensified as the field was taken from +45 Oe to -1 Oe (figures 5.11a-c). A domain wall swept through between -1 Oe and -3 Oe wiping out the zigzag 360° domain wall and a new 360° domain wall formed (figure 5.11d). In this case the 360° domain wall was aligned closer to the easy axis, therefore, did not have a zigzag folding. The ripple intensity then reduced as the field was taken to -33 Oe (figure 5.11e). The behaviour shown in the images is in agreement with the shape of the B-H loop (figure 5.2d). The return path shows the formation of 360° domain walls after reversal (figure 5.11i). The domain walls in this case lie close to the easy axis and thus are straight.

The hard axis reversal of M8 at a 360° domain wall is shown in figure 5.12. As the field is reduced from +32 Oe to +10 Oe the magnetisation rotates (figures 5.12a and b). By 0 Oe the magnetisation lies along the easy axis and the 360° domain wall has changed from a zigzag form to a straight form (figure 5.12c). Reversal continues through magnetisation rotation and the magnetisation direction is reversed by -26 Oe (figure 5.12d). The 360° domain wall returns to a zigzag form when the magnetisation is aligned along the hard axis (figure 5.12e). The return path is in agreement as shown in figures 5.12f-j.

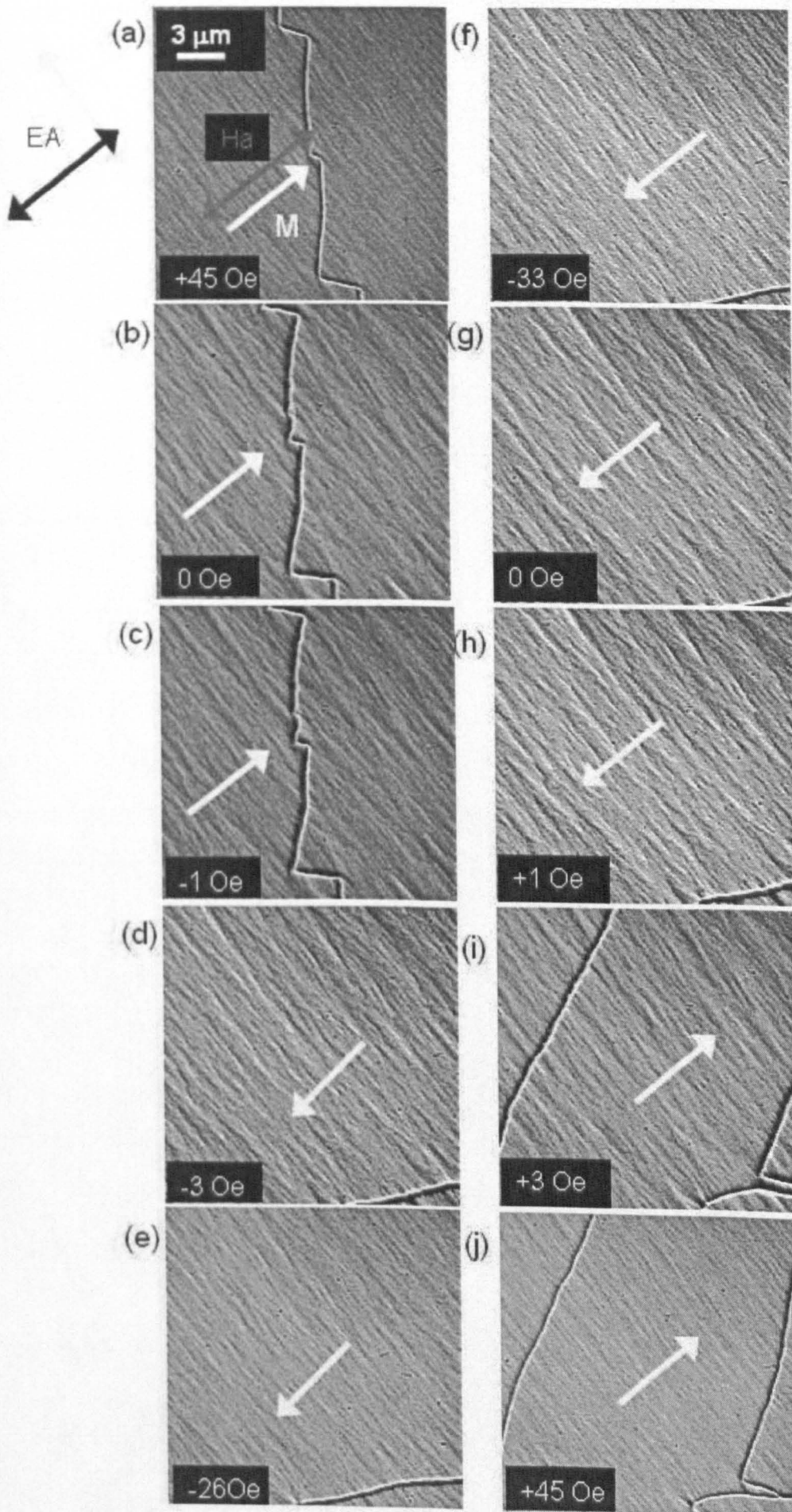


Figure 5.11: Easy axis magnetisation reversal of M8, NiFe1nm/CoFe5nm/(Al₂O₃1.5nm/NiFe1nm/CoFe5nm) \times 3 with red arrows indicating the direction of applied field and the white arrows the magnetisation direction.

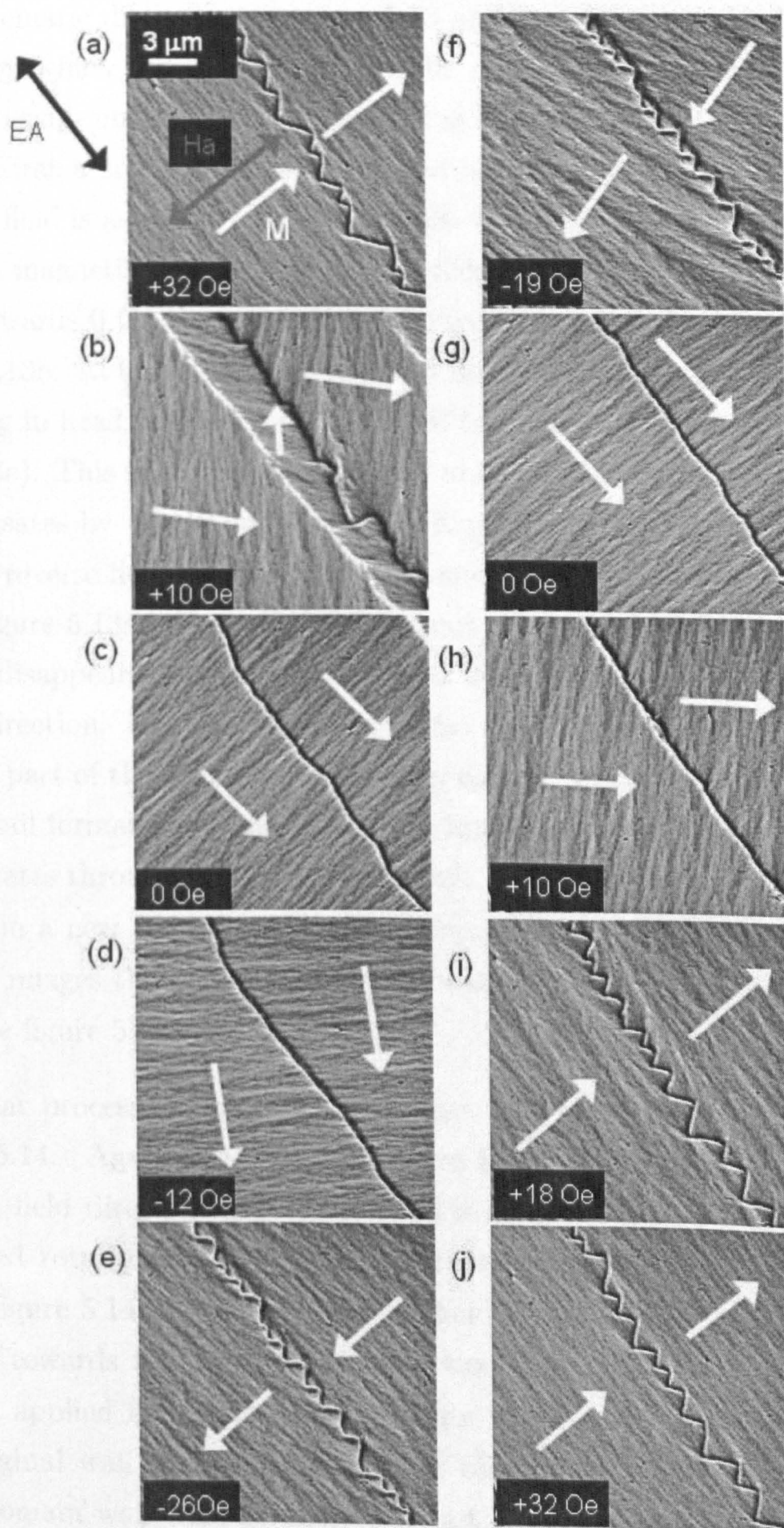


Figure 5.12: Hard axis magnetisation reversal of M8, NiFe1nm/CoFe5nm/(Al₂O₃1.5nm/NiFe1nm/CoFe5nm)x3 with red arrows indicating the direction of applied field and the white arrows the magnetisation direction.

The schematic diagrams in figures 5.13 and 5.14 show the likely mechanism by which the 360° domain walls remain during reversal. This is most easily understood by considering the hard axis reversal (figure 5.13). First a small offset between the hard axis and the direction of applied field is assumed to determine the direction of preferred rotation for each magnetisation vector. As the field is reduced from a saturated state towards 0 Oe the magnetisation direction rotates as illustrated in figure 5.13b. At 0 Oe the magnetisation now lies parallel to the easy axis resulting in head to head and tail to tail transitions within the wall (figure 5.13c). This is highly energetically unfavourable, therefore, the wall compensates by taking on a zigzag folding (figure 5.13d). By applying a small reverse field the magnetisation starts to rotate to align with the field (figure 5.13e). Here the bottom part of the wall (point q in figure 5.13d) disappears as the magnetisation is progressively aligned in the same direction. However, this is not the case for the magnetisation at the top part of the structure (point p in figure 5.13d). In this instance a tail to tail formation occurs (point r in figure 5.13e) and the magnetisation rotates through 360° within the wall. Applying a high enough field results in a new 360° domain wall forming (figure 5.13f), hence, in the Fresnel images the 360° domain wall contrast thereby reverses (see for example figure 5.6).

A similar process occurs during the easy axis reversal as illustrated in figure 5.14. Again it is assumed there is a small offset between the applied field direction and the easy axis to determine the direction of preferred rotation for each magnetisation vector. From the remanent state (figure 5.14a) as a small reverse field is applied the magnetisation rotates towards the applied field direction (figure 5.14(b)). At a high enough applied field a new 360° domain wall forms at the top part of the original wall and the bottom part of the wall disappears. A new 360° domain wall with reversed contrast is seen in the Fresnel images (figure 5.14(c)).

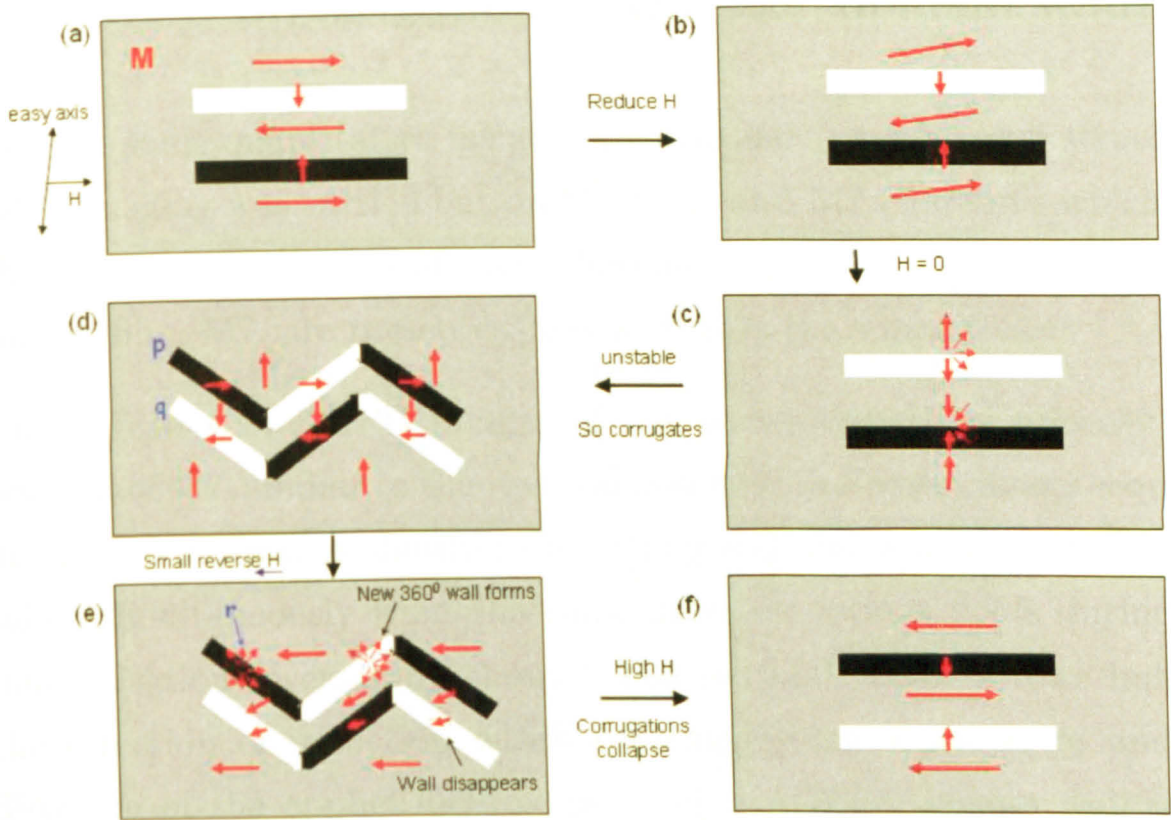


Figure 5.13: Schematic diagram showing hard axis reversal behaviour of 360° domain walls. The black and white colouring is used to illustrate the contrast observed in the Fresnel images.

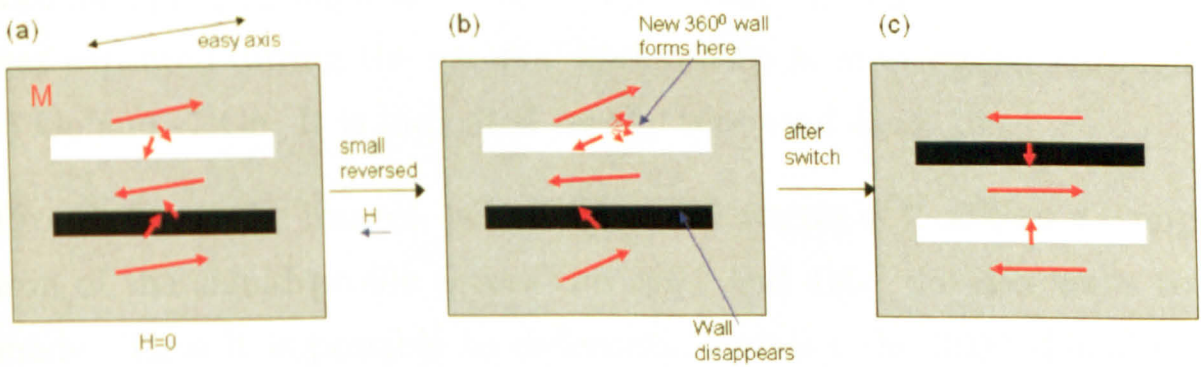


Figure 5.14: Schematic diagram showing easy axis reversal behaviour of 360° domain walls

5.4 DPC investigation of the 360° domain walls

To gain some quantitative insight into the 360° domain wall structures DPC imaging was carried out on films M5 and M7 (the films which had the greatest occurrence of 360° domain walls). The results from the bilayer film, M7, are presented first as this is the simpler case.

Figure 5.15 shows DPC images of the outward path of an easy axis reversal of M7, similar to the reversal observed in Fresnel image sequence in figure 5.9. Images showing the orthogonal components of induction, taken simultaneously from the same area, at various fields during the magnetisation reversal are shown. The red and yellow arrows indicate the direction of induction which the images are sensitive to and the direction of the applied field respectively. A 360° domain wall which was initially present is indicated by the green oval at +27 Oe. As the previous Fresnel studies showed the reversal is effected by a 180° domain wall sweeping through at ~ 7 Oe (figure 5.9). In this instance the wall was captured during the reversal and can be seen sweeping through at -6 Oe and -7 Oe. It is indicated by the blue oval at -7 Oe.

Processing of the images using Digital MicrographTM allows a comparison of the signal profile across the 360° and 180° domain walls to be made. Thus it is possible to determine whether the 360° domain wall exists in all the layers or, as suspected, only in one of the layers. The signal profile across the 180° domain wall is shown in figure 5.16 and the profile across the 360° domain wall is shown in figure 5.17. Comparison of the signal variation indicates the signal from the 360° domain wall is $\sim 1/2$ the signal from the 180° domain wall. Given that the 180° domain wall exists in the whole thickness of the structure, this suggests the 360° domain wall only exists in one of the CoFe layers in the bilayer film. This is illustrated in figure 5.18 which shows schematically the signals generated from a 180° and a 360° present in one or both layers of the bilayer film.

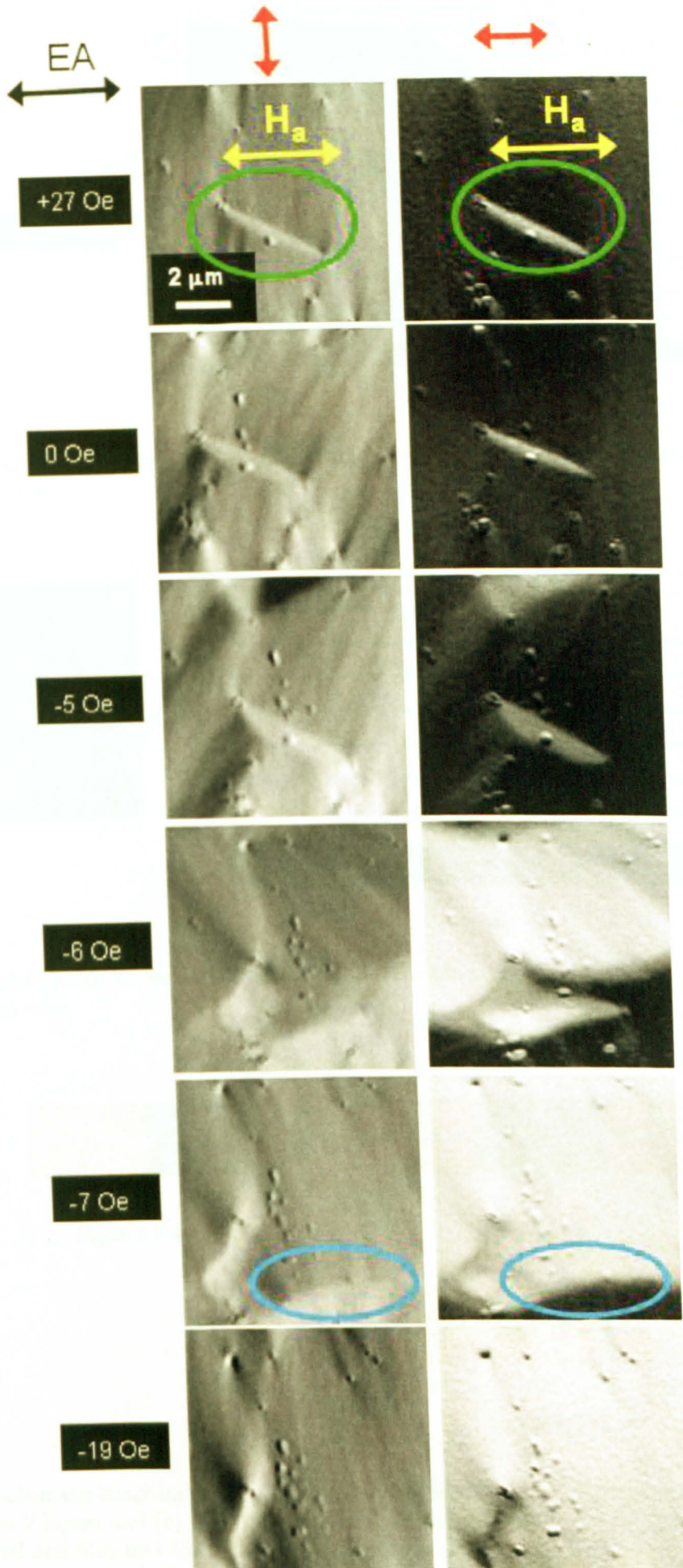


Figure 5.15: DPC image sequence during an easy axis reversal of M7, NiFe1nm/CoFe10nm/
Al₂O₃1.5nm/NiFe1nm/CoFe10nm

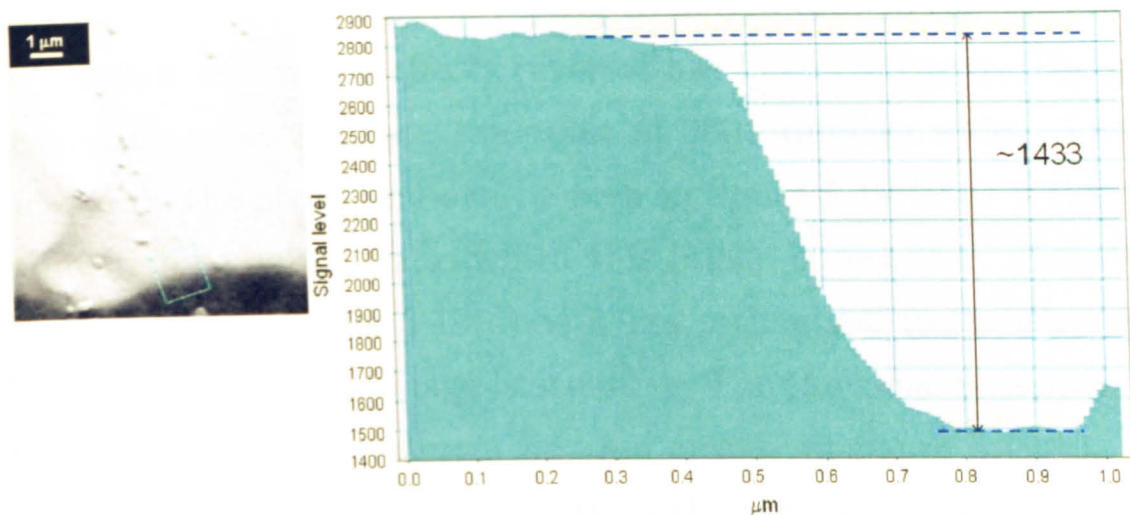


Figure 5.16: Signal profile across a 180° domain wall. The blue rectangle indicates the area which the profile was taken over.

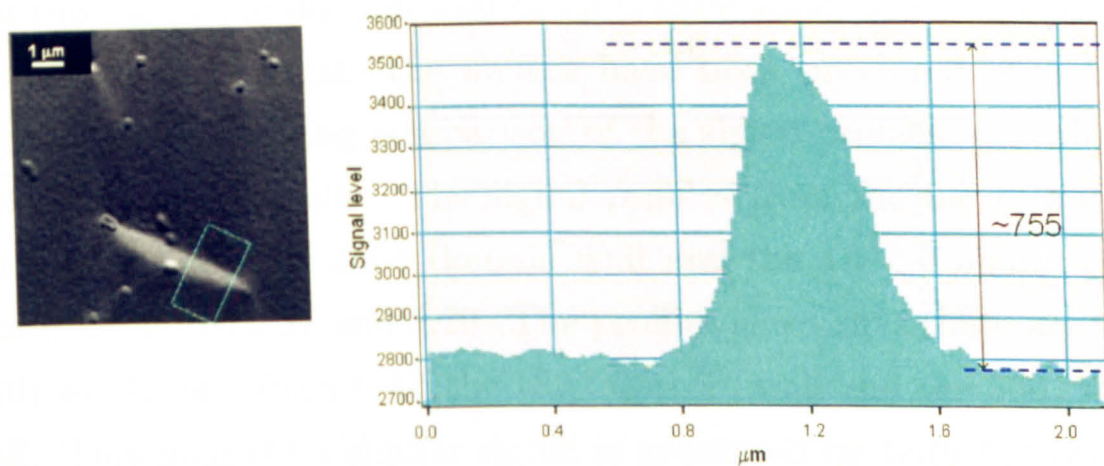


Figure 5.17: Signal profile across a 360° domain wall. The blue rectangle indicates the area which the profile was taken over.

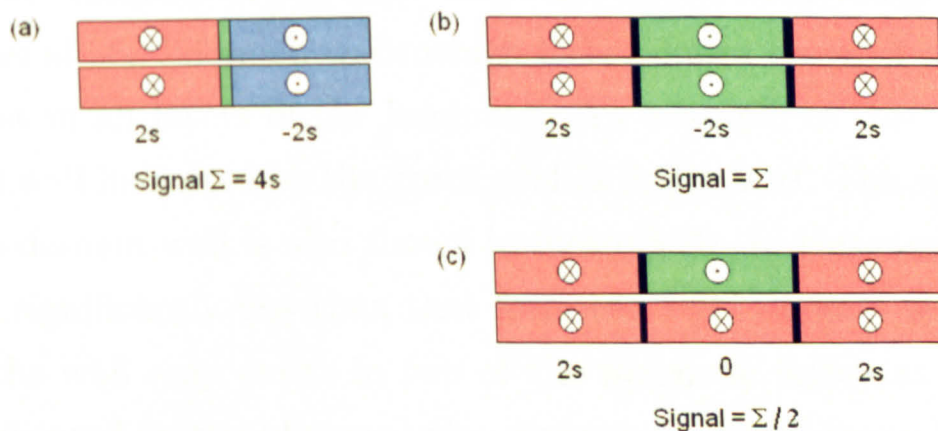


Figure 5.18: Schematic diagram of the signal generated from (a) 180° domain wall, (b) 360° domain wall present in 2 layers and (c) 360° domain wall present in 1 layer of a bilayer film. Domains are indicated in red and blue and the domain wall regions in green.

Figure 5.19 shows a set of DPC images from film M5. In this instance the 180° domain wall which effects reversal has been captured. The green, blue and red ovals indicate examples of 360° domain walls. The wall indicated by the green oval can be seen in figure 5.19(b) as it lies along the direction of induction to which this image is sensitive. However, it can not be seen in figure 5.19(a) as it lies orthogonal to the direction of induction to which this image is sensitive. For the same reason the wall indicated by the blue wall can be seen clearly in figure 5.19(c), but is less obvious in figure 5.19(d). Parts of the complex 360° domain wall structure indicated by the red oval in figure 5.19(d) have similar signal level to the uniformly magnetised material which has reversed suggesting that this particular domain wall extends throughout the whole thickness of the laminate. Again the images have been processed with Digital MicrographTM allowing comparison of the signal profiles from the 180° and 360° domain walls. The signal profiles from the most prominent part of this complex 360° domain wall and the 180° domain wall are shown in figures 5.21 and 5.20. The profiles show that there are similar contrast changes from both the 180° domain wall and the 360° domain wall. This suggests a similar signal is generated by both the 360° and 180° walls. Given that the 180° domain wall exists throughout the whole thickness of the film, then the 360° domain walls also extend throughout the whole thickness of the film. However, in the DPC images there are instances of 360° domain walls which have a lower contrast and thus do not exist in all layers of the laminate. An example of this is the 360° domain wall indicated by the green oval in figure 5.19. The signal profile for this domain wall is also shown in figure 5.20. In this case the signal level is significantly less than that from the 180° domain wall and it is likely the wall only exists in two of the magnetic layers at most. The wall indicated by the blue oval also generates a significantly lower signal (figure 5.22) indicating this wall is probably only present in two of the magnetic layers. A schematic illustration of the signal generated from a 360° domain wall present in one and two layers of the quadrilayer film

is given in figure 5.23.

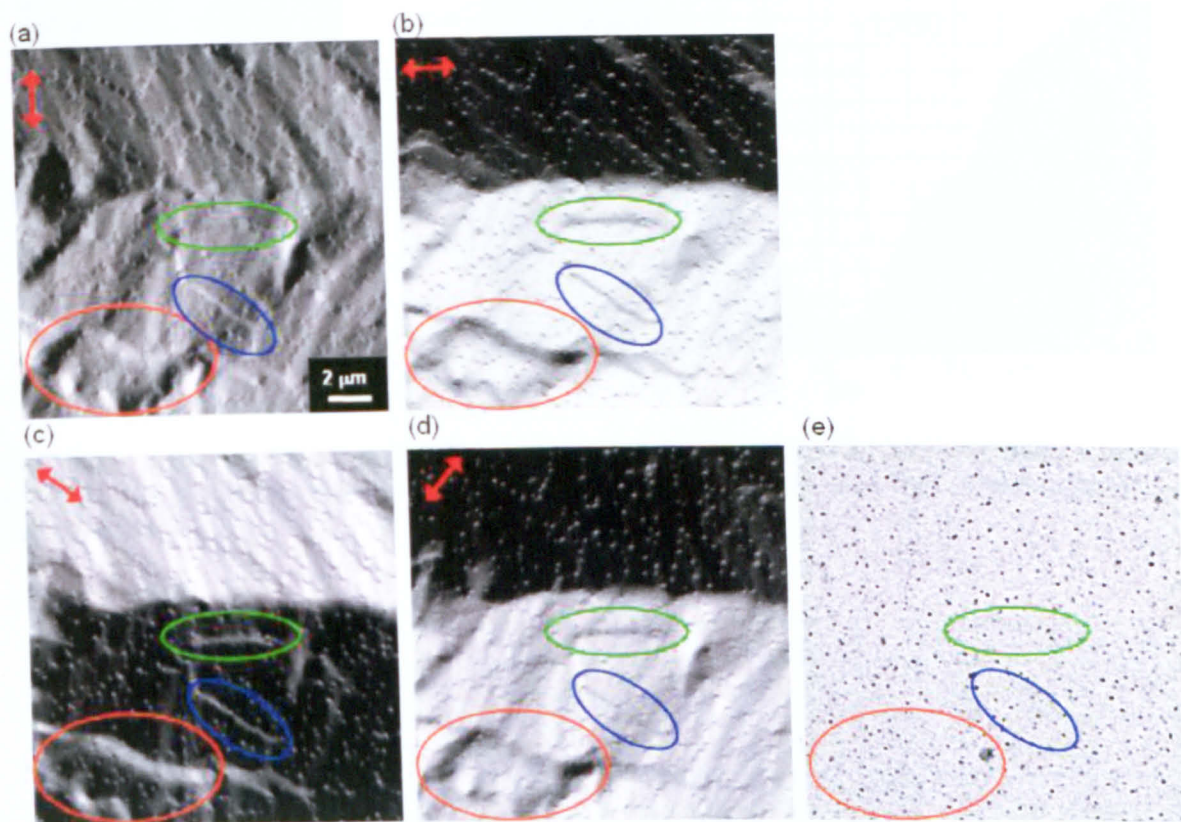


Figure 5.19: (a)-(d) DPC images of film M5. Red arrows indicate the direction of induction which the image is sensitive to. (e) corresponding bright field image. The coloured ovals highlight examples of 360° domain walls.

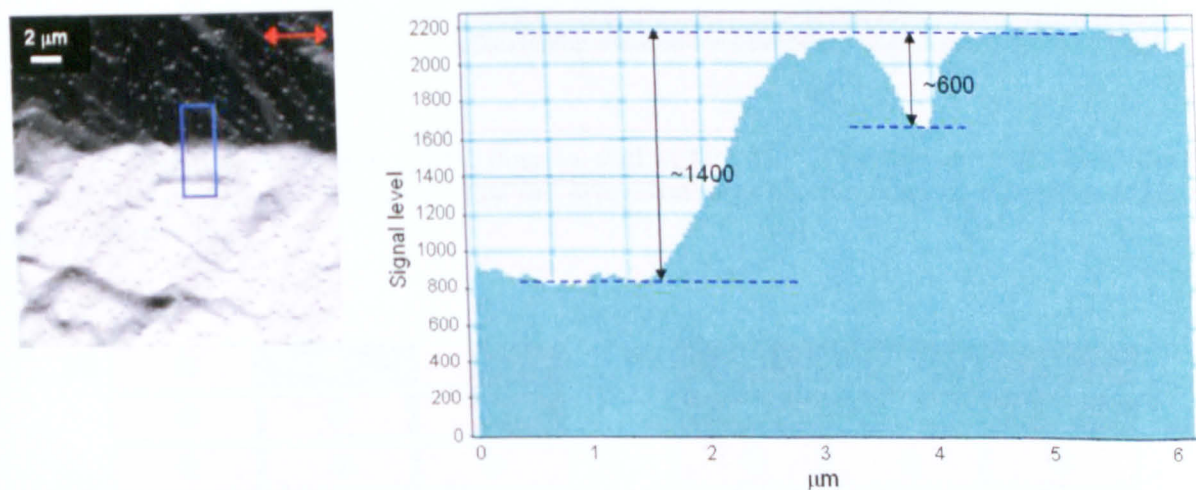


Figure 5.20: Signal profile across 180° and 360° domain walls in film M5. The blue rectangle indicates the area which the profile was taken over. The red arrow indicates the direction of induction which the image is sensitive to.

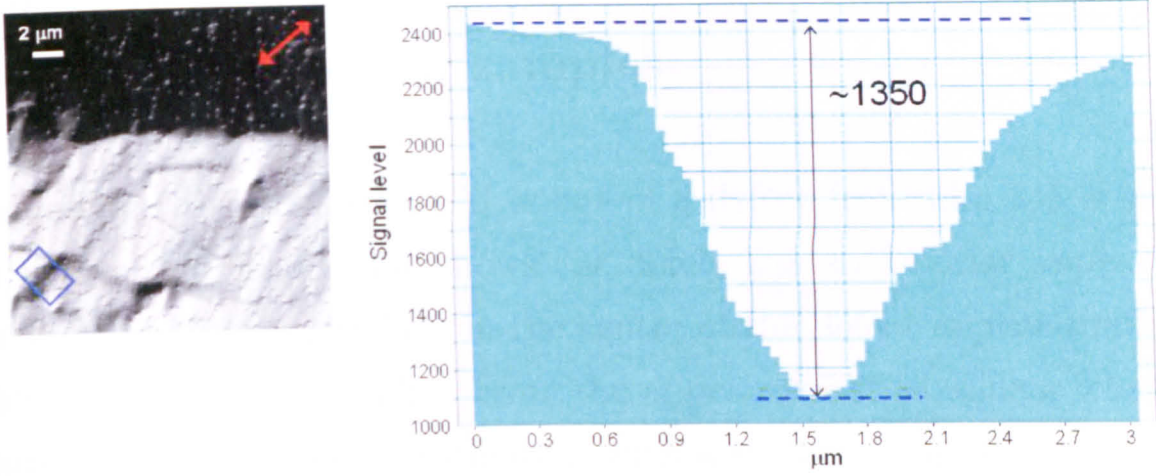


Figure 5.21: Signal profile across a 360° domain wall in film M5. The blue rectangle indicates the area which the profile was taken over. The red arrow indicates the direction of induction which the image is sensitive to.

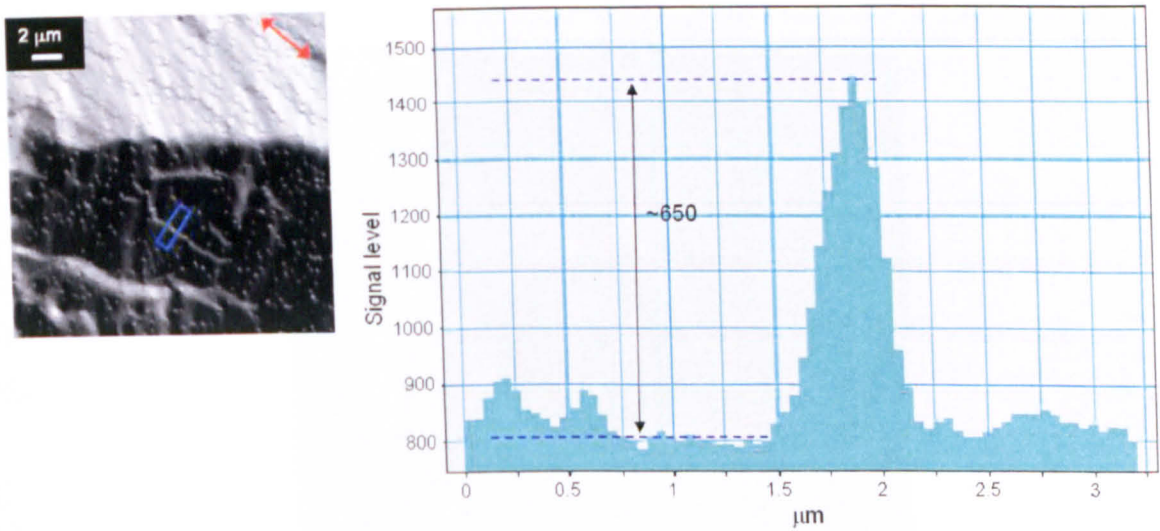


Figure 5.22: Signal profile across a 360° domain wall in film M5. The blue rectangle indicates the area which the profile was taken over. The red arrow indicates the direction of induction which the image is sensitive to.

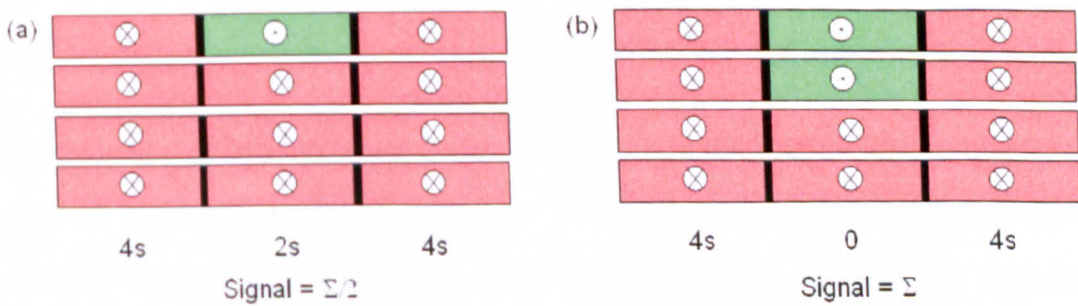


Figure 5.23: Schematic diagram of a 360° domain wall present in (a) one layer and (b) two layers of a quadrilayer film. Domains are indicated in red and domain walls in green.

5.5 Physical microstructure and elemental composition of planar samples

An enlarged bright field TEM image of a defect from film M5 is shown in figure 5.24. The image shows the defect has an annular appearance in TEM and the crystallites in the centre of the defect appear similar to those in the rest of the film. From the appearance it is unclear what has caused the defect and investigation with a surface imaging technique is required to determine the topology of the defect. This will be discussed in section 6.2

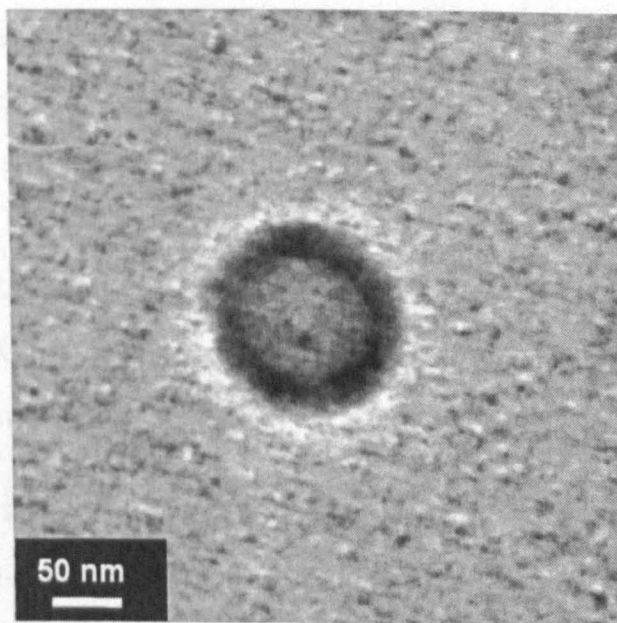


Figure 5.24: Bright field TEM image of a defect showing the visible crystallites within the annular defect.

To investigate whether there are any compositional differences between the defect regions and the regions without any defects, electron energy loss spectroscopy (EELS) has been carried out. Spectrum images were taken across two of the defect sites. HAADF images of the two areas with defects are shown in figures 5.25a and b with the spectrum image line traces indicated by the green lines. For each area core loss and low loss spectra were collected at ~ 5 nm intervals across the spectrum image.

This was done using a fast beam switch which allowed low loss and core loss spectra to be collected from the same area under the same electron optical conditions. Hence, deconvolution of the core loss spectra with the low loss spectra allowed removal of plural scattering effects from the core loss edge shape. The spectra included the O K-edge, Fe L_{2,3}-edges and Co L_{2,3}-edges which have edge onsets of 532 eV, 708 eV and 738 eV respectively. A dispersion of 0.5 eV/ch was used to allow simultaneous collection of the edges of interest. Processing of the data was performed using the microscopy software package Digital MicrographTM. A background of the form AE^{-r} , where A and r are constants and E is the energy, was fitted to the region immediately preceding the O K-edge and subtracted from the core loss parent spectrum image to give a second spectrum image. Figure 5.25c shows spectra taken from points a, b and c in the background subtracted spectrum image 1 and figure 5.25d shows the spectra for spectrum image 2. From the relative peak heights of the O, Fe and Co it appears that the defects are oxygen rich. This is most apparent at the edge of the defects (point b in figures 5.25a and b) where the Fe and Co peaks are significantly less intense when compared to the areas without defects (point a in figures 5.25a and b).

Deconvolution of the background subtracted core loss spectrum image with the low loss spectrum image was performed to remove plural scattering effects. A signal window of 50 eV was then set and the area under each edge integrated to give an intensity map of each element. This enabled the element profiles across the spectrum images to be determined. Figures 5.26 and 5.27 show the element profiles across spectrum image 1 and 2 respectively. The element profiles show the presence of oxygen is greatest at the edges of the defects. There is arguably an increase of Fe and Co at the edge of the defect, this is most apparent in figure 5.27. Although this is not as obvious as the increase in the O signal. This suggests it is likely that an oxide of Fe or Co is present. The t/λ for each spectrum image was calculated from the low loss spectrum image using equation 2.9. To show how the thickness varies across the spec-

trum image the resulting t/λ profile is also shown on figures 5.26 and 5.27. This confirms the defect sites are thicker than the uniform film with the centre of the defect ≈ 50 nm thicker than the rest of the film. However, the increase in t/λ in the centre of the defects is not due to the oxygen and has not been explained by the EELS results. The Fe and Co signals appear suppressed in the defect region. However, the element profiles have not been normalised to the zero loss peak and it is likely the Fe and Co signals have been depressed by extra scattering.

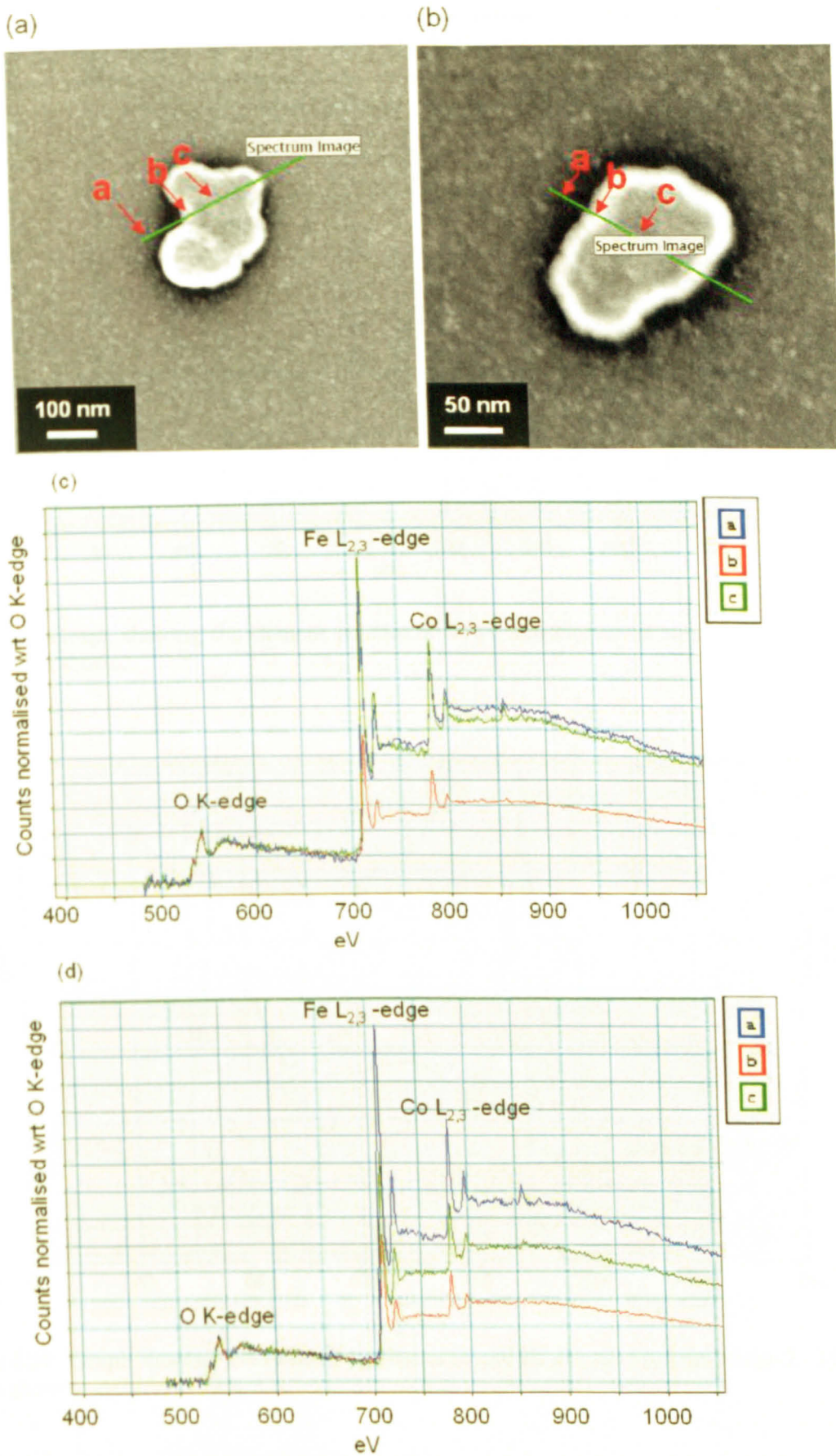


Figure 5.25: HAADF images of (a) defect site 1 and (b) defect site 2 showing the corresponding spectrum image line traces. Spectra, normalised with respect to the O K-edge, taken from points a, b and c on the line traces are shown in (c) and (d) for spectrum image 1 and 2 respectively.

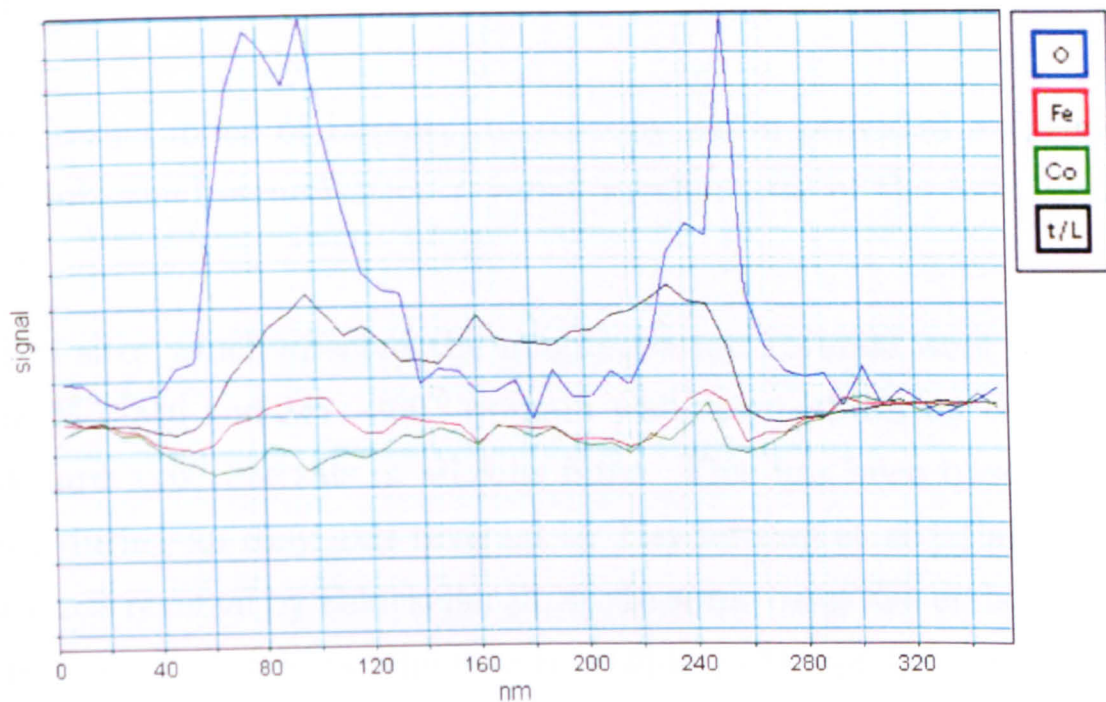


Figure 5.26: Graph showing the element profiles of O, Fe and Co across spectrum image 1. The t/λ profile is also shown.

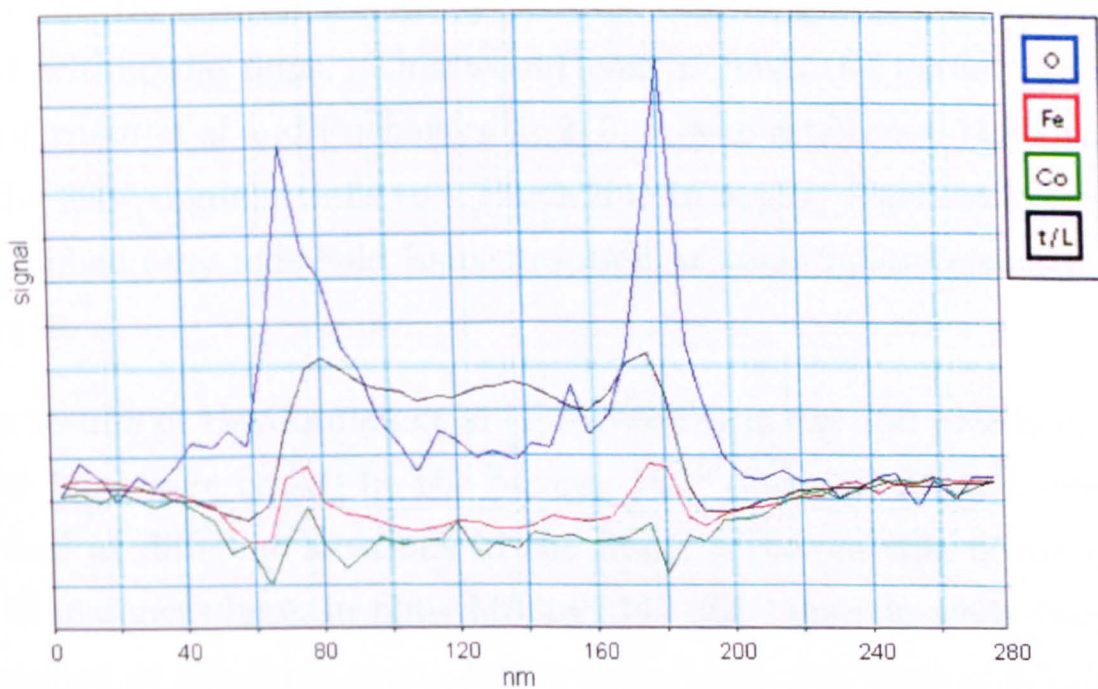


Figure 5.27: Graph showing the element profiles of O and Fe across spectrum image 2. The t/λ profile is also shown.

5.6 Discussion

The Fresnel mode of Lorentz microscopy again provided a detailed insight into the magnetisation reversal mechanisms of the four laminated films.

Defect sites which affected the magnetisation reversal were observed in films M5, M6 and M7. 360° domain walls formed during the easy axis and hard axis reversals in all four films. This has been observed previously during an easy axis reversal by Heyderman et al [1] and during a hard axis reversal by Feldtkeller [3, 4]. In some cases the ends of the walls were pinned at defects which were visible in bright field TEM images. However, there were also instances where the 360° domain walls did not end at the physical defect sites. This is similar to the observations in the multilayer film in chapter 4 where the pinning sites were not visible in HRTEM. However, it is entirely possible that magnetic inhomogeneities exist within the films. This would concur with the earlier studies of Heyderman *et al* and Puchalska [1, 2, 5, 6] who attributed the formation of the 360° domain walls to a Bloch line in a 180° Néel wall moving in an applied easy axis field being trapped at some inhomogeneity in the sample.

The results of Heyderman et al [1] showed that the 360° walls in multilayer films were erased by the passing 180° domain wall and new walls formed at different locations in the film. Although this is the case in some instances here, in films M5 and M7 360° domain walls frequently remained at the same position throughout reversal (figures 5.3, 5.4 and 5.6). These films had the largest density of defects and some walls persisted up to fields of a few hundred oersted suggesting the end points of the walls are very strongly pinned. Schrefl et al [7] simulated the formation and annihilation of 360° domain walls and found for a defect of 10 nm an external field of 280 Oe is needed to eliminate the 360° wall showing that the defects are indeed strongly pinned. It has also been

shown by Berkov et al [8] that the annihilation field of the pinned walls is strongly dependent on the defect geometry. When aligned along the hard axis the 360° domain walls took on a zigzag folding (see for example figure 5.12). This has again been observed previously and can be explained in terms of an equilibrium between the wall length and specific wall energy [2]. However, the fact that the 360° domain walls remain after reversal is a new observation and the likely processes which occur during the hard axis reversal have been discussed and are illustrated in figure 5.13.

DPC imaging has revealed that some of the 360° domain walls exist in all of the magnetic layers and some in only one or two layers. When a 360° domain wall is present in one layer a compensating wall can form in the neighbouring magnetic layer. Heyderman et al [1] showed the possibility of a 360° or a 0° compensating domain wall for the case where the original domain wall is inclined at 45° to the domain magnetisation direction. Using their arguments we consider compensating walls inclined at 0° to the magnetisation direction as would be the case for film M5. Figure 5.28 shows a schematic of the compensating walls. From the diagram it is evident that total charge compensation is achieved when the wall is aligned parallel to the magnetisation direction. Hence, it is still unclear why the signal level from the 360° domain wall in the DPC investigation is lower than would be expected for a wall present in two layers when compared to the signal from the 180° wall in film M5 (figure 5.20).

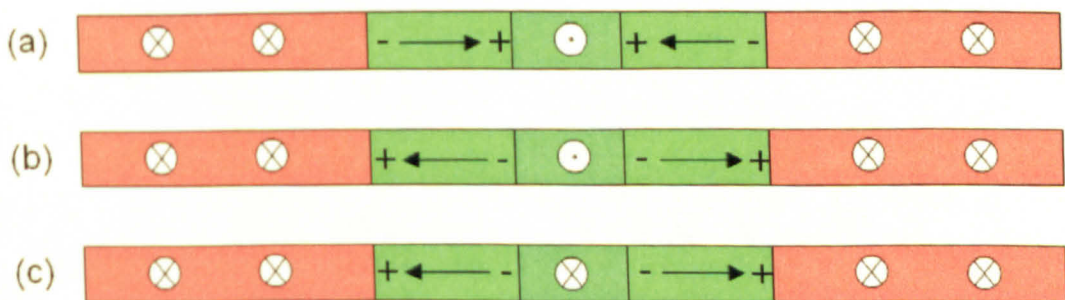


Figure 5.28: Schematic illustration of (a) 360° domain wall, (b) 360° compensating wall and (c) 0° compensating wall. The red areas indicate the domains and the green areas indicate the domain wall region.

Although the Lorentz microscopy investigation has revealed interesting properties of the four laminated films, the origin of the defect sites is still not understood. Therefore, in an attempt to gain further insight into the physical and elemental structure SEM of the planar samples has been carried out along with HRTEM and EELS investigations of cross sectional specimens. The findings from these studies are presented in chapter 6 and all discussion of the physical characterisation is left until section 6.5.

Bibliography

- [1] L. J. Heyderman, H. Niedoba, H. O. Gupta, and I. B. Puchalska, *J. Magn. Magn. Mater.* **96**, 125 (1991).
- [2] I. B. Puchalska and H. Niedoba, *IEEE Trans. Magn.* **27** (4), 3579 (1991).
- [3] E. Feldtkeller, *J. Appl. Phys.* **39** (2), 1181 (1968).
- [4] E. Feldtkeller and W. Liesk, *Z. Angew. Phys.* **14**, 195 (1962).
- [5] H. Niedoba, H. O. Gupta, L. J. Heyderman, I. Tomas, and I. B. Puchalska, *IEEE Trans. Magn.* **26** (5), 1527 (1990).
- [6] H. Niedoba, A. Hubert, B. Mirecki, and I. B. Puchalska, *J. Magn. Magn. Mater.* **80**, 379 (1989).
- [7] T. Schrefl, J. Fidler, and M. Zehetmayer, *J. Appl. Phys.* **87** (9), 5517 (2000).
- [8] D. V. Berkov, N. L. Gorn, R. Mattheis, and T. Zimmermann, *J. Magn. Magn. Mater.* **182**, 81 (1998).

Chapter 6

Structural properties of the CoFe thin Films

6.1 Introduction

This chapter investigates the physical and elemental structure of the CoFe laminate films in an attempt to establish the origin of the defects observed in chapter 5. SEM of the planar samples of film M5 has been carried out to gain greater knowledge of the surface topology of the defects.

Further cross-sectional TEM has been carried out on the laminate films to investigate the film growth. Bright and dark field TEM imaging and EELS were performed on two laminate films, M5 and M9. Their structures are described below. The magnetic behaviour of film M5 has been discussed in detail in chapter 5. However, film M9 is thick and not electron transparent when viewed in plan view, therefore the magnetic properties have not been investigated. However, the structure of film M9 is a more realistic example of the structures used in magnetic recording heads and thus the physical and elemental properties have been investigated.

M5	NiFe1nm/CoFe10nm/(Al ₂ O ₃ 1.25nm/NiFe1nm/CoFe10nm)(x3)
M9	NiFe1nm/CoFe22.5nm/(Al ₂ O ₃ 1.5nm/NiFe1nm/CoFe22.5nm)(x7)

6.2 SEM of film M5

Figure 6.1a and b show SEM images taken, at two magnifications, of the surface of film M5. Both images show the defects appear hemispherical and are thicker than the rest of the film. Typically the defects are 50 nm - 100 nm in size which agrees with the TEM results (section 5.5).

To investigate whether the defects were present before the film deposition or if they had been caused during the deposition a dual beam FIB/SEM, as described in chapter 2, was used. A protective platinum bar was deposited on top of the defects. Next the gallium ion beam was used to cut a trench through the area on which the platinum bar had been deposited. The electron beam was then used to image the area whilst slices were cut away from the trench until a defect was found, a technique known as serial sectioning [1, 2]. SEM images taken from the cross sectioned defects are shown in figure 6.1c and d. The image shown in figure 6.1c was taken immediately before breaking into the defect. Here the structure of the quadrilayer film and the substrate can be seen as indicated on the image. Figure 6.1d shows an image taken at the centre of a defect. This shows the presence of a hemispherical particle on the substrate, hence the defects are caused by some process before the film is deposited. The film grows on top of the particle, but there is an indent at the edge of the particle. This is seen in the surface images as a deficiency of material around the defects (figure 6.1a and b).

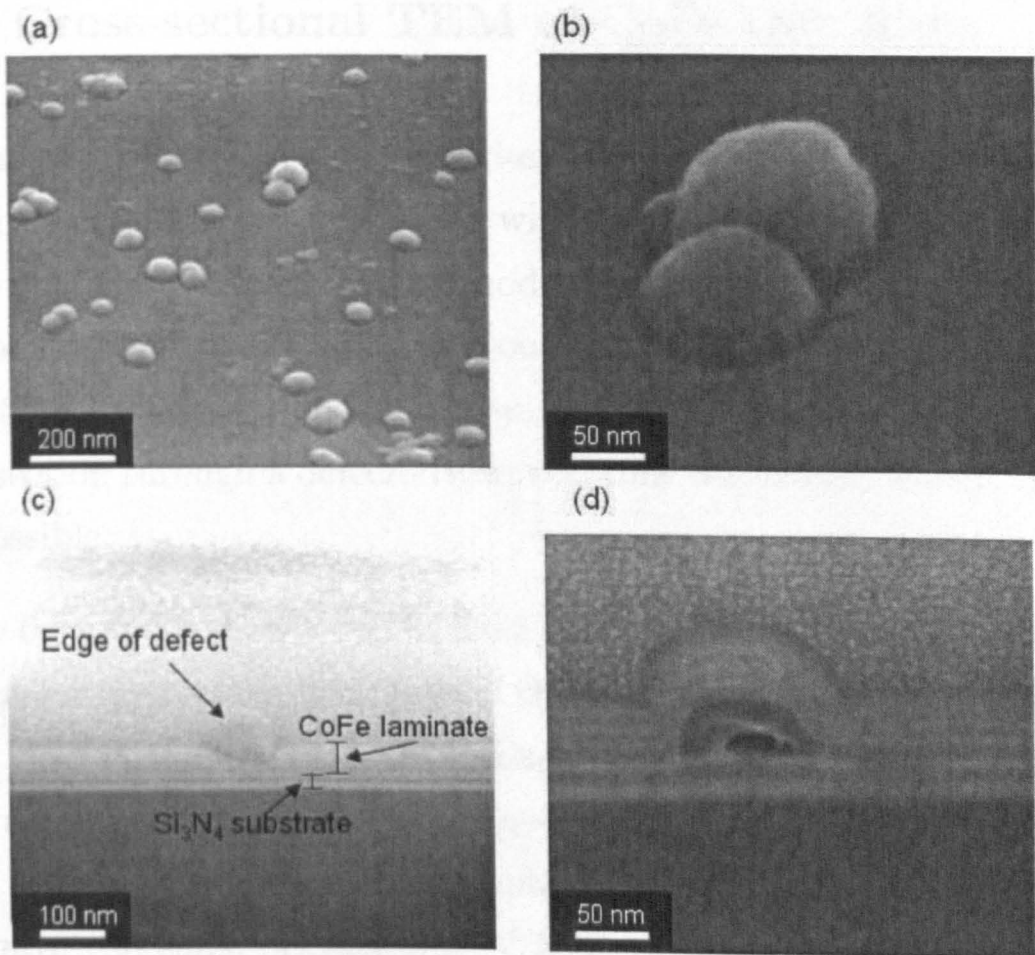


Figure 6.1: (a) and (b) SEM image of the surface of M5 showing the defects, (c) and (d) cross-sectional SEM images of the defects showing the multilayer film on top of the defect.

6.3 Cross-sectional TEM of CoFe thin films

In an attempt to identify the particles which are present on the substrate TEM cross sections were prepared with the encapsulation method. Due to the low sampling of this method no defects were found; however, imaging and analysis was carried out to investigate the growth of the CoFe films. The dual beam FIB would have enabled preparation of a cross-section through a defect. However, time limitations meant this was not possible.

Figure 6.2a and b show a bright field image of M5 and a dark field image of the same area, taken from part of the (110) diffraction ring. Unlike the bright field image, the dark field image allows determination of whether the grains have the same crystallographic orientation. The red ovals in figure 6.2a and b indicate an example of grains in different layers which may have the same orientation. Whilst this is not immediately obvious from the bright field image, the dark field image clearly shows both grains are diffracting strongly in the same direction. In the samples investigated there were a few instances of this where the grain growth does appear to have been affected by that in underlying layers. However, the occurrence of this was not as frequent as first thought from the bright field images of the cross-sectional samples. An example of such an area is given in figure 6.2c and d which show bright and dark field images of M9. Here the red ovals indicate areas in the bright field image in which it appears the grains are ‘talking’ to each other, but in the corresponding dark field image it can be seen that the grains do not have the same crystallographic orientation. The dark field imaging has revealed that although the grain boundaries in subsequent CoFe layers may occur at the same point the grains are in fact in different orientations. From close inspection of several dark field images it was found that approximately 0.5% of grains appear to have a similar orientation to those in the underlying layer.

It is also worth noting the roughness level of the spacer layers noticeably increases with distance from the substrate. As in film M4, section 4.6, there is evidence that the roughness is caused by grains in underlying CoFe layers.

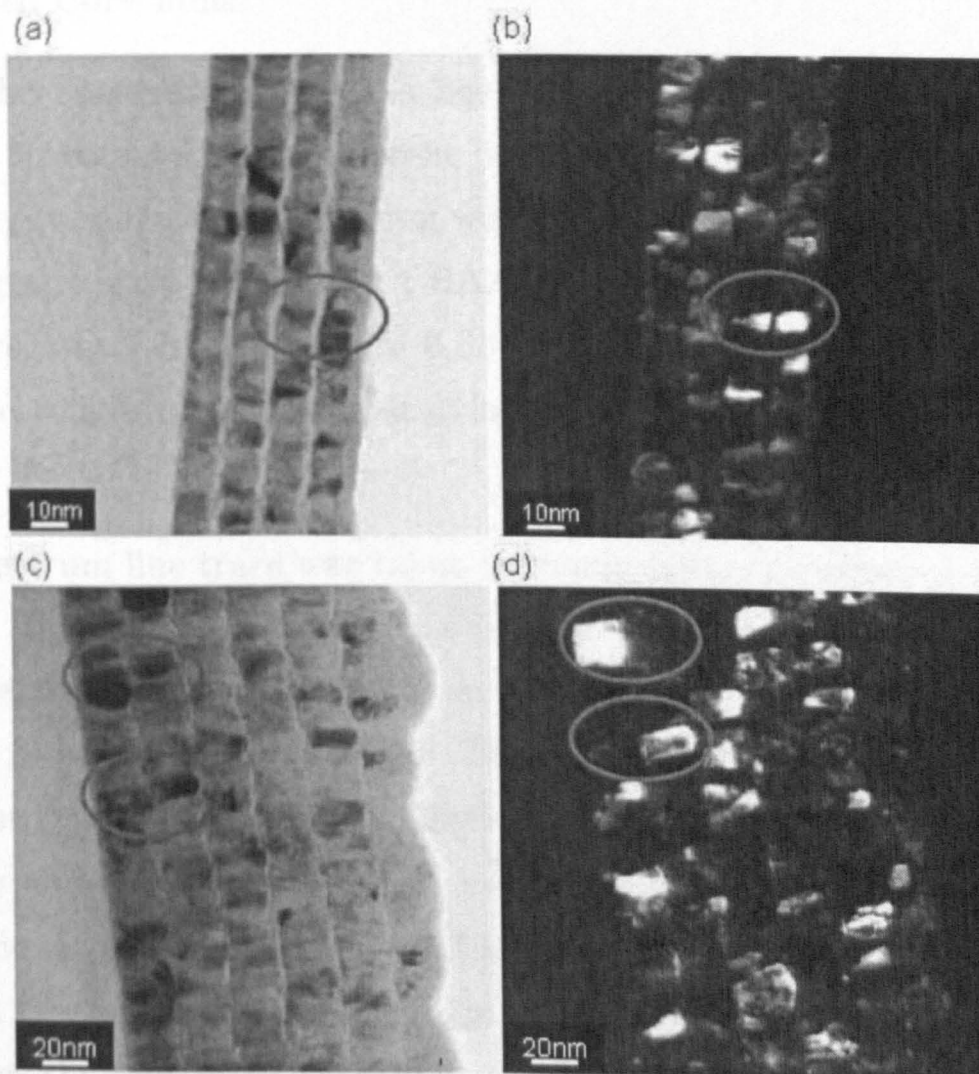


Figure 6.2: (a) BFTEM and (b) DFTEM of M5, NiFe1nm/CoFe10nm/(Al₂O₃1.25nm/NiFe1nm/CoFe10nm)x3. (c) BFTEM and (d) DFTEM images of M9, NiFe1nm/CoFe22.5nm/(Al₂O₃1.5nm/NiFe1nm/CoFe22.5nm)x7.

6.4 EELS investigation of CoFe laminate films

Electron energy loss spectroscopy of the cross-sectional specimens has been carried out to profile the elemental distribution throughout the laminated CoFe films.

An EELS spectrum image has been collected to produce an array of spectra corresponding to different points across a line trace in film M5. The energy range and dispersion were set to include the Fe, Co and Ni $L_{2,3}$ edges. Figure 6.3a shows a HAADF image indicating the spectrum image region of M5 and figure 6.3b the spectrum image line trace. In 6.3a the roughness of the spacer layers, similar to that in film M4 in chapter 4, can be seen.

The spectrum line trace was taken from substrate to surface with points every 1 nm and probe diameter ~ 0.6 nm. This was poor sampling and retrospectively it would have been more sensible to select a probe diameter of at least the step size. The data was processed using a built in quantification function in Digital MicrographTM. Here a background window and signal window were set for each edge. As the edges of interest lie close to each other the background window was limited to 40 eV and the signal windows were limited to 50 eV. The area under each edge was then integrated to give an intensity map of each element, thus the element profiles across the spectrum image were determined. Figure 6.3c shows the element profiles across the spectrum image. The element profiles have been normalised individually and are plotted against an arbitrary scale, hence the exact composition can not be determined from the plot. The Fe and Co signals agree with each other quite well apart from the top CoFe layer where the Co signal falls off sharper than that of the Fe. This implies the surface layer which can be seen in the HAADF image has a greater Fe content and may be due to an Fe oxide layer. At the first seedlayer, indicated by number 1 in figure 6.3c, the Ni peak appears wider than in the subsequent seedlayers, numbered 2-4. It should

also be noted that the Ni peaks 2-4 appear to tail into the CoFe. Roughness along the beam direction, consistent with the BFTEM images, can be seen in the HAADF image which may explain the Ni tailing into the CoFe layer. That the Fe and Co signals do not fall to zero at the spacer layer may also be due to this roughness.

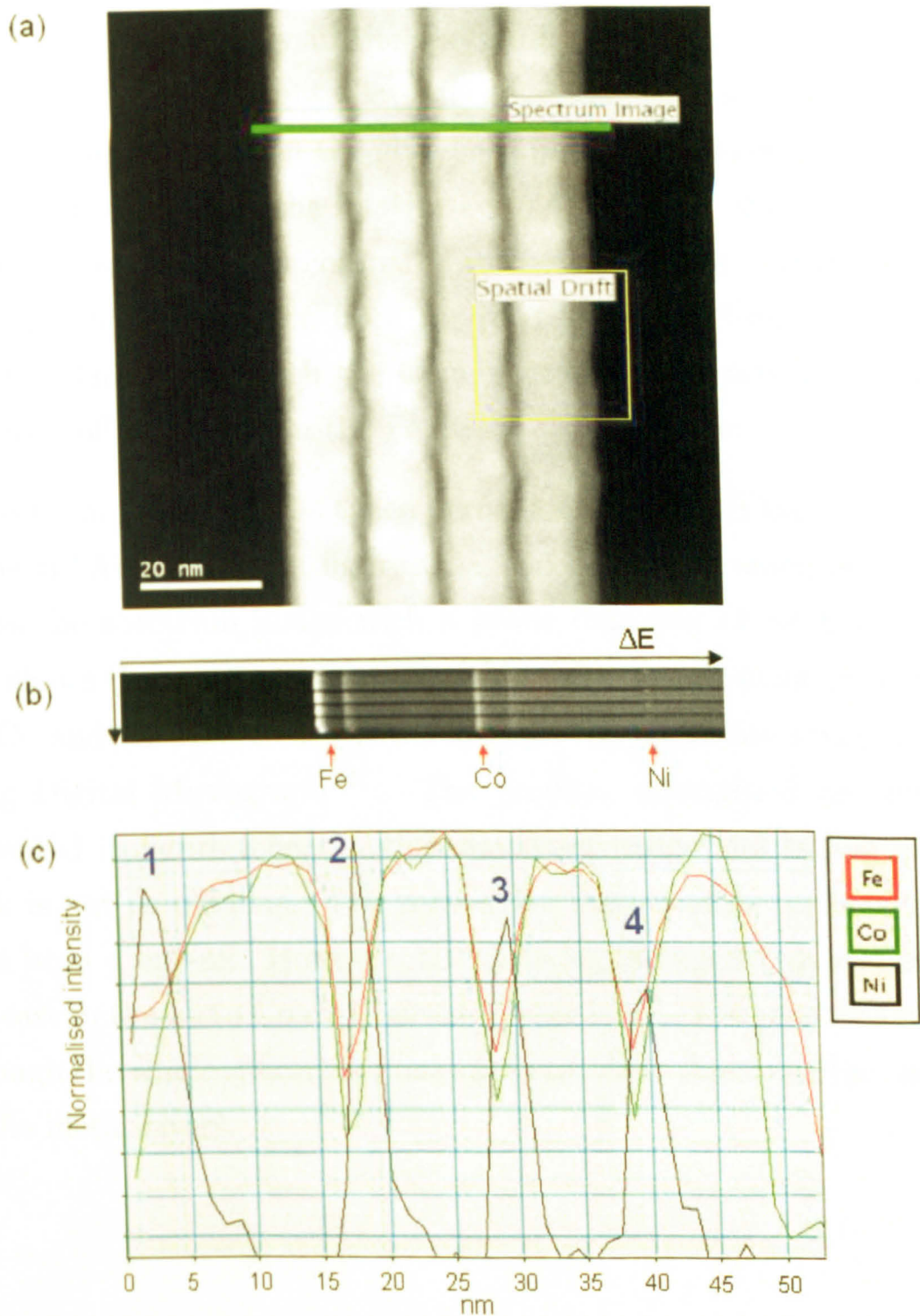


Figure 6.3: (a) Survey image showing spectrum image region, (b) spectrum image and (c) elemental profiles across the spectrum image of NiFe1nm/CoFe10nm/ (Al₂O₃1.25nm/NiFe1nm/CoFe10nm) \times 3.

To investigate whether there is a tailing of the Ni peak a further spectrum image has been taken from film M5 with more closely spaced points. The start energy of the spectrum was changed to include the oxygen K-edge and the dispersion was set at 0.5 eV/channel. Typical EELS spectra taken from points along the spectrum image at the CoFe layer, the NiFe seed layer and the Al₂O₃ spacer layer are shown in figure 6.4. An unexpected edge is present immediately before the Fe L_{2,3} edge and can be seen most clearly in the spectrum taken from the spacer region (figure 6.4c). It is thought that this edge may be due to fluorine which may have been present in the glue used in the cross-section preparation. Also it is worth noting the relative Fe to Co content appears to increase in the spacer layer when compared to the CoFe layer and the seed layer spectra. This can be seen from the relative peak heights in each of the spectra. This agrees with the element profiles in figure 6.3c where the Co drops off further than the Fe at the spacer layers.

A spectrum line trace was taken across the top spacer layer as indicated in the HAADF image in figure 6.5a. Spectra were taken every 0.2 nm across the spectrum image with a probe diameter of ~ 0.6 nm. Figure 6.5b shows the resulting spectrum line trace. The element profiles for O, Fe, Co and Ni were then extracted from the spectrum image as before using Digital MicrographTM. The profiles, normalised as before, are presented in figure 6.5c. In this spectrum image the tailing of the Ni peak is not as obvious. The reason for this remains unclear and may have been a one-off. However, the data again suggest there may be an increase in the Fe to Co ratio at the spacer layer. The presence of oxygen through the whole spectrum image is most likely due to surface oxidation of the metal layers.

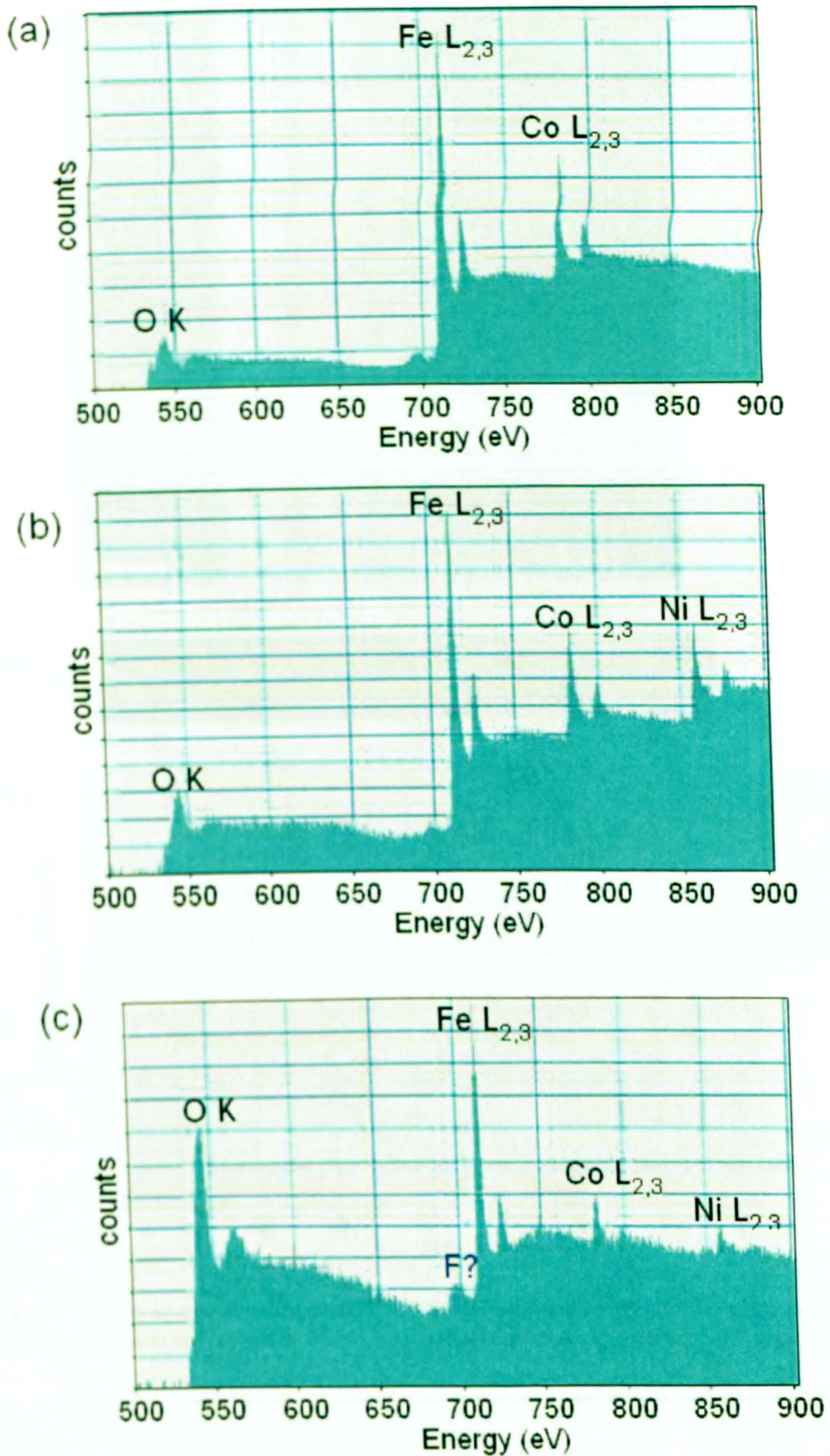


Figure 6.4: Typical EELS spectra taken from (a) a CoFe layer, (b) a NiFe seed layer and (c) a Al_2O_3 spacer layer in film M9, NiFe1nm/CoFe10nm/ (Al_2O_3 1.25nm/NiFe1nm/CoFe10nm) \times 3.

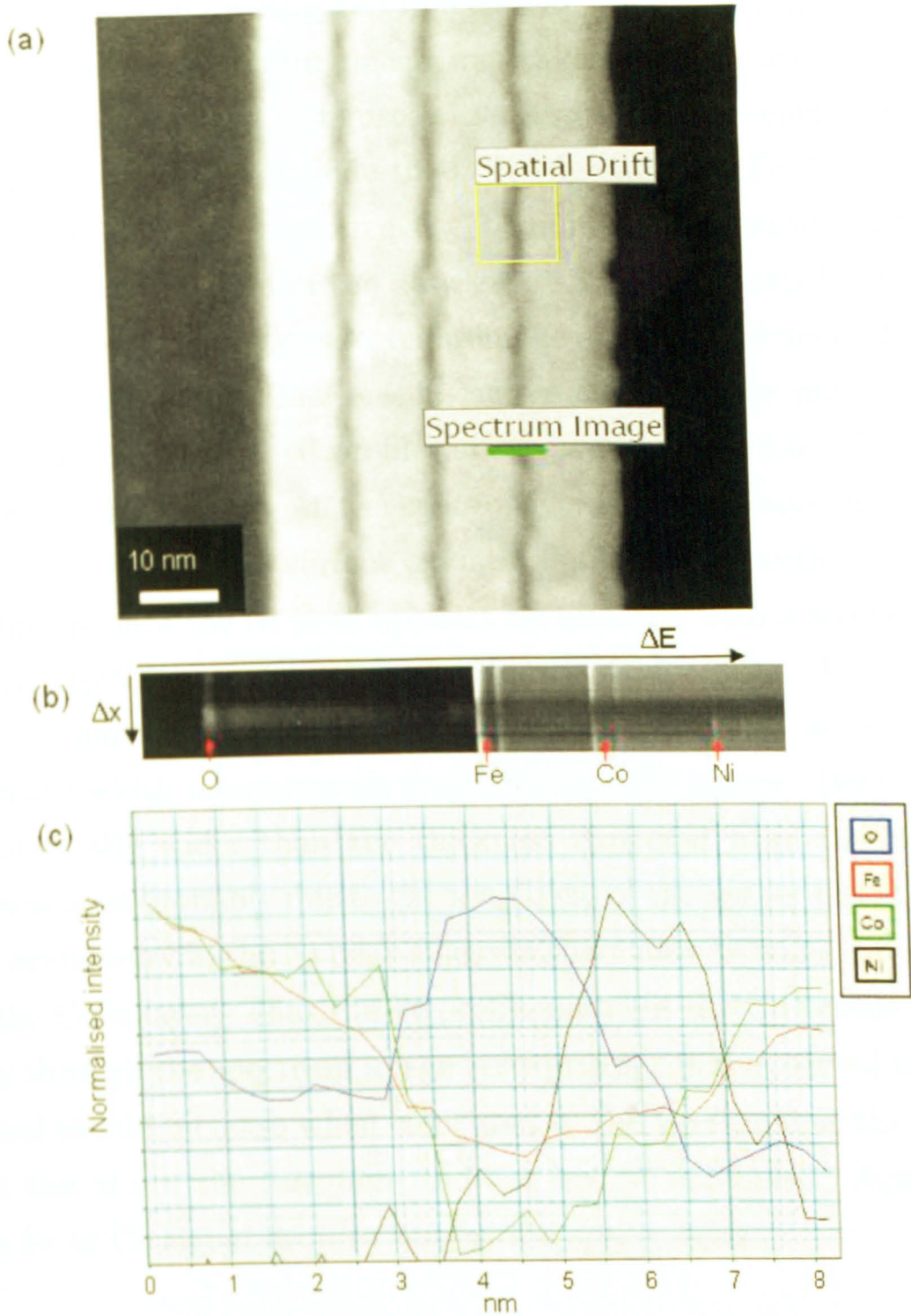


Figure 6.5: (a) Survey image showing spectrum image region, (b) spectrum image and (c) elemental profiles across the spectrum image of NiFe1nm/CoFe10nm/ (Al₂O₃1.25nm/NiFe1nm/CoFe10nm)x3.

Film M9 has been investigated in a similar fashion to film M5. However in this case the spectrum image was taken over an area as indicated in the HAADF image in figure 6.6a. As before, the energy range and dispersion were set to include the O K-edge and the Fe, Co and Ni L_{2,3} edges. A spectrum was taken every 0.3 nm over an area of ~ 12.5 nm by 1.5 nm. Quantification of the data gave an element map for each of the edges of interest over the spectrum image area. The elemental maps are shown in figure 6.6b. The profiles across each of these maps have been taken and the normalised profiles are shown in figure 6.6c. The O signal is greatest in intensity at the spacer layer, but is always present. This is most probably from surface oxidation of the cross-sectional specimen. In this instance the Ni peak appears asymmetric with a steeper slope at the Al₂O₃/NiFe interface than the NiFe/CoFe interface. The Ni FWHM is ~ 2.5 nm and the Al₂O₃ FWHM is ~ 3 nm which is in agreement with the width measurement from the HAADF image. Both layers are substantially wider than the thickness expected from the deposition. This is most probably due to the roughness of the spacer layers, although the asymmetry in the Ni peak suggests there may be some diffusion of Ni in the CoFe layer. That the Fe profile matches the Co profile the whole way through the spectrum image is surprising. It is expected that the Fe signal should increase when compared to the Co signal at the seedlayer, but this is not the case here and can not be explained. Again neither the Fe or Co signal drop to zero at the spacer layer.

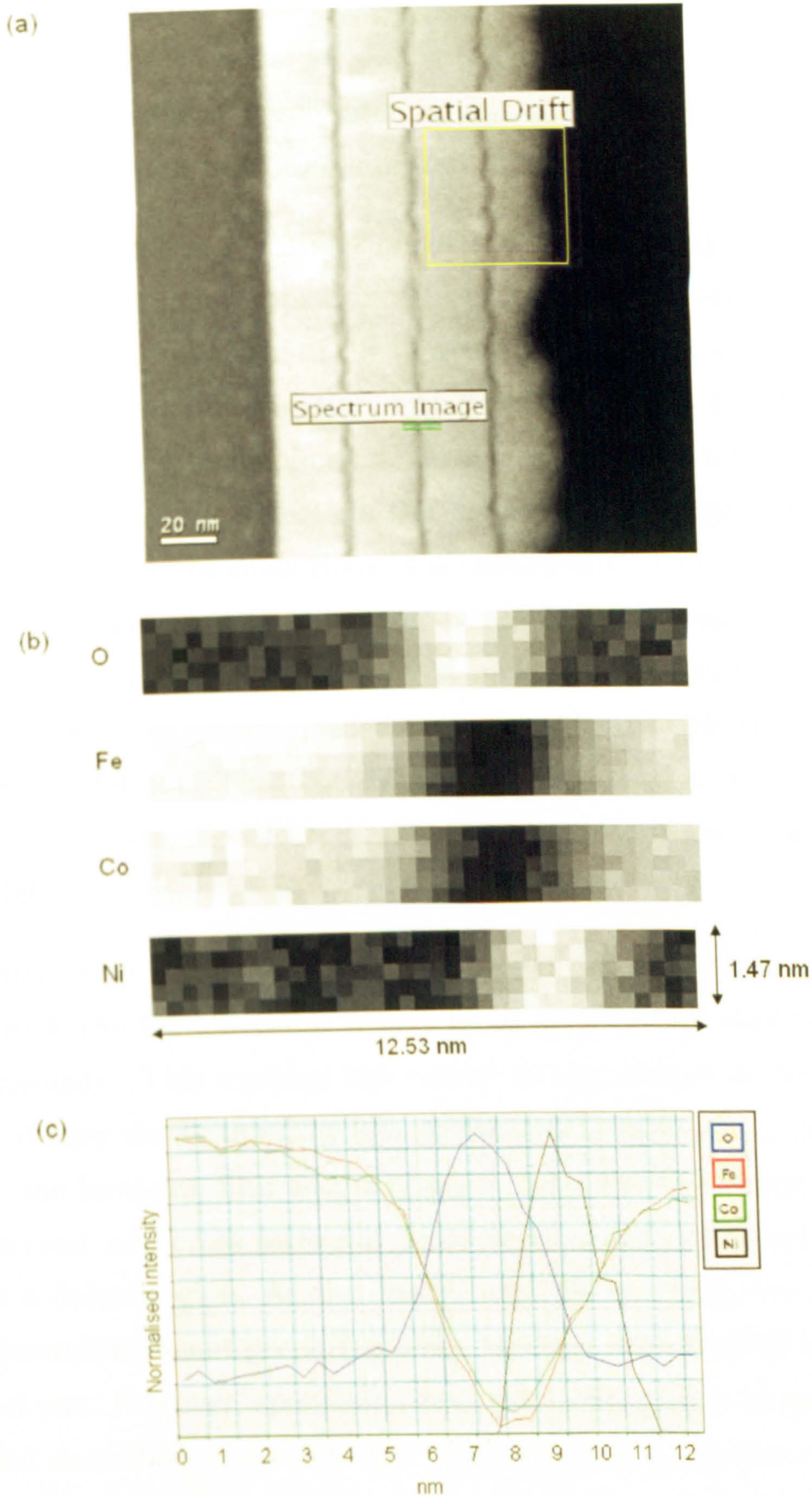


Figure 6.6: (a) Survey image showing spectrum image region, (b) elemental maps of O, Fe, Co and Ni. (c) elemental profiles across the spectrum image of NiFe1nm/CoFe22.5nm/(Al₂O₃1.5nm/NiFe1nm/CoFe22.5nm) $\times 7$.

6.5 Discussion

Following the results from chapter 5, this chapter explored further the physical structure of the CoFe laminate films.

The TEM and EELS investigation of the planar samples revealed the defects have an annular appearance (section 5.5) and were thicker in the centre. However, the origin of the increase in thickness was not apparent from these studies. Investigation with SEM has shown the defects are in fact approximately hemispherical. A deficiency of material can be seen around the edge of the defects in the surface SEM images. However, the cross-sectional images show there is no deficiency. This can be explained from the weaker secondary electron signal from this area. The annular appearance of the defects in the TEM images is still puzzling and cross-sectional TEM images are needed to investigate the film structure at the edge of the defects. That the defects are oxygen rich around the edge was revealed from the EELS studies and suggests these areas are prone to oxidation.

The dual beam FIB proved a useful tool in cross sectioning the defect areas with the Ga ion beam whilst imaging with the electron beam simultaneously. This enabled the centre of the defects to be found and revealed they were caused by the presence of a particle on the substrate before the laminate film was deposited. The identity of the particles is still unclear and cross-sectional TEM was carried out in an attempt to detect a defect region. As the dual-beam FIB is a new tool at Glasgow, time restraints meant preparing cross-sections with the FIB could not be carried out. However, specimens were prepared using the encapsulation method described in section 2.8. With the encapsulation method it is not possible to be specific about the area which is thinned to electron transparency. This along with the low sampling of the technique meant the chances of finding a defect region were small and indeed none were found.

The cross-sectional TEM did, however, allow the structure of the film to be studied. As seen in chapter 4 section 4.6 there was an increase in the spacer roughness with distance from the substrate and it can be attributed to the grains in the underlying layers. This roughness is not unusual in sputtered multilayered films and there have been several investigations into understanding the roughness [3, 4, 5] and optimising the deposition conditions to minimise it. The dark field observations have confirmed that the spacer layers are effective at breaking up the growth between the CoFe layers throughout the majority of the film, although there are occasional instances where the grains may be connected across two layers.

The EELS studies have suggested there may be a tailing of the Ni into the CoFe or it may just be from the roughness. Previous studies on spin valve materials have studied the diffusion of Ni into CoFe layers [6] which implies diffusion in the case of the laminate films is entirely plausible. Although there are still many unanswered questions from the EELS results it was noted that the Fe and Co signals do not drop off to zero at the spacer layers and the Co does not drop off to zero at the seed layer. It is thought this is most likely due to the roughness of the interfaces which was observed in both BFTEM and HAADF images.

Although the cross-sectional TEM study was unsuccessful in finding a defect, it is suggested that the particles which are responsible for the defects occur from some process carried out after the TEM membranes have been etched, but before deposition. As the particles are 50 nm - 100 nm in size and are regularly dispersed across the substrate it is unlikely they are due to handling. Preparation of cross-sectional specimens of the defects with the dual beam FIB is required to gain more information and will be discussed in section 8.3. Preliminary results from studies of this kind suggest there may be an oxide of silicon present, although the data are by no way conclusive and thus have not been presented here.

The SEM results showed the film growth was significantly disturbed by

particles present on the substrate and hence it is expected the local magnetisation around the particles is disturbed. It is thought this disturbance provides the necessary pinning sites for the 360° domain walls observed in chapter 5. In chapter 4 the termination points of the 360° domain walls were attributed to the roughness of the space layers and this is thought to be the case for the instances where the 360° domain walls terminate at non defect sites in chapter 5. It is suggested that the walls which are present throughout the whole thickness of the laminate terminate at the structural defect sites and it is these strongly pinned walls which remain throughout the magnetisation reversals. For the instances where the walls exist in one or two layers at most it is likely the termination sites are due to the roughness and the walls are confined to the uppermost layers where the roughness is greatest. The structural characterisation of the laminate films has revealed the nature of the pinning sites, however, further micromagnetic calculations similar to those carried out by Schrefl et al [7] are required to gain a greater understanding of the micromagnetic behaviour at the termination points. This will be discussed in section 8.3.

Bibliography

- [1] M. D. Uchic, M. A. Groeber, D. M. Dimiduk, and J. P. Simmons, *Scripta Materialia* **55**, 23 (2006).
- [2] D. N. Dunn and R. Hall, *Appl. Phys. Lett.* **75** (21), 3414 (1999).
- [3] X. W. Zhou *et al.*, *Acta Mater.* **49**, 4005 (2001).
- [4] D. J. Larson *et al.*, *Phys. Rev. B* **67**, 144420 (2003).
- [5] D. J. Larson, A. K. Petford-Long, Y. Q. Ma, and A. Cerezo, *Acta Materialia* **52**, 2847 (2004).
- [6] R. T. Huang *et al.*, *J. Magn. Magn. Mater.* **260**, 28 (2003).
- [7] T. Schrefl, J. Fidler, and M. Zehetmayer, *J. Appl. Phys.* **87** (9), 5517 (2000).

Chapter 7

Patterned soft magnetic films

7.1 Introduction

The studies in chapters 4 to 6 on the continuous films have provided useful and interesting information on the magnetic and physical properties of the CoFe films. However, it is of technological interest to investigate how the films would behave when patterned down to a shape and size similar to that of a perpendicular recording write head.

As the write head is miniaturised to accommodate the increase in areal density, there are many factors in the design which need to be taken into account. Previous studies have investigated the effect of trailing shields on the write field [1, 2, 3]. As mentioned in chapter 1, the remanent field of the write head is also an important factor and various aspects of the writer geometry have been studied to achieve lower remanence [4, 5, 6]. Other groups have focused on the pole-tip geometry, in particular, interest has been given to the effects of the geometry when writing at skew [7, 8, 9]. Trapezoidal geometries have been proposed to alleviate the problem of interaction with previously written data when the write pole is skewed with respect to the track direction [10]. Gao and Bertram [11] modelled the write field of a tapered-neck pole and compared it to various other pole designs. They found the tapered-neck pole achieved much larger write fields and field gradients than those without a tapered-

neck.

Here the interest lies in understanding the micromagnetic processes occurring during the reversal of six “head” shapes. The “pole tip” width has been varied for shapes with and without a tapered-neck; the geometries are given in section 7.2. This chapter reports preliminary studies of patterned permalloy films. Permalloy was chosen as it is isotropic, thus allowed observation of the effect of the shape anisotropy on the reversal of a film without a well defined anisotropy axis. Time limitations meant the CoFe films studies in the previous chapters have yet to be patterned.

7.2 Fresnel Studies of Patterned Permalloy films

Six head shapes have been patterned by electron beam lithography and lift-off (as described in section 2.9) and a 30 nm permalloy film deposited. Each shape has been investigated using the Fresnel mode of Lorentz microscopy. A schematic diagram showing the shapes and their dimensions is given in figure 7.1.

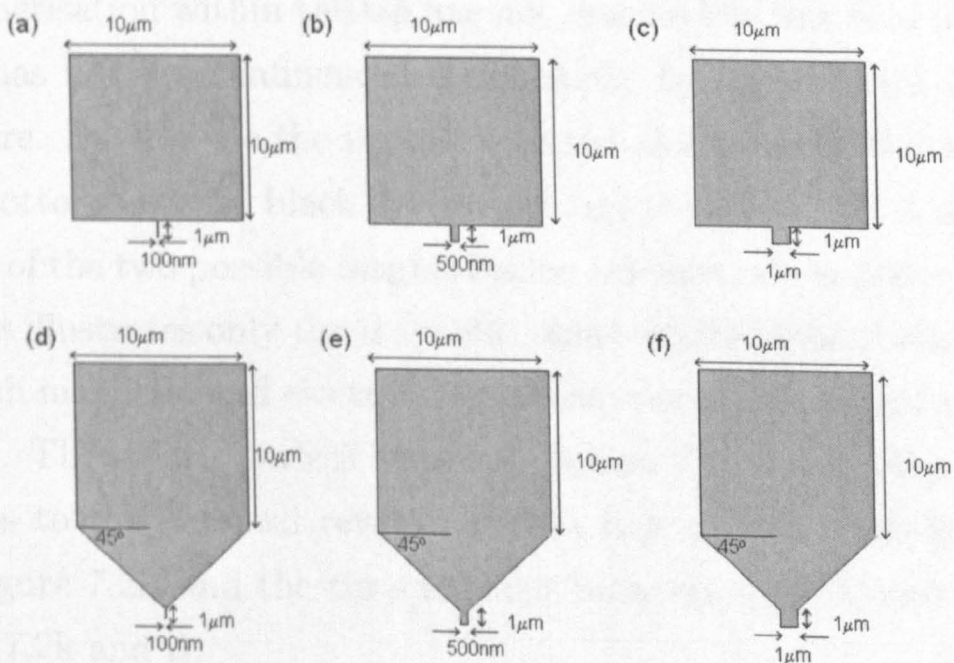


Figure 7.1: Schematic diagram of head shapes (a) H1, (b) H2, (c) H3, (d) H4, (e) H5 and (f) H6.

The evolution of magnetic microstructure has been investigated for the applied field directed parallel to the “pole tip”. Images at various fields during the magnetisation reversal are shown. The applied field and magnetisation directions are indicated by red and white coloured arrows respectively.

Figure 7.2 shows the reversal of H1 which has a pole tip width of 100 nm. As the field is reduced from +130 Oe to +16 Oe the magnetisation takes on a C-state shape (figure 7.2b). At 0 Oe the magnetisation is almost in a flux closure state in the main body of the element, although a 180° cross-tie domain wall has formed (figure 7.2c). The cross-tie domain wall forms as it is harder to reverse the magnetisation close to the edge of the element. As the field is applied in the opposite direction the domain which has its magnetisation direction along the applied field direction grows at the expense of the other domains (figure 7.2d). By -32 Oe the cross-tie domain walls no longer remain and the majority of the shape has reversed. Here the magnetisation has taken on a flower state where the magnetisation at the edges of the element points in opposite directions in an attempt to minimise the energy (figure 7.2e). However, the magnetisation within the tip has not reversed at this field indicating the tip has not been influenced significantly by the reversal in the $10\ \mu\text{m}$ square. By -132 Oe the tip has reversed as seen from the white line on the bottom and the black line on the top in figure 7.2f. A schematic diagram of the two possible magnetisation orientations is shown in figure 7.3. This illustrates only the magnetic phase whereas the Fresnel images have both magnetic and electrostatic phase contributions and amplitude contrast. The return path is shown in figures 7.2g-l and follows similar processes to the outward reversal with a flux closure state forming at 0 Oe (figure 7.2i) and the tip switching between +36 Oe and +130 Oe (figures 7.2k and l).

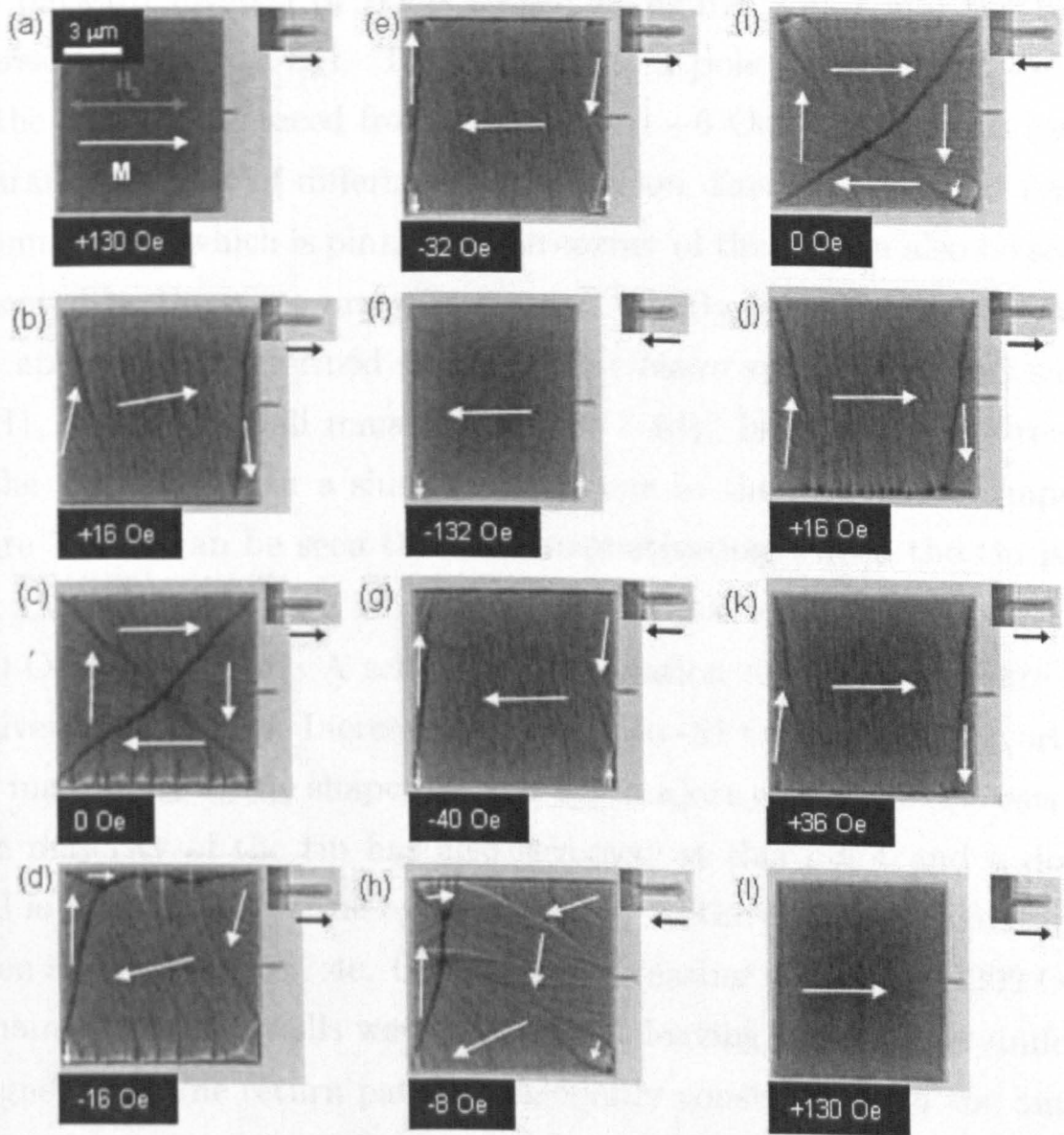


Figure 7.2: Fresnel reversal of H1. Red and white arrows indicate the direction of applied field and magnetisation direction respectively. The Black arrows indicate the magnetisation direction within the tip.

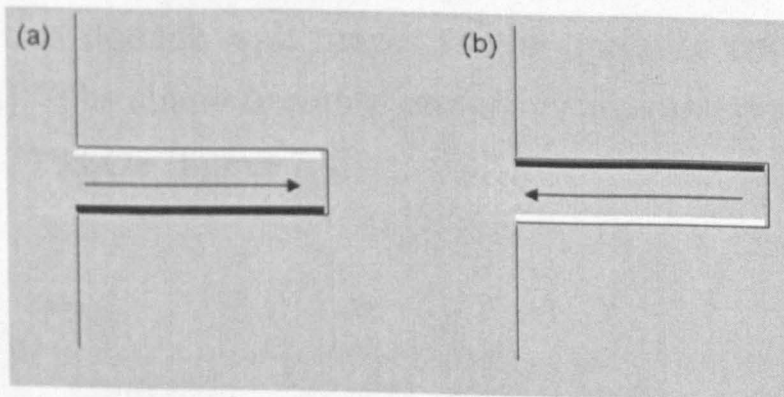


Figure 7.3: Schematic illustration of the Fresnel intensity in the tip of H1.

The outward reversal of H2 is shown in figures 7.4a-f and the return reversal in figures 7.4g-l. This shape has a pole tip width of 500 nm. As the field was reduced from +198 Oe to +6 Oe domain walls formed separating regions of differing magnetisation direction (Figures 7.4a-c). A domain wall which is pinned at the corner of the tip can also be seen as indicated by the green arrow in figure 7.4b. By 0 Oe the magnetisation had approximately formed a quasi-flux closure state. However, similar to H1, a cross-tie wall remained (figure 7.4d). In this case the reversal in the tip occurs over a similar field range to the rest of the shape. In figure 7.4d it can be seen that the magnetisation within the tip is in a flux closure state which is perfectly acceptable for a rectangular shape at 0 Oe applied field. A schematic illustration of the flux closure state is given in figure 7.5. Increasing the field to -31 Oe pushed the vortex in the main body of the shape out and the majority of the shape reversed. The majority of the tip has also reversed at this point and a domain wall is now pinned at the opposite corner of the tip as indicated by the green arrow in figure 7.4e. On further increasing the field to -202 Oe the remaining domain walls were pushed out leaving the element uniformly magnetised. The return path is reasonably consistent with the outward path (figures 7.4g-l). However, the reversal in the tip does not go via a flux closure state indicating this structure can support different domain structures within the tip. Similar to the outward reversal, a domain wall which is pinned at the corner of the tip can be seen (figure 7.4i) as the tip switches this domain wall moves to the opposite corner of the tip (figures 7.4i-j). The shape becomes uniformly magnetised as the field is increased to +198 Oe (figure 7.4l)

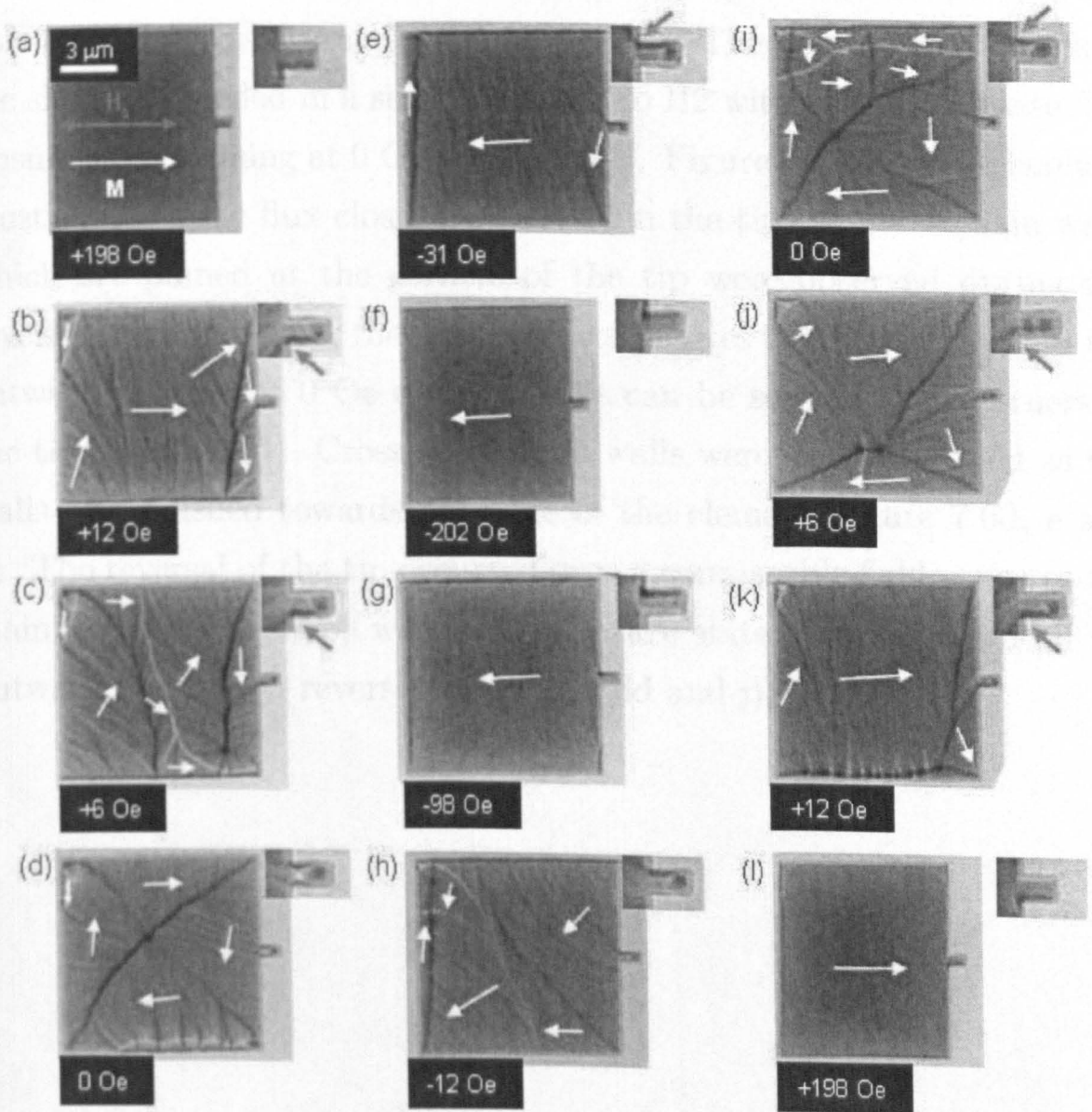


Figure 7.4: Fresnel reversal of H2. Red and white arrows indicate the direction of applied field and magnetisation direction respectively.

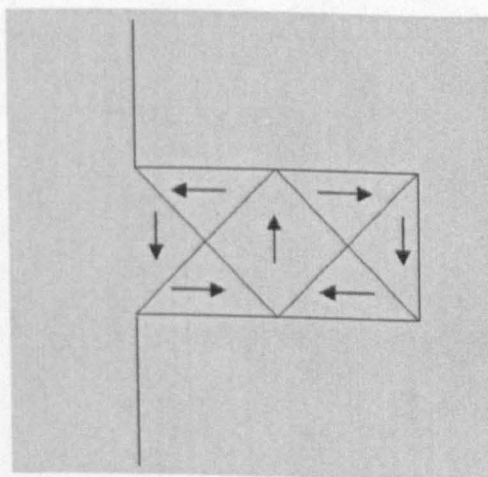


Figure 7.5: Schematic illustration of the Fresnel intensity in the tip of H2 at 0 Oe applied field.

The magnetisation reversal of H3 is shown in figure 7.6. In this case the pole tip width was $1\ \mu\text{m}$ giving a square tip. The reversal in the bulk of the shape proceeded in a similar fashion to H2 with an approximate flux closure state forming at 0 Oe (figure 7.6d). Figure 7.7 shows a schematic illustration of the flux closure state within the tip. Again domain walls which are pinned at the corners of the tip were observed during the reversal as indicated by the green arrows (figures 7.6c, e, i and k). In the outward reversal at 0 Oe domain walls can be seen at both corners of the tip (figure 7.6d). Cross-tie domain walls were again observed as the walls were pushed towards the edge of the element (figure 7.6d, e and k). The reversal of the tip occurred over a comparable field range to the main body of the shape with a flux closure state occurring in both the outward and return reversals (figures 7.6d and j).

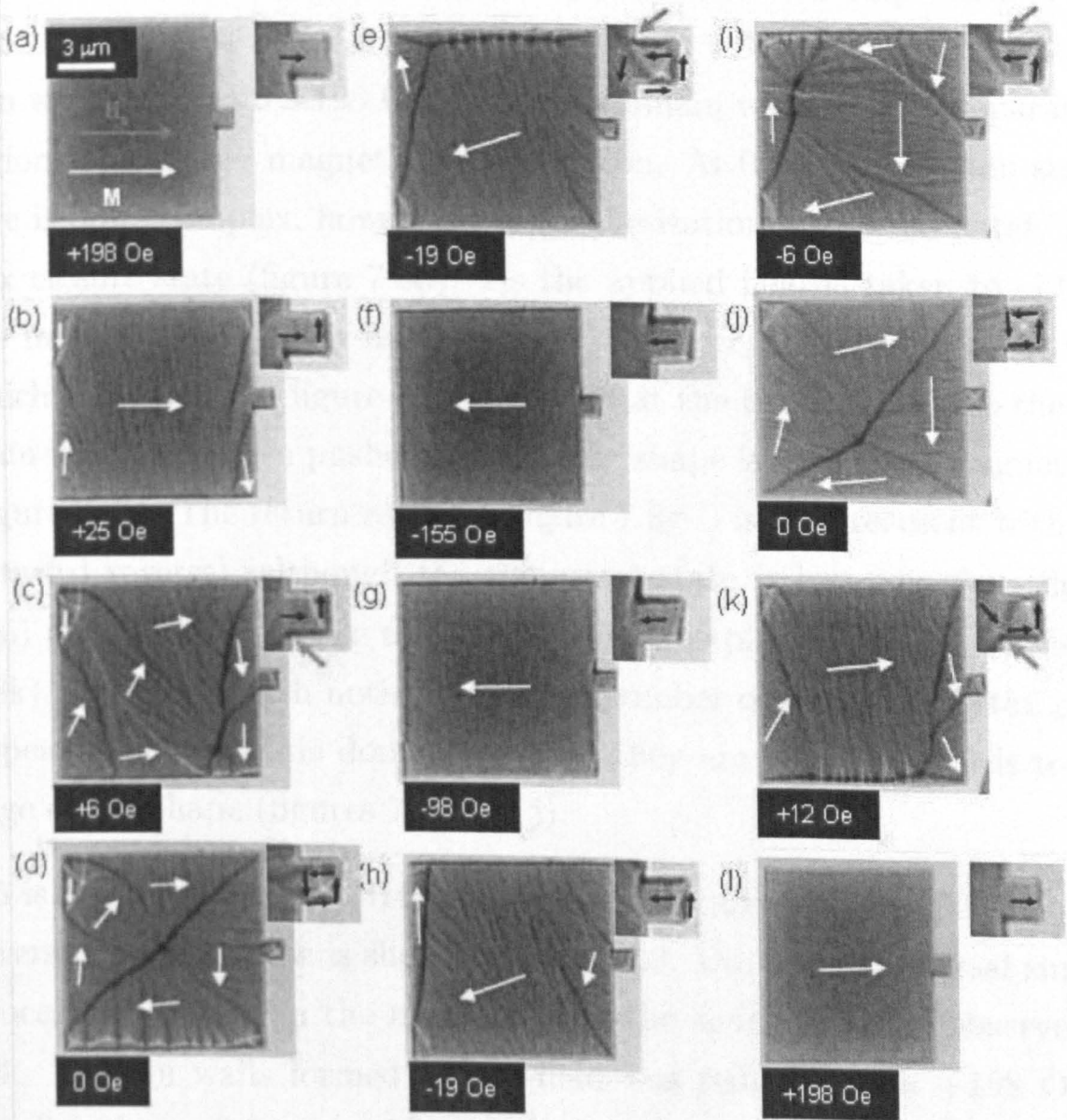


Figure 7.6: Fresnel reversal of H3. Red and white arrows indicate the direction of applied field and magnetisation direction respectively. The Black arrows indicate the magnetisation direction within the tip.

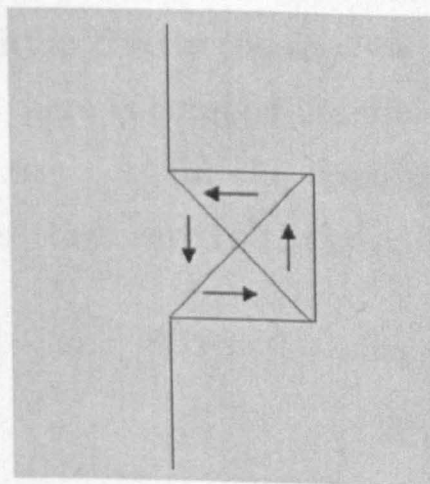


Figure 7.7: Schematic illustration of the Fresnel intensity in the tip of H3.

The next shape to be studied had a 'tapered-neck' and a tip width of 100 nm. The outward reversal is shown in figures 7.8a-f. As the magnetisation was taken from +198 Oe to +6 Oe domain walls formed separating regions of differing magnetisation direction. At 0 Oe the domain structure is quite complex, however, the magnetisation is approximately in a flux closure state (figure 7.8d). As the applied field is taken to -13 Oe the majority of the film has reversed. However, the light domain wall which is observed in figure 7.8e is pinned at the tip. By -202 Oe the domain walls have been pushed out and the shape is uniformly magnetised (figure 7.8f). The return reversal (figure 7.8g-l) is in agreement with the outward reversal, although the remanent state is less complex (figure 7.8i) and in this case the dark domain wall is pinned at the tip (figure 7.8k). It is also worth noting a greater number of cross-tie/vortex pairs appear in the cross-tie domain walls as they are pushed towards to the edge of the shape (figures 7.8l and j).

H5 is a similar shape to H4, but with a pole tip width of 500 nm. The reversal for this shape is shown in figure 7.9. During the reversal similar processes occurred in the main body of the shape to those observed in H4. Domain walls formed as the field was reduced from +198 Oe to +6 Oe (figure 7.9a-c) and the magnetisation attempted to reach flux closure by 0 Oe (figure 7.9d). However, the reversal in the tip region was similar to shapes H2 and H3 with domain walls being pinned at the corners of the tip. In the outward path after reversal there are still domain walls present within the tip (figure 7.9e). However, in the return reversal (figures 7.9g-l) there is complete domain collapse within the tip after reversal (figure 7.9k). Again the cross-tie domain walls became more complex the closer they were to the edge of the shape (figures 7.9i and j).

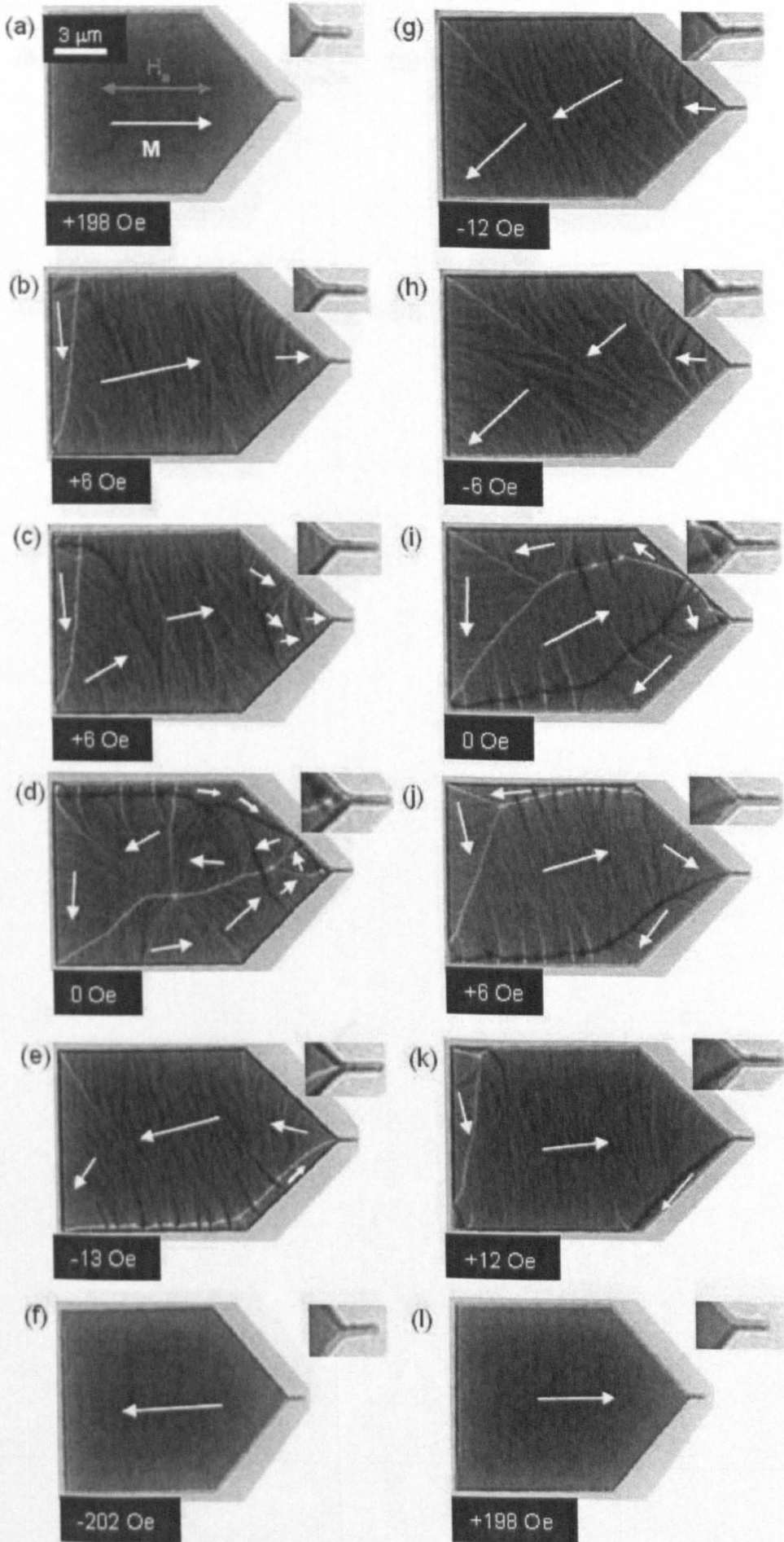


Figure 7.8: Fresnel reversal of H4. Red and white arrows indicate the direction of applied field and magnetisation direction respectively.

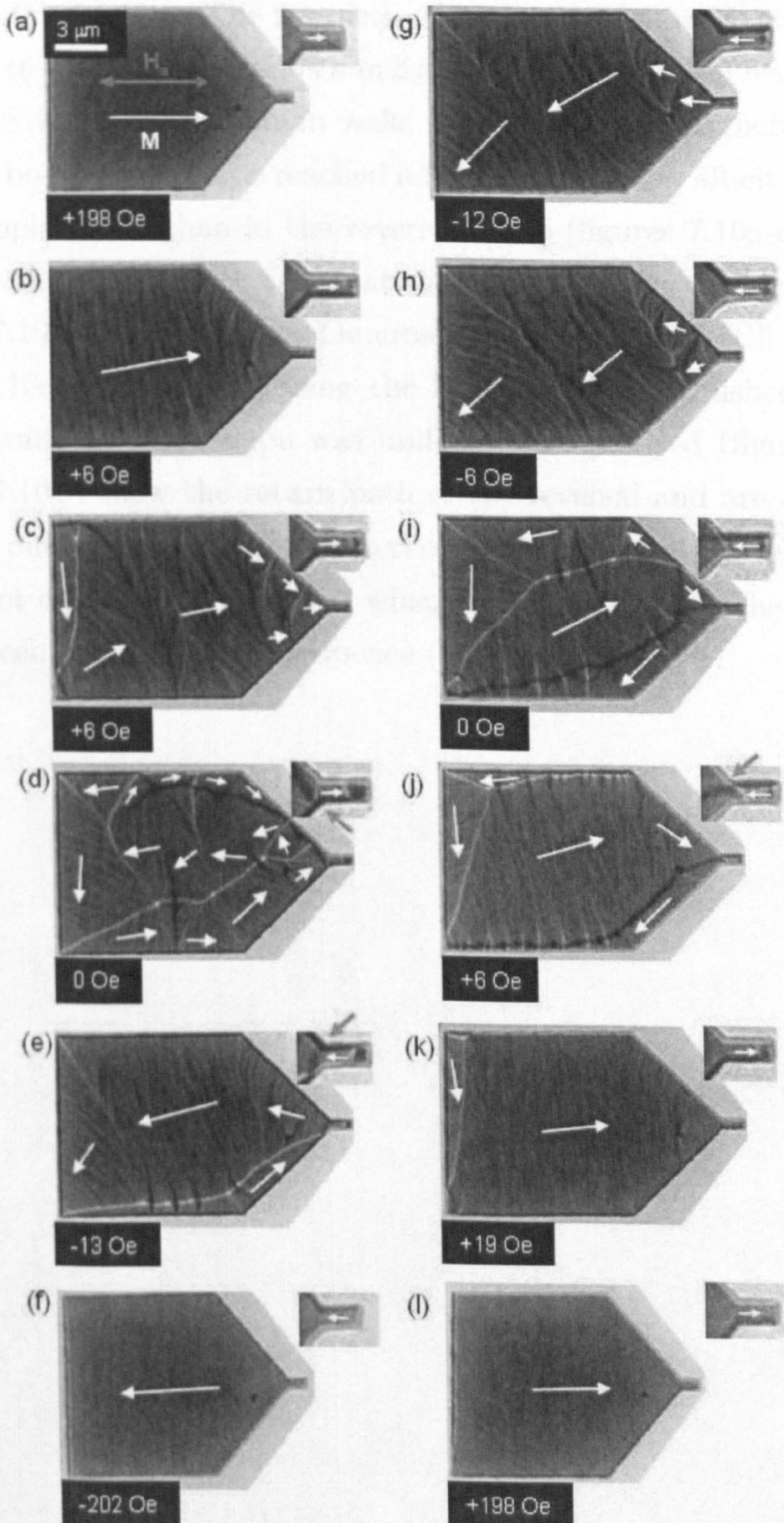


Figure 7.9: Fresnel reversal of H5. Red and white arrows indicate the direction of applied field and magnetisation direction respectively.

The final shape to be investigated was H6 which had a tapered-neck and a $1\ \mu\text{m}$ pole tip width. The magnetisation reversal followed very similar processes to those in H5 as shown in figure 7.10. As the field was reduced from $+198\ \text{Oe}$ to $0\ \text{Oe}$ domain walls formed and the magnetisation in the main body of the shape reached a flux closure state, albeit a slightly more complex state than in the reversal of H5 (figures 7.10a-d). Again domain walls which were pinned at the corners of the tip were present (figures 7.10d and e). At $-13\ \text{Oe}$ cross-tie domain walls still remained (figure 7.10e). Again increasing the field to $-202\ \text{Oe}$ pushed out the domain walls and the shape was uniformly magnetised (figure 7.10f). Figures 7.10g-l show the return path of the reversal and are consistent with the outward path. That the cross-tie domain walls have a greater number of cross-tie/vortex pairs when they are closer to the edge can also be seen in this reversal sequence (figures 7.10j and k).

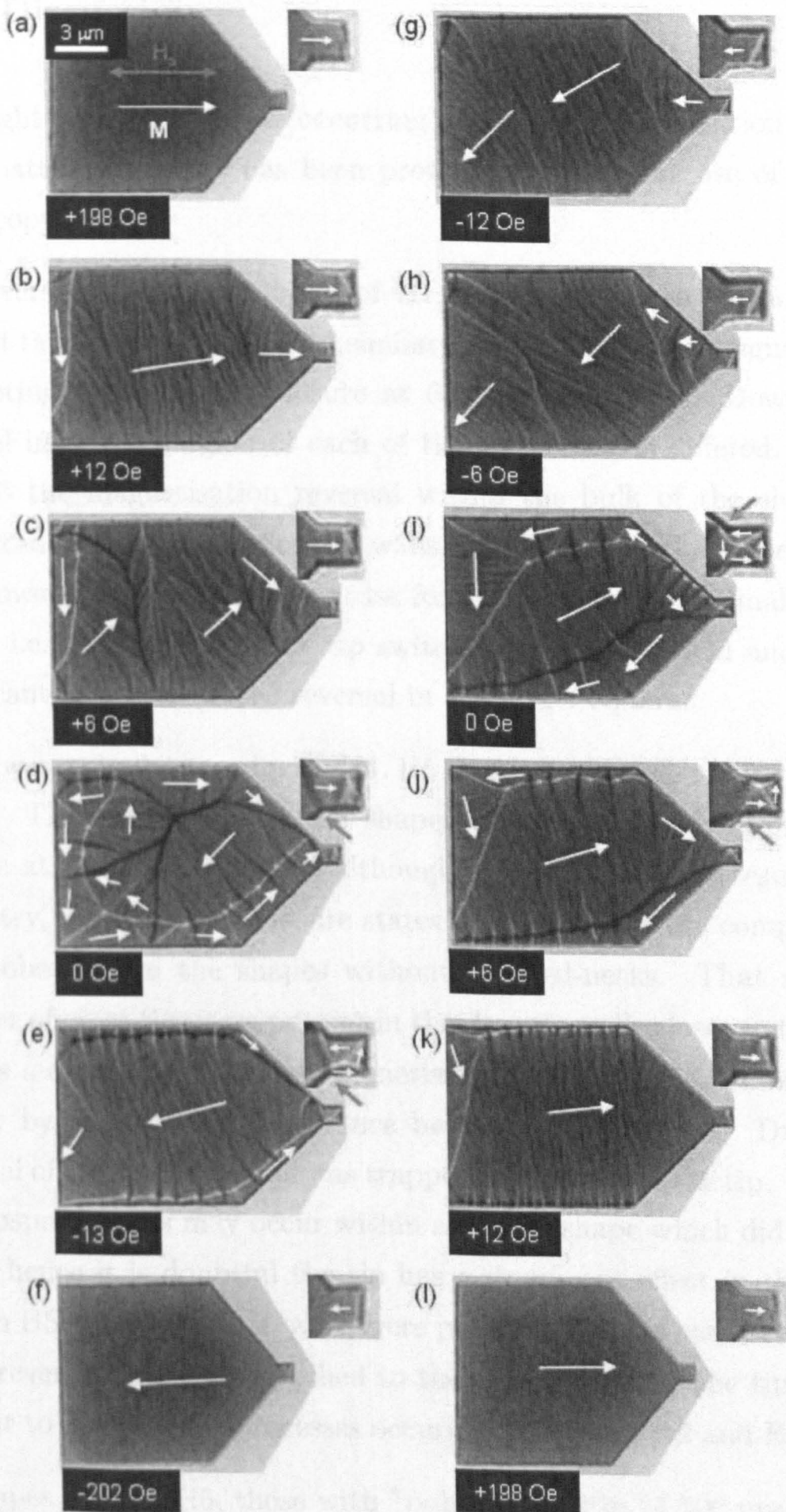


Figure 7.10: Fresnel reversal of H6. Red and white arrows indicate the direction of applied field and magnetisation direction respectively.

7.3 Discussion

An insight into the processes occurring during the magnetisation reversal of six patterned shapes has been provided through the use of Lorentz microscopy

The reversal of the main body of H1, H2 and H3, three head shapes without tapered-necks, followed similar processes with the magnetisation attempting to reach flux closure at 0 Oe applied field. However the reversal in the tip region of each of the three shapes differed. For H2 and H3 the magnetisation reversal within the bulk of the shape was influenced by the tip and domain walls were pinned at the corners of the tip. However, this was not the case for H1 which had the smallest pole width, i.e. 100 nm. Here the tip switched at a higher field and had no significant influence on the reversal in the larger square.

There was a similar trend with H4, H5 and H6, the shapes with tapered-necks. The main body of the shapes again attempted to reach flux closure at 0 Oe applied field although in this case, as a result of the geometry, the quasi-flux closure states were slightly more complex than those observed in the shapes without tapered-necks. That a greater number of cross-ties were present in the domain walls closer to the shape edge is a consequence of the magnetisation attempting to minimise the energy by shortening the distance between the cross-ties. During the reversal of H4 a domain wall was trapped at the base of the tip. However, it is suspected this may occur within a similar shape which did not have a tip, hence it is doubtful the tip has a significant effect in the case of H4. In H5 and H6 domain walls were pinned at the corner of the tip and after reversal the walls switched to the other corner of the tip which is similar to the reversal processes occurring in shapes H2 and H3.

In shapes H2 and H5, those with "pole-tip" widths of 500 nm, different domain structures were observed in the tip region during the outward and return reversals. This is consistent with previous studies which

have shown various domain structures can be supported by rectangular elements [12, 13, 14]. That different configurations are observed suggests the reversal processes occurring within these geometries are rather uncontrolled which is undesirable for a write head. However, these processes occurred in an isotropic permalloy film and not in a film with well defined anisotropy.

As mentioned in section 1.5 in chapter 1, it is important for the pole-tip to have a low coercivity and low remanence to avoid writing unwanted data. This is not the case for the pole-tips which pin the domain walls during reversal. Previous studies found through modelling that magnetisation rotation yields the fastest head field reversal [4, 15] and as seen in chapter 4 continuous films with an induced anisotropy do reverse via magnetisation rotation along the hard axis. The results in this chapter show the effect the shape anisotropy has on the reversal of a well behaved soft, isotropic film and what the induced anisotropy films have to overcome. Clearly further studies are required to determine how the magnetisation reversals of the CoFe laminated films with well defined anisotropy are influenced by the head shape. This will be discussed in section 8.3.

Bibliography

- [1] M. Mallary, A. Torabi, and M. Benakli, *IEEE Trans. Magn* **38** (4), 1719 (2002).
- [2] W. Xia, H. Aoi, H. Muraoka, and Y. Nakamura, *IEEE Trans. Magn.* **40** (4), 2365 (2004).
- [3] Y. Zhou and J.-G. Zhu, *J. Appl. Phys.* **97**, 10N518 (2005).
- [4] D. Z. Bai and J. G. Zhu, *IEEE Trans. Magn.* **38** (5), 2240 (2002).
- [5] D. Z. Bai and J. G. Zhu, *J. Appl. Phys.* **91** (10), 6833 (2002).
- [6] Y. Zhou and J.-G. Zhu, *IEEE Trans. Magn.* **41** (12), 4449 (2005).
- [7] J. van Ek, A. Shukh, E. Murdock, G. Parker, and S. Bantra, *J. Magn. Magn. Mater.* **235**, 408 (2001).
- [8] H. Zhou and R. Gustafson, *IEEE Trans. Magn.* **40**, 2395 (2004).
- [9] M. L. Plumer, S. Bozeman, J. van Ek, and R. P. Michel, *J. Appl. Phys.* **99**, 08K501 (2006).
- [10] B. M. Lairson *et al.*, *IEEE Trans. Magn.* **37**, 1223 (2001).
- [11] K. Z. Gao and H. N. Bertram, *IEEE Trans. Magn.* **38** (5), 3521 (2002).
- [12] S. McVitie, J. N. Chapman, L. Zhou, L. J. Heyderman, and W. A. P. Nicholson, *J. Magn. Magn. Mater.* **148**, 232 (1995).
- [13] X. Liu, J. Chapman, S. McVitie, and C. Wilkinson, *Appl. Phys. Lett.* **84** (22), 4406 (2004).

- [14] K. J. Kirk, J. N. Chapman, and C. D. W. Wilkinson, *Appl. Phys. Lett.* **71** (4), 539 (1997).
- [15] J. G. Zhu, C. Y. Mao, R. M. White, S. Batra, and R. Rottmayer, *IEEE Trans. Magn.* **38**, 124 (2002).

Chapter 8

Conclusions and Future Work

8.1 Introduction

In this thesis the reversal mechanisms occurring in soft magnetic thin films have been investigated extensively along with the physical microstructure. The bulk of the work focused on CoFe films which have applications in perpendicular write heads. Various single layer and laminate films were investigated which allowed the effect of including seed and spacer layers on the film properties to be studied. The majority of the micromagnetic characterisation was carried out in a TEM and many interesting features of the films were discovered such as complex defect regions and 360° domain walls in the laminate films. The physical microstructure was also characterised with a TEM which revealed features such as the mean grain size of the films and a significant roughness level in the laminate layers. The TEM investigations also revealed a large density of defects within the laminate films, the origin of these has been investigated using EELS and SEM although the exact cause was not determined.

Magnetising experiments on a patterned permalloy film were also performed. This enabled the effect of the shape anisotropy on the reversal processes of a soft, isotropic magnetic thin film to be examined. However, the CoFe films were not patterned due to time restraints. Thus the

effect of the shape on the reversal processes in a film with well defined anisotropy has still to be investigated and will be discussed further in section 8.3.

8.2 Conclusions

Chapter 3 explored the reversal processes occurring in two very soft magnetic thin films, a crystalline NiFeCuMo film and an amorphous CoFeB film. For both films relatively simple reversal behaviour was observed although the NiFeCuMo film showed a well defined anisotropy whereas it proved difficult to distinguish a preferred axis in the amorphous CoFeB film. The differences in the magnetisation ripple of the two films were also noted and the results were consistent with a preferred anisotropy axis in one film and a lack of anisotropy in the other film. The rotational behaviour and formation of domain walls during the reversal of the two films served as an introduction to the processes occurring during the magnetisation reversal of the CoFe films which are investigated through the rest of the thesis.

Studies on four initial CoFe films were discussed in chapter 4. The films differed by the inclusion or otherwise of seedlayers and spacer layers. Here the majority of the work was carried out using the Fresnel mode of Lorentz microscopy and a detailed study on the reversal behaviour of the films was presented. That the inclusion of a seedlayer significantly altered the magnetisation distribution and reduced the coercivity was attributed to a reduction in grain size. Laminating the films significantly reduced the coercivity to ~ 3 Oe and purely rotational behaviour, similar to that of the films in chapter 3, was observed during the hard axis reversal. The B-H loops of the laminate films showed superior coercivities and reversal properties. Whilst the TEM investigations revealed a smaller mean crystallite size, which is a contributing factor in the lower coercivity, areas which showed complex localised magnetic behaviour were

also observed. Normal TEM imaging revealed nothing unusual about these areas and SEM showed no signs of surface defects. Cross-sectional TEM showed significant conformal roughness throughout the laminate and it was surmised that the complex magnetic domains are stabilised at the roughest points where coupling fields much greater than 100 Oe are likely. The presence of 360° domain walls during the easy axis reversal of the quadrilayer film were also observed and again nothing unusual about the end points of the walls could be detected with conventional TEM imaging.

Further studies of laminate films were carried out with the aim of gaining a greater understanding of the localised complex behaviour and the 360° domain walls. The results from these investigations were presented in chapter 5. The majority of the films investigated here all had structural defects present which had significant effect on the reversal behaviour of the films. The in-situ magnetising experiments revealed a far greater density of 360° domain walls than in the laminated film in chapter 4. These persisted up to fields greater than 700 Oe and remained throughout reversal which was unexpected. It was also noted that the domain walls were straight when aligned along the easy axis, but took on a zigzag folding when aligned along the hard axis. This was discussed and the reversal mechanism for the walls was proposed. Although there were instances where the end points of the domain walls were located at the structural defects there were also occasions where this was not the case and, as in chapter 4, normal TEM imaging revealed nothing unusual about the end points of the walls. However, it is likely that all 360° domain walls are associated with some inhomogeneity at the end points which disturbs the magnetisation configuration enough to pin the wall. It may be possible to model the micromagnetics and this is discussed in section 8.3. Quantitative studies with DPC were carried out on the laminate films and it was discovered that some of the 360° domain walls were present through the whole thickness of the laminate, although some were confined to one or two layers. It is likely they are confined to the

uppermost layers where the roughness level is greatest.

The physical characterisation of the defects was presented in both chapter 5 and chapter 6. Conventional TEM followed by SEM of the structural defects revealed there were particles present on the substrate before the CoFe films were deposited. This caused a raised area in the film which had a deficiency of material around it. The area around the defects was found to be oxygen rich and indeed the whole defect may be oxygen rich, however, as normalisation with the zero loss peak was not carried out this may be surface oxidation. In an attempt to discover the identity of the particle and gain a greater understanding of the film growth cross-sectional specimens were prepared. The conformal roughness observed in chapter 4 was again apparent here. Bright and dark field imaging revealed the spacer layers were effective at breaking up the growth across the majority of the film. Spectrum imaging with EELS revealed a possible tailing of the Ni into the CoFe layer, although this may be due to the roughness of the spacer layers. However, no defects were found in the cross-sectional specimens and the origin of the particles on the substrate remain unknown at this stage. The structural defects are ideal sites to capture a Bloch line moving in a 180° Néel wall and provide the stabilisation necessary for the 360° domain walls to form.

The magnetisation processes occurring during the reversal of the CoFe continuous films are interesting and aid the understanding of the micromagnetic structure. However, from an industrial point of view it is important to investigate the processes occurring in patterned shapes of similar dimensions to perpendicular write heads as this will aid understanding when shape anisotropy and stresses become involved. Chapter 7 focused on initial studies from patterned permalloy shapes and thus enabled a soft, isotropic film to be investigated. The results showed the processes occurring in two sets of shapes, those with tapered-necks and those without. It was discovered for the “pole tip” widths of 100 nm the reversal processes occurring within the tip were not significantly in-

fluenced by the reversal in the main body of the shape. However, wider “pole tip” widths of 500 nm and 1 μm did influence the reversal and the 500 nm tips were capable of supporting different domain structures within the tip. These observations are highly undesirable for a write head and show the obstacles which the CoFe films with well defined anisotropy face.

To summarise, the main findings in this thesis have emphasised how important it is to have smooth interfaces in multilayered magnetic films. That magnetic defects occur when there is a high degree of roughness would have major implications if present in films used for device applications. The effect of physical defects on the magnetisation processes which occur during reversal showed the importance of having clean substrates when considering film deposition. Some interesting properties of 360° domain walls were also revealed and there may be implications for some future device applications which require domain wall pinning. Finally the patterning of permalloy films to write head shapes revealed how the shape anisotropy effects the reversal behaviour and the challenges which CoFe films have to overcome.

8.3 Future Work

Possible future work to aid the understanding of the defects observed in chapters 5 and 6 is detailed in this section along with further studies on the CoFe films.

From the results in chapter 6 it is clear the dual beam FIB/SEM could be used to prepare TEM cross-sectional specimens of specific areas. Therefore the structural defects observed in the laminate films in chapters 5 and 6 could be cross-sectioned. This would allow EELS to be performed and the identity of the particles which are present on the substrate could be found. It May also be possible with the dual beam FIB/SEM to prepare cross-sectional specimens from the complex magnetic defect regions

which were observed in chapter 4. This would require initial identification of the defect areas using the compu-stage on the FEI Tecnai F20. It would then be possible to deliberately contaminate the sample to provide markers at a measurable distance from the area of interest. This would enable identification of the magnetic defect area when the sample is transferred to the FIB/SEM. Analytical investigations of the cross-sectional samples would allow the growth of the films at these points to be investigated and may provide information as to the origin of defect areas.

The reversal behaviour of the 360° domain walls which were observed in the laminate films in chapters 4 and 5 is reasonably well understood, however, the end points which pin the walls are not. It would be worthwhile carrying out micromagnetic modelling of these to aid understanding. This is by no means an easy calculation and the initial input parameters would need to be considered carefully. For example whether a structure similar to the defects observed in chapter 5 should be included and perhaps initial studies should consider single layer films before moving onto the more complex laminate films.

To further the studies of how the shape anisotropy of the write head effects the reversal, the CoFe films from chapter 4 should be patterned into shapes similar to those investigated in chapter 7. Fresnel studies of the patterned shapes will reveal how films with well defined anisotropies behave in an environment where there is a complex stress distribution. In Chapter 4 the displacement of walls between layers within the bilayered films was observed and it would be of interest to see if such walls occur within the films when patterned down and if so how the walls behave when there are other stresses present. The investigation of the patterned CoFe films would also reveal whether the purely rotational behaviour observed for the continuous quadrilayer film in chapter 4 still occurred when the sample was patterned down and if any complex localised behaviour was present.

From a technological point of view it is important to establish whether the domain structures within the tip are reproducible at 0 Oe applied field or if the behaviour in the CoFe films is similar to that observed for the permalloy film in chapter 7 where variable, uncontrollable processes occurred. This would relate to the remanent state of the head and the erase-after-write phenomena which was mentioned in chapter 1 section 1.5.1. Another possible investigation would be to vary the angle of the “tapered-neck” and the height of the “pole tip” to determine how they effect the reversal. This may aid in optimising the geometry of the writer as the areal storage density is increased further. Another issue which deserves attention is the concern that there are areas within the pole tip in which the flux is channelled down. To this end it would be worthwhile investigating the flux emitted out of the tip of the patterned CoFe shapes using DPC. However, this is quite a complex experiment as the stray field from the tip would have a significant effect and separating out the various field contributions would prove timely.

Other possible studies involve varying the materials used in the laminate films, for example the use of Ru as a spacer layer or Cu as a seed layer. Interest lies in how the different layers effect the grain growth, i.e. are there alternative materials which give a smaller grain size or smoother interfaces. Also how are the magnetisation processes occurring during reversal effected and are there better alternatives for perpendicular writers than the CoFe laminate films investigated in this thesis.

